Rhodes University

Observations of Diffuse Radio Emission in the Perseus Galaxy Cluster

Author:
Clemence Mungwariri

Supervisors:
Prof. Gianni Bernardi
Prof. Oleg Smirnov

A thesis submitted in fulfilment of the requirements for the degree of Master of Science

in the
Faculty of Science
Department of Physics and Electronics
Centre for Radio Astronomy Techniques and Technologies

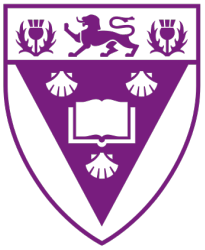

RHODES UNIVERSITY
Where leaders learn

Abstract

In this thesis we analysed Westerbork observations of the Perseus galaxy cluster at 1380 MHz. Observations consist of two different pointings, covering a total of ~ 0.5 square degrees, one including the known mini halo and the source 3C 84, the other centred on the source 3C 83.1 B. We obtained images with 83 μJy beam^{-1} and 240 μJy beam^{-1} noise rms for the two pointings respectively. We achieved a 60000 : 1 dynamic range in the image containing the bright 3C 84 source.

We imaged the mini halo surrounding 3C 84 at high sensitivity, measuring its diameter to be ~ 140 kpc and its power 4×10^{24} W Hz^{-1}. Its morphology agrees quite well with that observed at 240 MHz (e.g. Gendron-Marsolais et al., 2017). We measured the flux density of 3C 84 to be 20.5 ± 0.4 Jy at the 2007 epoch, consistent with a factor of ~ 2 increase since the 1960s.

Acknowledgements

I would like to sincerely thank my supervisor Prof. Gianni Bernardi for his invaluable guidance, motivation, expertise and patience throughout this project, as well as the endless life-long lessons he has imparted on me during our time working together. This work would not be possible without him. I am eternally grateful for the opportunity to work under the RATT group, and for this I extend my gratitude to Prof. Bernardi and to my co-supervisor Prof. Oleg Smirnov.

I am also grateful to the RATT group, particularly Ridhima Nunhokee, Ben Hugo, Jon Zwart, Jonathan Kenyon and others for the engagement and assistance. I also would like to thank Gift Sichone as well as my friends Siyanda Matika, Olorato Mosiane, Sibonelo Ngobese and others for the discussions, encouragement and support.

Lastly, I would like to thank my mother for the many years of stern but patient encouragement, insightful advice and unwavering support. I would also like to thank my brother Leeroy and the rest of my family for the support.

To my mother and my brother

Declaration of Authorship

I, Clemence Mungwariri, declare that this thesis titled, '*Observations of Diffuse Radio Emission in the Perseus Galaxy Cluster*' and the work presented in it are my own. I confirm that:

- This work was done wholly or mainly while in candidature for a research degree at this University.
- Where any part of this thesis has previously been submitted for a degree or any other qualification at this University or any other institution, this has been clearly stated.
- Where I have consulted the published work of others, this is always clearly attributed.
- Where I have quoted from the work of others, the source is always given. With the exception of such quotations, this thesis is entirely my own work.
- I have acknowledged all main sources of help.
- Where the thesis is based on work done by myself jointly with others, I have made clear exactly what was done by others and what I have contributed myself.

Signed: 

Date: 29 OCTOBER 2019

Contents

List of Figures

List of Tables

Abbreviations

ΛCDM	**Lambda C**old **D**ark **M**atter
3C	Third **C**ambridge Catalogue
A 426	**A**bell **426**
AGN	**A**ctive **G**alactic **Nucleus**
AUI	**A**ssociated **U**niversities, **I**nc.
BT	**B**ent-**T**ailed
CASA	**C**ommon **A**stronomy **S**oftware **A**pplications
CC	**C**ool **C**ore
CF	**C**ooling **F**low
CMB	**C**osmic **M**icrowave **B**ackground
DR	**D**ynamic **R**ange
FR I, FR II	**F**anaroff-**R**iley type **I**, **F**anaroff-**R**iley type **II**
HT	**H**ead-**T**ail
IC	**I**ntra**C**luster *or* **I**ndex **C**atalogue
ICM	**I**ntra**C**luster **M**edium
MH	**M**ini **H**alo
NED	**N**ASA/IPAC **E**xragalactic **D**atabase
NGC	**N**ew **G**eneral **C**atalogue
PA	**P**osition **A**angle
PSF	**P**oint **S**pread **F**unction
PyBDSF	**Py**thon **B**lob **D**etector and **S**ource **F**inder
RFI	**R**adio **F**requency **I**nterference
RH	**R**adio **H**alo
ROSAT	**RO**entgen **SAT**ellite
RR	**R**adio **R**elic
RT	**R**adio **T**elescope
UTC	Coordinated Universal Time
VLA	**V**ery **L**arge **A**rray
WSRT	**W**esterbork **S**ynthesis **R**adio **T**elescope

Symbols

M	mass	kg
t, t_H	time, Hubble time	s
R, r	radius	m
v	velocity	$\mathrm{m} \cdot \mathrm{s}^{-1}$
m	apparent magnitude	
z	redshift	
L_X	X-ray luminosity	$\mathrm{erg} \cdot \mathrm{s}^{-1}$
n	number density	$\mathrm{particles} \cdot \mathrm{cm}^{-3}$
T	temperature	K
I_X	X-ray surface brightness	$\mathrm{W} \cdot \mathrm{cm}^{-2}$
I_ν	surface brightness at frequency ν	$\mathrm{mJy} \cdot \mathrm{arcsec}^{-2}$
$P_{1.4}$	monochromatic radio power at 1.4GHz	$\mathrm{W} \cdot \mathrm{Hz}^{-1}$
P_ν	spectral power at frequency ν	$\mathrm{W} \cdot \mathrm{Hz}^{-1}$
S_ν	spectral flux density at frequency ν	Jy
P_{ram}	ram pressure	$\mathrm{dyne} \cdot \mathrm{cm}^{-2}$
R_{MH}	mini-halo radius	kpc
D	antenna diameter	m
$B, \mathbf{b}$	baseline length, baseline vector	m
$\hat{s}$	unit vector	
V_p, Vq	voltage induced in antennas p and q	
V_{pq}	complex visibility measured by the baseline of antennas p and q	
$I(l, m)$	sky brightness distribution function	
$\mathbf{J}$	complex Jones matrix	
H	Hermitian operator	
I, Q, U, V	Stokes parameters	
$\mathbf{B}$	intrinsic source brightness matrix	
$\mathbf{B}(\nu)$	complex bandpass matrix	
$\mathbf{G}(t)$	complex gain matrix	
V^m	model visibilities	

$I^D(l,m)$	dirty image	
σ	velocity dispersion	$\mathrm{km} \cdot \mathrm{s}^{-1}$
ϵ_ν	emissivity	$\mathrm{erg} \cdot \mathrm{s}^{-1}$
ρ	density	$\mathrm{kg} \cdot \mathrm{m}^{-3}$
ρ_{ICM}	intracluster gas density	$\mathrm{particles} \cdot \mathrm{cm}^{-3}$
α	spectral index	
ν	frequency	Hz
θ_{res}	angular resolution	rad
λ_{obs}	observing wavelength	m
τ_g	geometric time delay	s
ω	angular frequency	$\mathrm{rad} \cdot \mathrm{s}^{-1}$
ϕ	phase	rad
γ	loop gain	
σ_I	noise standard deviation	$\mathrm{Jy} \cdot \mathrm{beam}^{-1}$

Physical Constants

Speed of light	c	=	$2.99792458 \times 10^{8}\ \mathrm{m \cdot s^{-1}}$
Planck constant	h	=	$6.62607015 \times 10^{-34}\ \mathrm{J \cdot s}$
Newtonian gravitational constant	G	=	$6.67430 \times 10^{-11}\ \mathrm{N \cdot m^{2} \cdot kg^{-2}}$
Boltzmann constant	k_B	=	$1.3806488 \times 10^{-23}\ \mathrm{J \cdot K^{-1}}$
Electron mass	m_e	=	$9.1093837015 \times 10^{-31}\ \mathrm{kg}$
Proton mass	m_p	=	$1.67262192369 \times 10^{-27}\ \mathrm{kg}$
Solar mass	$M_\odot$	=	$1.98847 \times 10^{30}\ \mathrm{kg}$
Hubble constant	H_0	=	$69.6\ \mathrm{km \cdot s^{-1} \cdot Mpc^{-1}}$

Chapter 1

Background

1.1 Galaxy Clusters

The standard ΛCDM model suggests that the Universe's large scale structure results from the gravity-driven hierarchical merging of smaller substructures (Gott III and Rees, 1975; White and Rees, 1978; Blumenthal et al., 1984). This ongoing hierarchical growth process has resulted in a continuous distribution of cosmic systems spanning a wide range of scales, from the size of galaxies through groups and clusters up to superclusters and filaments. Galaxy clusters generally grow through major and minor mergers in the dense filamentary regions. With masses ranging from 10^{14} $M_\odot$ up to a few times 10^{15} $M_\odot$, galaxy clusters are the most massive gravitationally bound objects in the Universe to result from this bottom-up structure formation scheme.

Galaxy clusters are virialized cosmic structures consisting of a number of galaxies held together by a mutual gravitational attraction. A lower limit to the cluster's relaxation time is given by the crossing time t_{cr}, the time it takes to travel across the galaxy cluster, $t_{cr}(r) \propto r/v_r$, where r is the cluster radius and v_r is the radial velocity (e.g., Sarazin, 1988). Velocity dispersions for galaxies in rich clusters are in the range of $400 - 1400$ km s^{-1} (e.g., Struble and Rood, 1991), with a median radial velocity dispersion of 750 km s^{-1} (e.g., Bahcall, 1996). Combining this with the typical cluster radius, which is of the order of 1 Mpc, estimates for typical crossing times are in the range of 1 Gyr, which is significantly less than the Hubble time, showing that clusters have had, in principle, sufficient time to be dynamically relaxed.

1.2 Optical properties

Rich clusters are distinguished from poor clusters and more so, from galaxy groups, by the number of their constituent galaxies (Paul et al., 2017). Using data from the Palomar Sky Survey, Abell (1958) defined a rich cluster as one containing a minimum of 50 galaxies whose magnitude, m is within the range $m_3 \leq m \leq m_3 + 2$, inside a circle of radius $R_A = 1.7/z$ arcmin $= 3h_{50}^{-1}$ Mpc around the cluster centre. R_A is referred to as the Abell radius, and m_3 is the

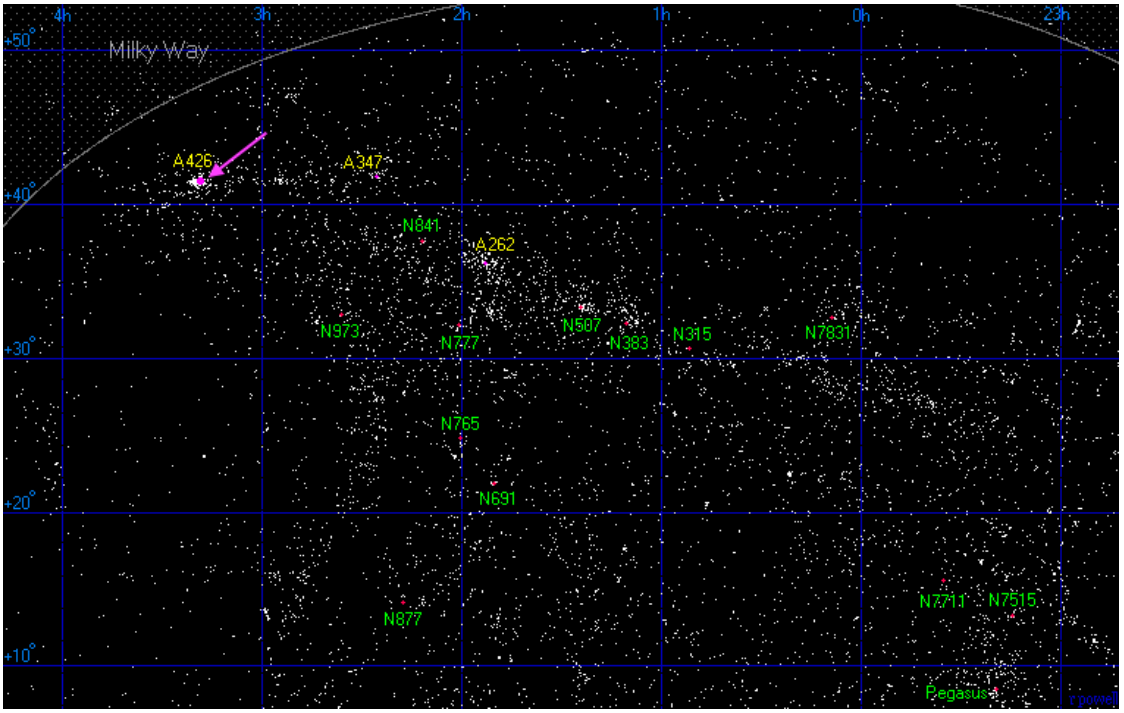

FIGURE 1.1: Location of the Perseus Cluster (A 426), marked by the large pink dot, in the Pisces-Pisces supercluster[1] (Powell, 2006)

magnitude of the third brightest cluster member. The clusters under consideration in the Abell catalogue had redshifts between 0.02 and 0.20 (Bahcall, 1977).

Due to the inherent difficulty in defining the edges of a cluster, there are multiple definitions for cluster radii, although the gravitational radius, $R_{\rm G} \approx \frac{2GM}{3v_r^2}$ is a common one. Alternatively, it can be defined as the radius at which the galaxy surface brightness density decreases to about 1% of the core density. Under this definition, rich clusters typically contain 30 to 300 galaxies (Bahcall, 1996) and tend to have symmetrical morphologies, with a centrally concentrated galaxy distribution and little sub-clustering, compared to poor clusters and galaxy groups.

Since galaxy clusters were first discovered in the optical domain, they are historically classified based on the size and spatial distribution of their constituent galaxy population, but only 5% of galaxies live in rich clusters (Dressler, 1984). The majority of the cluster mass is in the form of dark matter, which constitutes 85% while baryonic matter accounts for about 15% of the total mass.

One of the most studied galaxy clusters is the Perseus galaxy cluster ($z \approx 0.0183$, Fabian et al., 2000), located in the Perseus-Pisces supercluster, a 300 million light year long cosmic structure about 250 million light years away (Figure 1.1). In the optical wavelengths, it has an unusually high velocity dispersion of $\sigma = 1420 \pm 140$ km s^{-1} (Tanaka, 1985). Brunzendorf and Meusinger (1999) find roughly 30% morphologically irregular and spiral galaxies within the central $30'$[2] and roughly 50% for the entire galaxy cluster in general.

[1] credit: Richard Powell
[2] where $1' = 31.5\ h_{50}^{-1}$ kpc

1.2.1 NGC 1275

Located near the Perseus galaxy cluster centre is NGC 1275, one of the most active known galaxies (Gisler and Miley, 1979). NGC 1275 was discovered on 17 October 1786 by William Herschel[3] and catalogued as H 603. It is also known as Perseus A, as it is the brightest member of the Perseus galaxy cluster.

NGC 1275 is a giant elliptical galaxy initially classified as a Seyfert galaxy (Seyfert, 1943) based on its (broad) line and compact continuum emission properties. It is also surrounded by a low-ionisation emission-line nebula (Figure 1.2; Pedlar et al., 1990; Fabian et al., 2008), which has an 80 kpc radius and $\sim 10^{10}$ $M_{\odot}$ in cold gas. This nebulous component is the dominant gas component in the inner 15 kpc of the optical emission in the inner region of the Perseus cluster, and whose velocities (Hatch et al., 2006; Salomé et al., 2011) correspond to the bulk shear measurements from the Hitomi X-ray observations of the same region, suggesting that it moves along with the ICM hot plasma (The Hitomi Collaboration, 2016).

Hubble Space Telescope images show roughly $100 - 200$ Myr old emission line filaments surrounding NGC 1275 (Figure 1.2 Fabian et al., 2008) which also harbors star forming regions hosting some young star clusters that could result from galaxy mergers.

[3]recorded as NGC 1278, but the position is closer to the much brighter NGC 1275

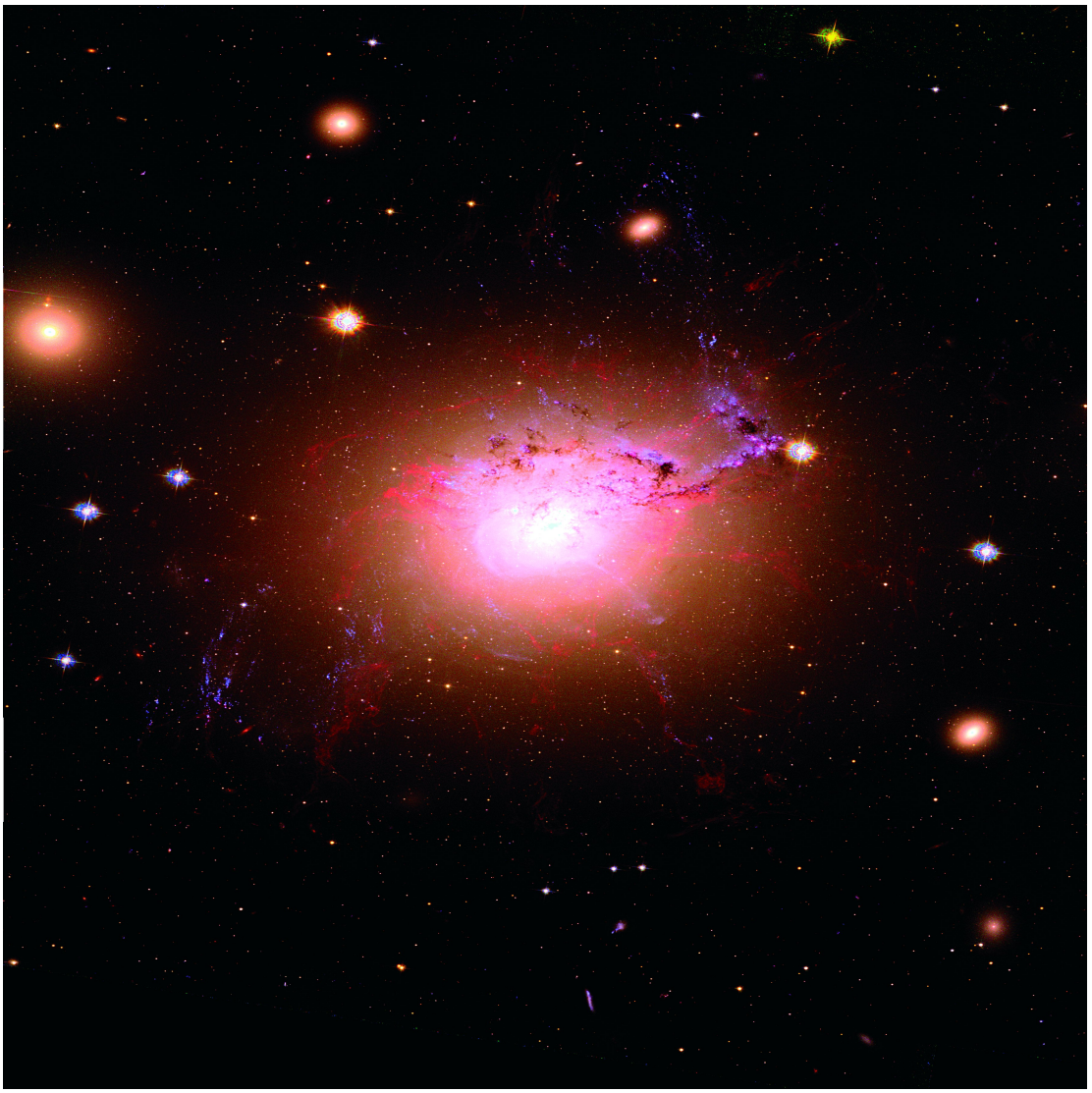

FIGURE 1.2: Optical image of NGC 1275 (red). Young star clusters (blue) roughly trace out the nebulous network of filamentary structure around it (Fabian et al., 2008).

1.3 X-ray emission

From the mid 1960*s* to the early 1970*s* extragalactic X-ray emission discoveries were made in the direction of M87 in the Virgo cluster (Byram et al., 1966), Perseus (Fritz et al., 1971; Gursky et al., 1971) and Coma, three of the closest galaxy clusters. The X-ray sky catalogue compiled from the Uhuru X-ray astronomy satellite's observations shortly confirmed that X-ray emission from galaxy clusters was commonplace, with luminosities of the order $10^{42.5} \leq L_{\mathrm{X[2-10\ keV]}} \leq 10^{45}$ erg s^{-1} (Sarazin, 1988).

The baryonic component of the mass in galaxy clusters is dominated by the hot, diffuse intracluster medium, which makes up $\sim 12\%$ of the cluster's total mass, while luminous matter, in the form of galaxies, comprises only $\sim 3\%$ of the total cluster mass (Voit, 2005; Aleksić et al., 2010). The spatial extent of the X-ray emitting intracluster gas is comparable to the scale of the entire cluster, with gas densities around 3×10^{-3} particles cm^{-3} (Jones and Forman, 1992) and

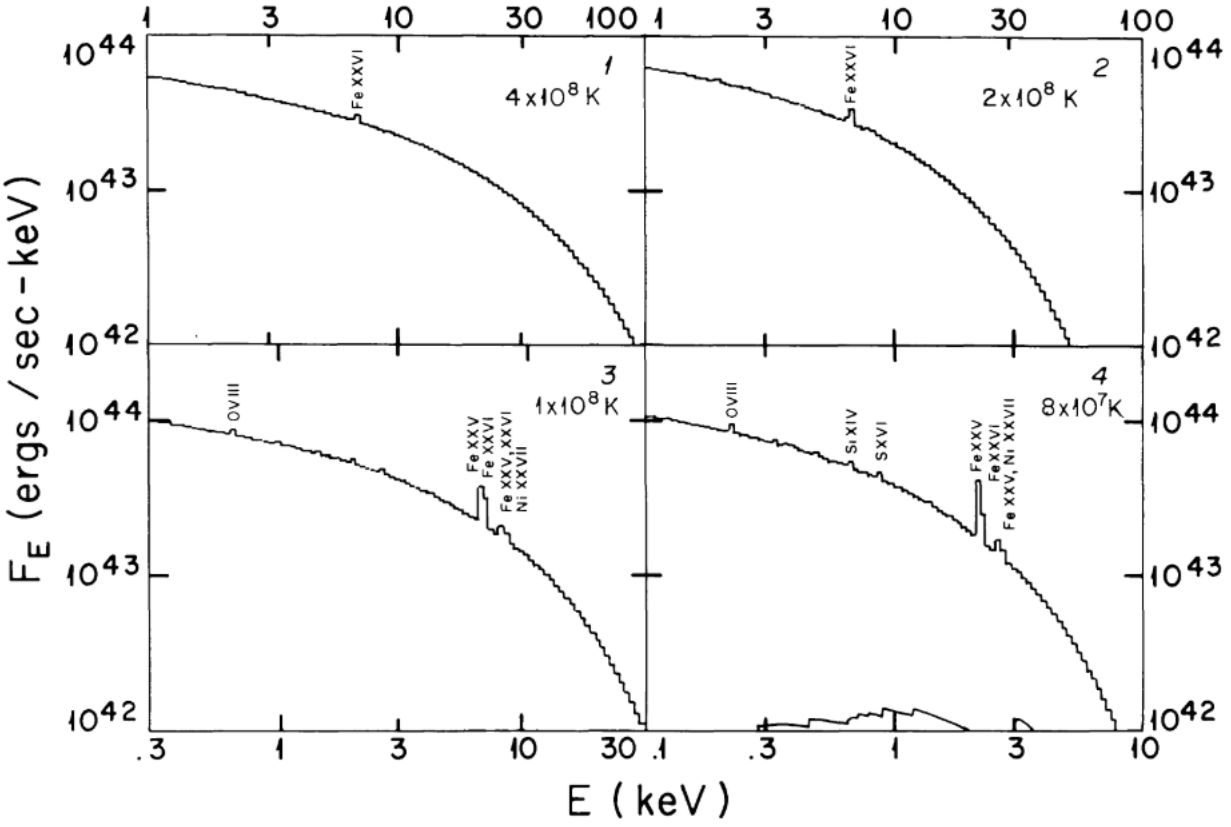

FIGURE 1.3: Integrated X-ray emission spectra predicted from isothermal models for the ICM gas in galaxy clusters at high temperatures: 0.8×10^8 K $\leq T_{\rm g} \leq 4 \times 10^8$ K. The gas is assumed to be in an isothermal sphere of radius 500 kpc, with a proton number density of 1×10^{-3} particles cm^{-3}. The lower curves represent bound-free emission, and the strongest line emission features are labeled on the upper curves (Sarazin and Bahcall, 1977).

temperatures in the range of $2 \times 10^{7-8}$ K (Felten et al., 1966). Thus besides optical emission, all galaxy clusters have an extensive, diffuse, ionized gas component which emits X-rays via thermal bremsstrahlung. Bremsstrahlung radiation results from the interactions between free electrons and positively charged nuclei in an ionized plasma. Electrons which have a Maxwellian velocity distribution in a plasma are decelerated by their interactions with the positively charged nuclei and thus emit continuum radiation. The bremsstrahlung emissivity, i.e. the luminosity per frequency and unit volume, due to a nucleus of charge Z is given by (Lea et al., 2002; Sarazin, 1988):

$$\epsilon_\nu = \frac{2^5 \pi e^6}{3 m_{\rm e} c^3} \left(\frac{2\pi}{3 m_{\rm e} k_B T_{\rm g}} \right)^{1/2} Z^2 n_{\rm e} n_Z g_{\rm ff}(Z, T_{\rm g}, \nu) e^{-h\nu/k_{\rm B} T_{\rm g}}, \tag{1.1}$$

where $g_{\rm ff}(Z, T_{\rm g}, \nu)$ is the Gaunt factor, a quantum mechanical correction factor of order unity (Gaunt, 1930; Karzas and Latter, 1961), $n_{\rm e}$ and n_Z represent the number density of the electrons and nucleus, respectively, Z is the atomic nucleus charge, h is Planck's constant, $k_{\rm B}$ is the Boltzmann's constant and $\rm T_g$ is the gas temperature.

The brehmsstrahlung spectrum shows an exponential cutoff at energies $h\nu > K_{\rm B} T_{\rm g}$ (Figure 1.3). This condition allows us to determine the gas temperature from the spectrum or, conversely, to measure the spectrum break, given the gas temperature.

The gas density profile is often assumed to be described by a so called isothermal model (Cavaliere and Fusco-Femiano, 1976; Bahcall, 1996; Neumann and Arnaud, 1999; Makino et al., 2002):

$$\rho_{\rm g}(r) = \frac{\rho_{\rm g,0}}{\left[1 + \left(\frac{r}{r_{\rm c}}\right)^2\right]^{3\beta/2}}, \tag{1.2}$$

where $r_{\rm c}$ is the cluster core radius, $\rho_{\rm g,0} = \rho_{\rm g}(r_{\rm c})$ is the gas density at the cluster core and parameter $\beta = \frac{\sigma^2 \mu m_{\rm p}}{K_{\rm B} T_{\rm g}}$ is the energy per unit mass ratio between the galaxies and the gas, as derived from cluster observations. Cluster observations and density profile fits of the gas and galaxy distribution in clusters find a value of $\beta \approx 1$ (Lubin and Bahcall, 1993; Bahcall and Lubin, 1994).

The X-ray surface brightness distribution in galaxy clusters is described by (Jones and Forman, 1984; Neumann and Arnaud, 1999):

$$I_{\rm X}(r) = \frac{I_0}{\left[1 + \left(\frac{r}{r_{\rm c}}\right)^2\right]^{3\beta - \frac{1}{2}}}. \tag{1.3}$$

The cooling time-scale for a galaxy cluster's gas is defined as (Sarazin, 1988):

$$t_{\rm cool} = 8.5 \times 10^{10} \left(\frac{n_Z}{10^{-3}{\rm cm}^{-3}}\right)^{-1} \left(\frac{T_{\rm g}}{10^8{\rm K}}\right)^{1/2} yr. \tag{1.4}$$

This cooling time-scale ($\rm t_{cool}$) in most galaxy clusters is longer than the Hubble time (Sarazin, 1988; Fabian et al., 2002) and by extension, the cluster age, $\rm t_a$. Since the emissivity is proportional to the square of the gas density, a galaxy cluster's densest regions cool faster. Consequently, galaxy clusters whose density profile is highly peaked have much shorter cooling times in their central regions, which makes cooling important for such clusters.

If cooling occurs faster than heating and there isn't a massive net loss of mass in the ICM, $\rm t_{\mathit{cool}}$ (equation 1.4) eventually becomes less than $\rm t_{\mathit{a}}$ in these galaxy clusters with highly peaked density profiles. Since the gas density profile generally decreases radially from the center, $\rm t_{cool}$ increases radially. The cooling in massive clusters takes longer, and so a quasi-hydrostatic sphere forms, whose extent is bounded by the cooling radius ($\rm r_{cool}$) where $\rm t_{cool} = t_a$. Beyond this radius, the cooling time-scale remains in the range of the Hubble time t_H and cooling is not important. Within the cooling radius, in the absence of a heat source, a lot of the intracluster gas cools out of the hot intracluster medium. To support the weight of the outer gas, it has been suggested (Sarazin, 1988; Fabian, 1994) that the drop in temperature at the cluster core results in the surrounding gas flowing towards the cluster center, in order to preserve pressure balance, resulting in a slow, subsonic inflow of a few hundred $\rm M_\odot\ yr^{-1}$ (Fabian et al., 2006), referred to as the cooling flow (CF). Galaxy clusters with small cooling time-scales were hence called cooling flow clusters (Fabian, 1994; Fabian et al., 2002).

X-ray observations confirm that some clusters have cooling time-scales in the range of $\rm t_H$ (Lea et al., 2002; Silk, 1976; Cowie and Binney, 1977; Fabian and Nulsen, 1977; Sarazin, 1988).

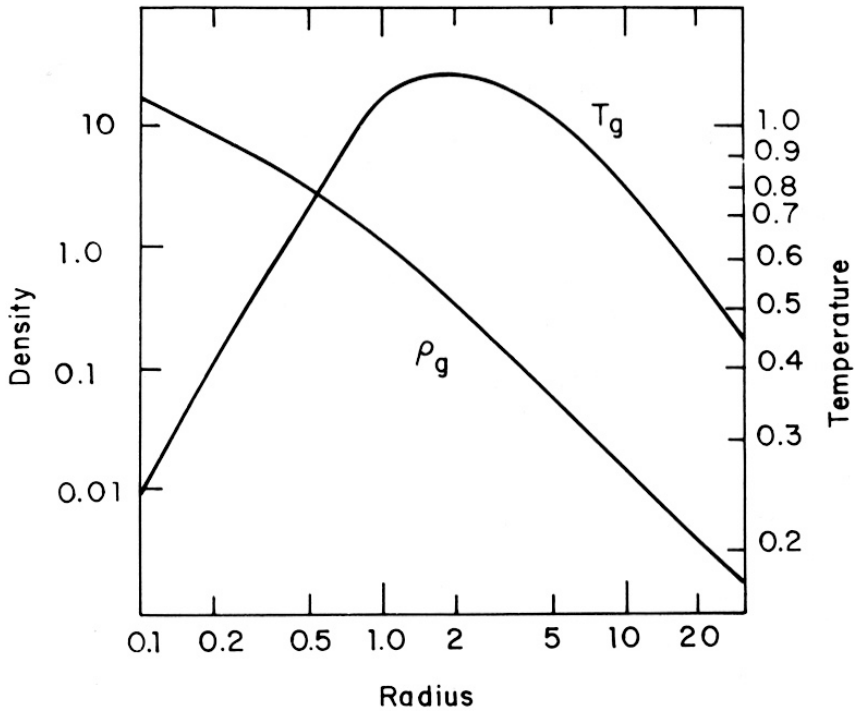

FIGURE 1.4: Modelled gas density and gas temperature in a galaxy cluster (Cowie and Binney, 1977). The radius is normalised by the core radius ($x = r/r_c$), $\rho_g = \rho_g(r)/\rho_g(r_c)$ and the gas temperature by $k_B/(\mu m_p \sigma^2)$. credit: (Sarazin, 1988)

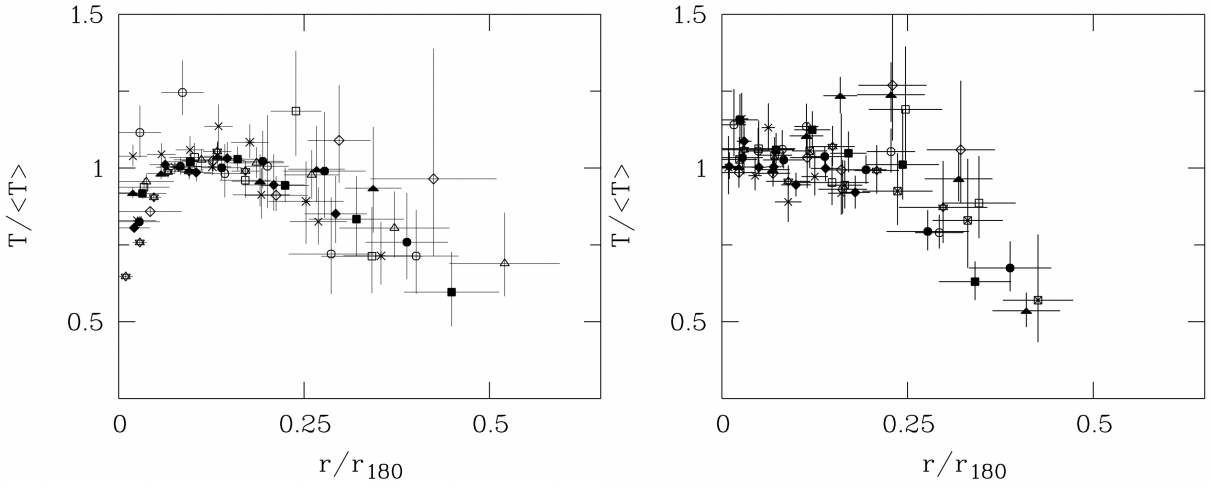

FIGURE 1.5: Left: Projected temperature profiles for cool-core clusters. The Perseus cluster's temperature profile is represented by stars in the plot. Right: Projected temperature profiles for non-cool-core clusters. Credit: (De Grandi and Molendi, 2001).

Measurements of temperature profiles that increase radially have also been made (Gorenstein et al., 1977; Ulmer and Jernigan, 1978), in line with predictions from models such as shown in Figure 1.4 with observational support as shown in the left panel of Figure 1.5 in some clusters, while other clusters still show the expected temperature profile as shown in the right panel of Figure 1.5.

Some of the fundamental assumptions of the simple cooling flow model have been discounted in

recent X-ray findings (Böhringer and Werner, 2010; Feretti et al., 2012). While the existence of cool gas around the cores of CF galaxy clusters is virtually indisputable, there has not been conclusive observational evidence of a cooling flow thus far. Additionally, the amount of new stars in cluster interiors generally do not match the mass deposition rates in the range of hundreds to thousands (Thomas and Fabian, 1987; Peterson and Fabian, 2006) of solar masses found by X-ray measurements (Fabian, 2002). Furthermore, X-ray observations have been unable to show evidence of gas cooling below 1-2 keV (Fabian, 2002).

Since the evidence against cooling flows in the classical sense does not preclude the existence of cool cores in galaxy clusters characterised by short cooling times, classical CF clusters are now referred to as cool-core (CC) clusters. The existence of some heating mechanism may help to explain the lack of strong cooling in the central regions of CC clusters (Fabian, 2002; Böhringer and Werner, 2010). Possible sources of heat include supernova heating (Silk et al., 1986), turbulence from minor merger events and energy expulsion from active galaxies (Fabian, 2002).

1.3.1 X-ray emission in the Perseus cluster

The Perseus cluster is a cool-core cluster with a luminosity of $L_{\mathrm{X}\ [0.1-2.4\ \mathrm{keV}]} = 8.65{\times}10^{44}\ \mathrm{erg\,s^{-1}}$, which peaks at the location of NGC 1275 (Ikebe et al., 2002) and it is one of the brightest X-ray sources in the sky.

Figure 1.6 shows the X-ray surface brightness distribution at the centre of the cluster, along with structures at various angular scales. At larger scales, several low surface brightness areas are visible, aligned along a south-east to north-west line passing through the core.

Two cavities (i.e., X-ray faint regions) can be seen close to the X-ray core. They are about 30 arcseconds across (Fabian et al., 2000, 2002). Two further cavities are seen, at larger distancs from the core, about 25 kpc to the north-west and 45 kpc to the south-south-east of the core respectively (Böhringer et al., 1993). The X-ray cavities are encircled by bright rims with X-ray emission greater than the surrounding gas.

Figure 1.7 shows the X-ray emission in the inner region of the cluster (Böhringer et al., 1993) overlaid with a 332 MHz radio contours (Pedlar et al., 1990). Böhringer et al. (1993) first pointed out that X-ray cavities have a spatial correspondence with bright radio emission (e.g., Figure 1.7), suggesting evidence of interaction between the particles ejected by the central galaxy in the form of radio jets and lobes and the surrounding gas. Figure 1.7 shows an example where the radio lobes push out the gas, leading to regions with depleted (lower) gas densities and, therefore low X-ray emission (Fabian et al., 2002). The immediate vicinity of this displaced X-ray gas is surrounded by rims of high X-ray emission due to shocks (Heinz et al., 1998). However, the rims are cooler than the surrounding gas (Fabian et al., 2000; Feretti, 2007), which contradicts the idea that the radio lobes are providing heat to the cooling gas in the inner cluster region.

On the other hand, support for the interaction between radio lobes and the ambient gas as the origin of X-ray cavities is provided by the fact that the radio lobe energy density pressure is larger than the external gas pressure (Fabian et al., 1981; Pedlar et al., 1990).

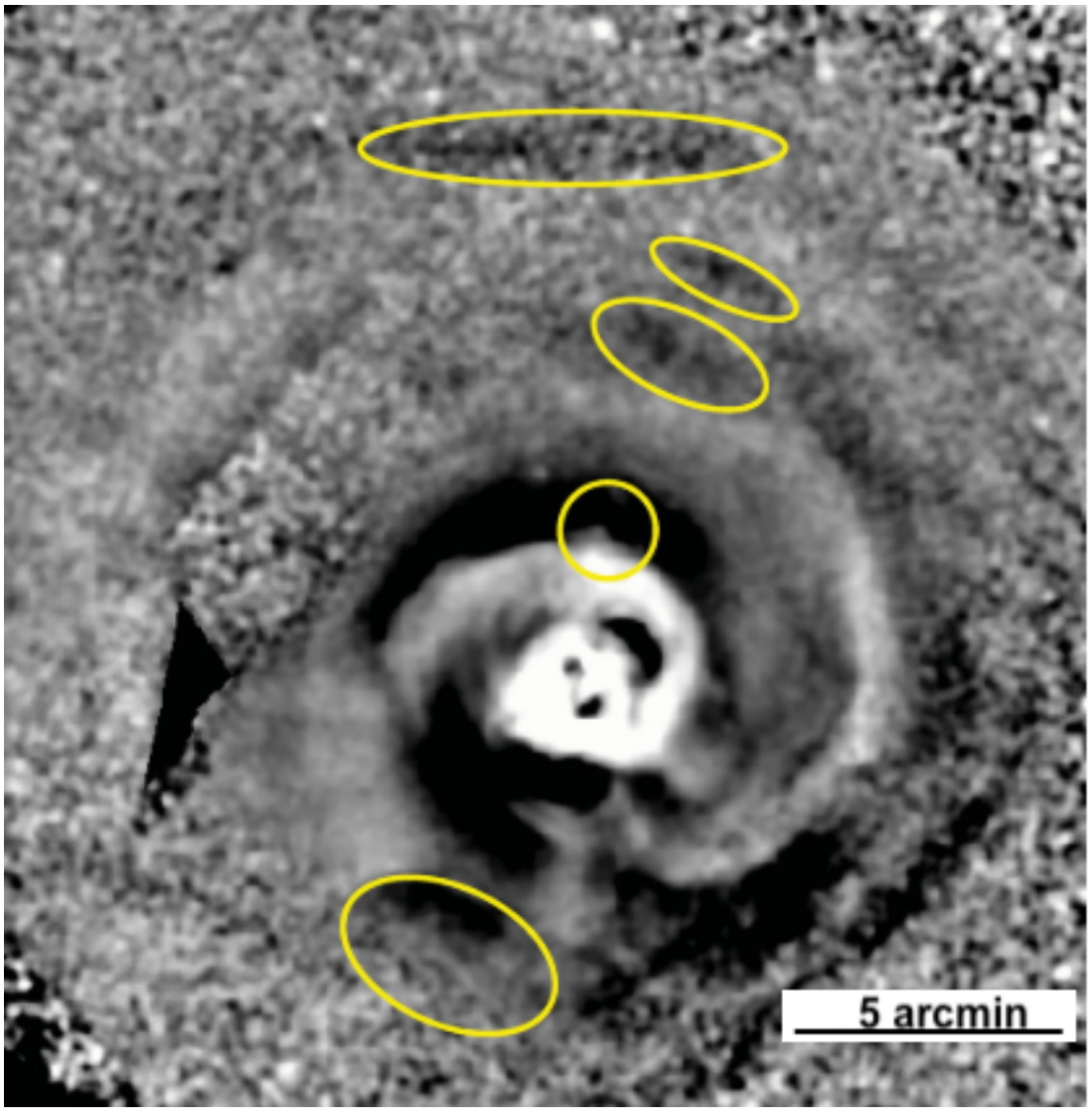

FIGURE 1.6: X-ray image of the Perseus cluster. From top to bottom, the five yellow circles show the locations of the northern trough, two buoyantly rising bubbles, the top of the Hα filament seen in optical observations and the south bay (Fabian et al., 2011, see text for details).

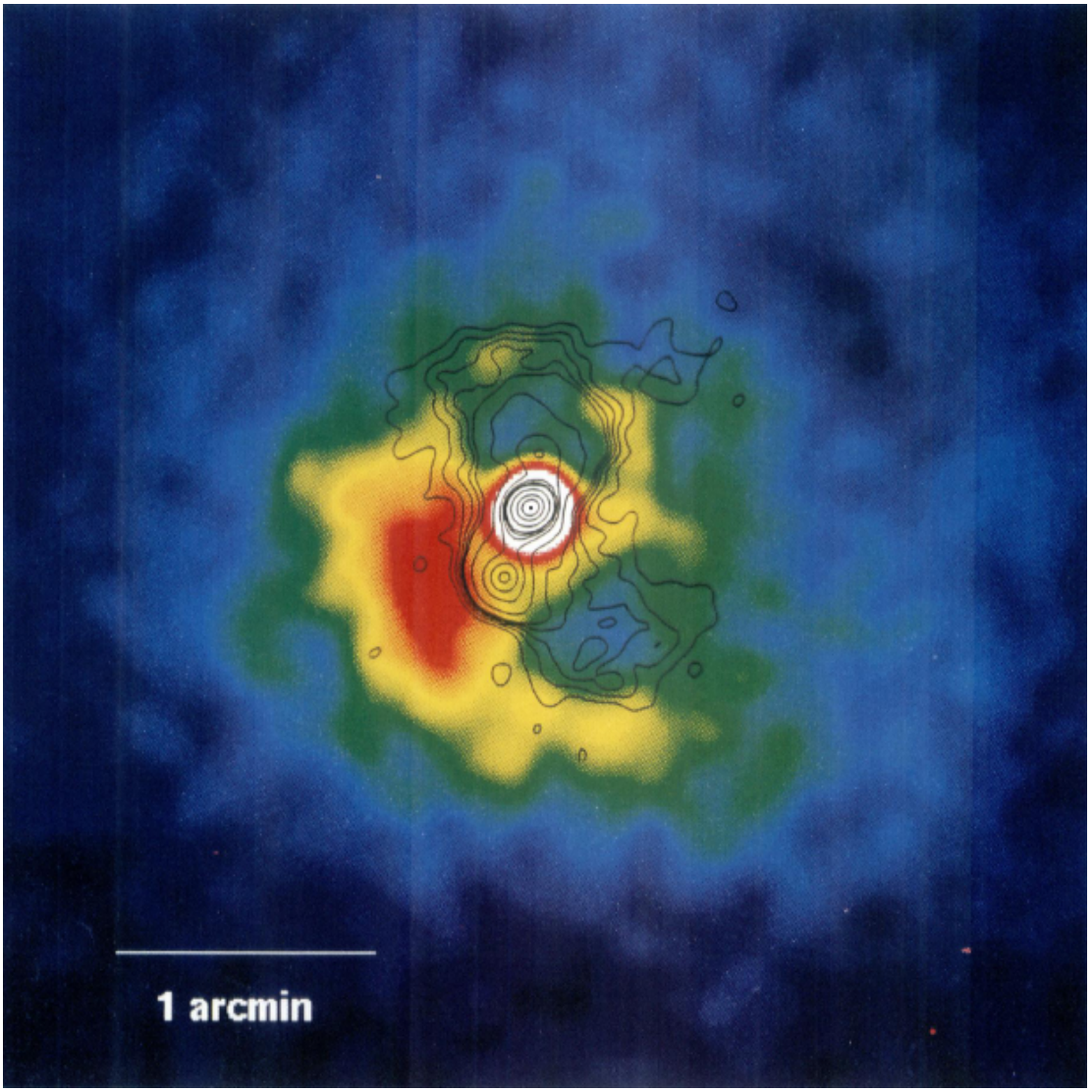

FIGURE 1.7: Radio contours at 332 MHz with a $\approx 5''$ resolution (Pedlar et al., 1990) overlaid on the X-ray ROSAT image of NGC 1275 (Böhringer et al., 1993). The inner X-ray holes coincide with the radio lobes from NGC 1275.

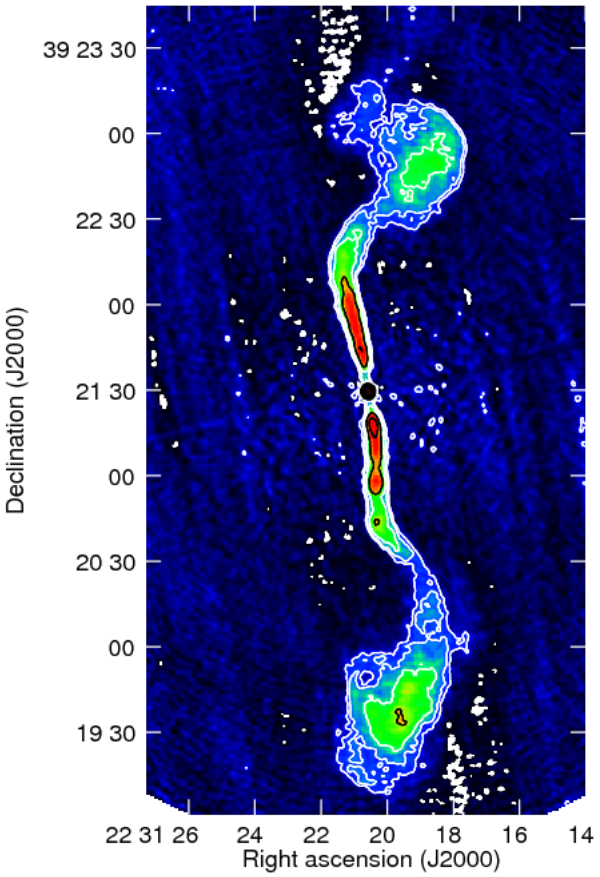

FIGURE 1.8: Fanaroff-Riley type I source 3C 449. The core is the brightest radio feature (from Kharb et al., 2014)

1.4 Radio Emission

Radio galaxies emit due to synchrotron emission, mostly coming from accretion of matter onto a central black hole. Fanaroff and Riley (1974) defined two main classes of radio galaxies:

- Fanaroff-Riley type I (FR I): sources whose brightness is dominated by the nuclear emission and with a monochromatic radio power at 1.4 GHz of $P_{1.4\ \mathrm{GHz}} \lesssim 10^{24.5}$ W Hz^{-1} (Figure 1.8);
- Fanaroff-Riley type II (FR II): sources whose brightness is dominated by lobe emission, with $P_{1.4\mathrm{GHz}} \gtrsim 10^{24-25}$ W Hz^{-1} (Figure 1.9).

FR I radio sources have jets that are usually visible on kpc scales and bright radio compact cores (Fanaroff and Riley, 1974; Kharb et al., 2014). Jets terminate in relatively faint lobes and/or elongated plumes.

When found in galaxy clusters, FR I lobes often coincide with cavities in the X-ray brightness distribution (see Section 1.3; McNamara and Nulsen, 2007; Gitti et al., 2012) and occasionally host thermal plasma (Croston and Hardcastle, 2014).

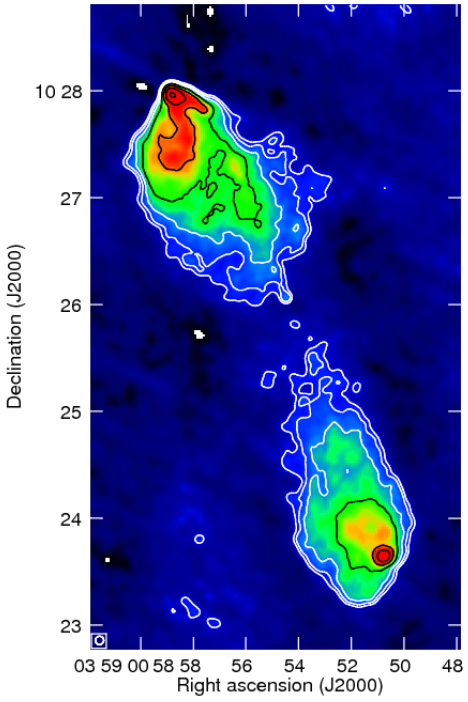

FIGURE 1.9: Fanaroff-Riley type II source 3C 98. The brightest, most noticeable features are the radio lobes (from Kharb et al., 2014)

FR II sources have fainter cores, very prominent radio lobes and are generally brighter than FR Is. Differences between FR I and FR II sources are likely environmental (Zirbel, 1997; Gopal-Krishna and Wiita, 2000; Gawroński et al., 2006; Miller and Brandt, 2009). Owen and Ledlow (1994) showed that the dichotomy in FR I and FR II radio power depends upon host galaxy optical luminosity, which is related to the size of the host galaxy. There is a clear separation with little overlap between FR I and FR II radio luminosities (Owen and Ledlow, 1994), with some overlap between the two classes occuring at $10^{24.5-26}$ W Hz^{-1} luminosities (Baum et al., 1995; Kharb et al., 2014).

As FR I sources have fainter lobes compared to FR II sources, it has been suggested that the FR I jets, which are sub-sonic at large scales, have a lower kinetic power than FR II jets and, therefore, remain less collimated in dense media (e.g. Ghisellini and Celotti, 2003; Marchesini et al., 2004). A more common interpretation is that jets are initially super-sonic in both FR types, but the FR I jets decelerate to sub-sonic speeds because of the environment, leading to inefficient energy transport from the core (Rudnick and Owen, 1976; Falle, 1991; Bicknell, 1994; Kaiser and Alexander, 1997; Nakamura et al., 2008). This interpretation is supported by observations of relativistic (super-sonic) jets within a kiloparsec from the central engine of FR I galaxies such as M 87 (Biretta et al., 1995), as well as observations of sources with an FR I type jet on one side and an FR II jet on the other (Gopal-Krishna and Wiita, 2000; Gawroński et al., 2006; Miller and Brandt, 2009). FR I sources also tend to be found in rich environments such as the central regions of rich galaxy clusters, compared to FR II sources (Zirbel, 1997; Wing and Blanton, 2011; Saripalli, 2012).

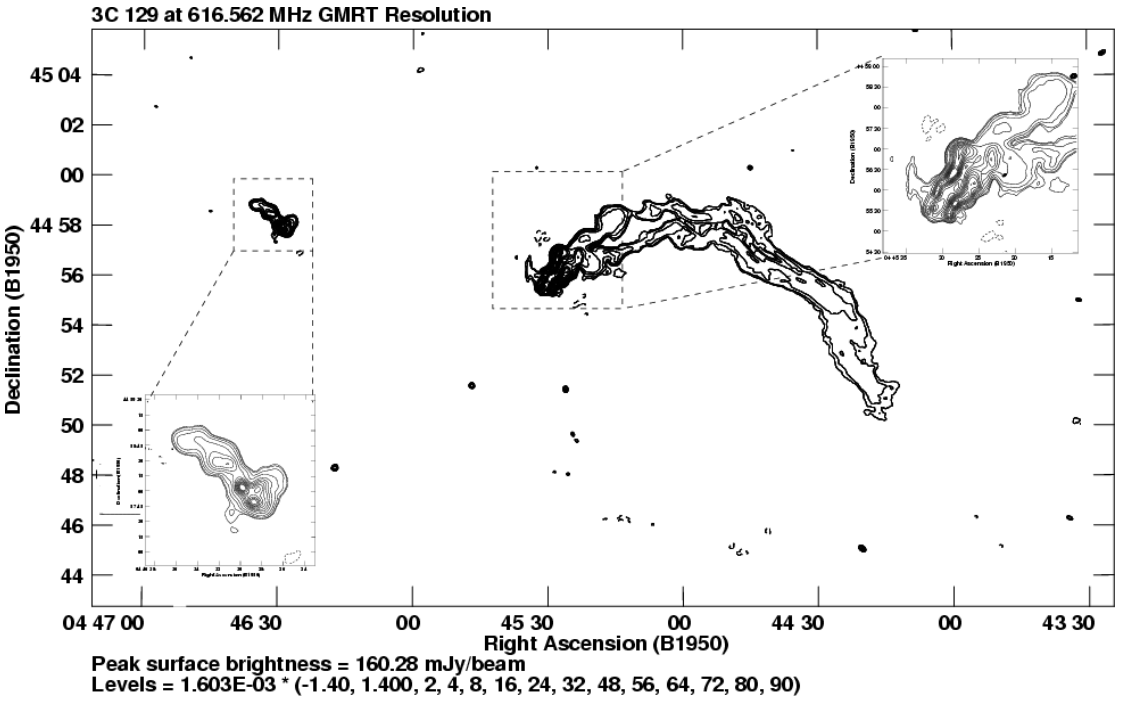

FIGURE 1.10: The head-tail radio galaxy 3C 129 observed at 49 cm with an angular resolution of $\sim 8.0''$ (Lal and Pramesh Rao, 2004).

1.4.1 Bent-Tailed radio sources

Bent-Tailed (BT) galaxies are radio sources whose jets and lobes are not linearly aligned with the galactic nucleus (Dehghan et al., 2014, Figure 1.10). They are classified as FR I sources, although their luminosities fall in the range of the FR I/FR II radio power overlap region (Dehghan et al., 2014; Johnston-Hollitt et al., 2014). They are preferentially observed in dense environments such as galaxy groups and clusters (Mao et al., 2009; Johnston-Hollitt et al., 2014).

The distinctive morphology of BT galaxies is understood to result from the effects of ram pressure due to the motion of the host galaxy through the dense intracluster medium (Gunn and Gott III, 1972; Miley et al., 1972; Dehghan et al., 2014). The galaxy ejects plasma beams while moving through a dense ICM and the interaction between the supersonic jets and the ICM slows the jet down, resulting in the asymmetric morphology that is characteristic of BT sources (Begelman et al., 1979).

A galaxy moving at speed $v_{\rm g}$ relative to an ambient medium of density $\rho_{\rm ICM}$ experiences a ram pressure $P_{\rm ram}$ (Miley et al., 1972; Sarazin, 1988):

$$P_{\rm ram} = \rho_{\rm ICM} v_{\rm g}^2 \text{ dyne cm}^{-2}. \tag{1.5}$$

If the ram pressure on the surrounding ICM due to the jets is comparable to the ram pressure on the galaxy itself due to its motion relative to the ambient ICM, the jets experience a curvature parametrized by its radius R (Begelman et al., 1979; Jones and Owen, 1979; Freeland and Wilcots,

2011; Mguda et al., 2015):

$$R = \rho_{\rm jet} v_{\rm jet}^2 \frac{h}{\rho_{\rm ICM} v_{\rm gal}^2}, \tag{1.6}$$

where h is the jet cylindrical radius, $\rho_{\rm jet}$ the internal density and $v_{\rm jet}$ the speed of material in the jet.

BT sources whose jets are well collimated within the inner tens of kpc before flaring into elongated, bent plumes, with opening angles of more than 90° are known as wide angle tails (WATs) (Owen and Rudnick, 1976; Sarazin, 1988; Sijbring and de Bruyn, 1998; Dehghan et al., 2014). BT sources whose entire radio emission lies entirely on one side of the host optical galaxy are known as narrow angle tails (NATs) or head-tail (HT) galaxies (Ryle and Windram, 1968; Sarazin, 1988; Dehghan et al., 2014).

1.4.2 Diffuse emission

In addition to radio emission associated to galaxies, galaxy clusters also host extended diffuse emission that has no optical counterpart and thus can not be attributed to any particular galaxy (Willson, 1970; Giovannini and Feretti, 2002). This diffuse synchrotron emission provides evidence for the existence of large-scale magnetic fields in galaxy cluster environments.

Based on its morphology, location and dynamical state of the host cluster, the synchrotron diffuse emission is generally grouped into (Giovannini and Feretti, 2002; Feretti et al., 2012; Kale et al., 2016):

- Radio Halos (RH): steep spectrum sources ($\alpha \gtrsim 1$) with a regular morphology and Mpc linear size, with radio power of order $P_{1.4\ \rm GHz} \approx 10^{24}$ W Hz^{-1},
- Radio Relics (RR): located at the cluster periphery, highly polarised (up to 30%) megaparsec-scale sources with characteristic radio powers in the range of $10^{23} - 10^{25}$ W Hz^{-1} (Venturi, 2011);
- Mini Halos (MH): Morphologically regular, steep spectrum ($1.2 \leq \alpha \leq 1.6$) sources (Giacintucci et al., 2014a; Kale et al., 2015; Omar, 2019), usually surrounding the central galaxy in a few CC clusters (Burns et al., 1992), with a characteristic largest linear size of ~ 500 kpc (Cassano et al., 2008).

1.4.2.1 Radio Halos

RHs are found in the central regions of galaxy clusters and show a spatial correspondence with the X-ray emission (Figure 1.11).

RHs are not ubiquitous and are found in $\sim 30\%$ of clusters with $L_{\rm X\ [0.1-2.4\ keV]} \gtrsim 5\times10^{44}$ erg s^{-1}. This number rises to $\sim 40\%$ for clusters with $L_{\rm X} \gtrsim 8\times10^{44}$ erg s^{-1} (Venturi et al., 2008; Cassano et al., 2011). Their 1.4 GHz power correlates with mass: it has been found that RH radio power and the host cluster's mass correlate as $P_{1.4\ \rm GHz} \propto M^{2.3}$, where M is the gravitational mass within the radius $3\left(\frac{H_0}{50}\right)^{-1}$ Mpc, for clusters with $10^{14.8} \leq M \leq 10^{15.5}\ M_\odot$ (Govoni et al., 2001;

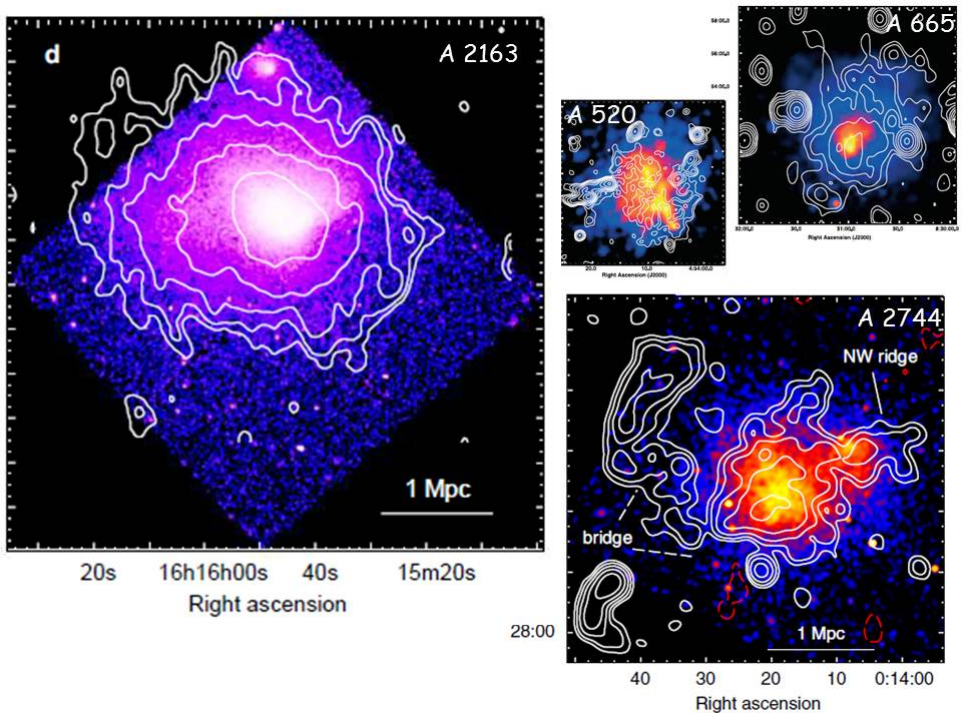

FIGURE 1.11: Examples of RHs (contours overlaid onto the X-ray images). Note the spatial morphology corresponding with the X-ray emission (from Brunetti and Jones, 2014).

Feretti, 2003). This correlation was found to be slightly steeper when mass within the virial radius was used (Brunetti and Setti, 2018).

Radio halos are generally found in unrelaxed clusters. Cassano et al. (2013) found a bimodal correlation between the cluster radio power and their mass: more massive clusters that underwent more merging events host a RH whereas less massive ones do not. This correlation between the presence of a RH (and its power) and the merging history of a cluster supports the evidence that RHs are originated by relativistic electrons accelerated via merging-induced turbulence (Brunetti et al., 2001, 2008).

1.4.2.2 Radio Relics

Radio relics are also diffuse sources with no optical counterpart, but mostly located away from the cluster centre (few hundred megaparsecs projected distance). Unlike RHs, RRs have elongated shapes with sizes generally up to a few hundreds kpc. They typically have radio luminosities below 10^{24} W Hz^{-1} (Feretti et al., 2012; Vazza et al., 2012). Some radio relics have been observed symmetrically located on either side of the host cluster (Feretti, 2005; Bagchi et al., 2006; Bonafede et al., 2009, 2014, e.g., Figure 1.12).

RRs are also linked to the dynamical history of the cluster, generated by particles reaccelerated by shocks (Botteon et al., 2016).

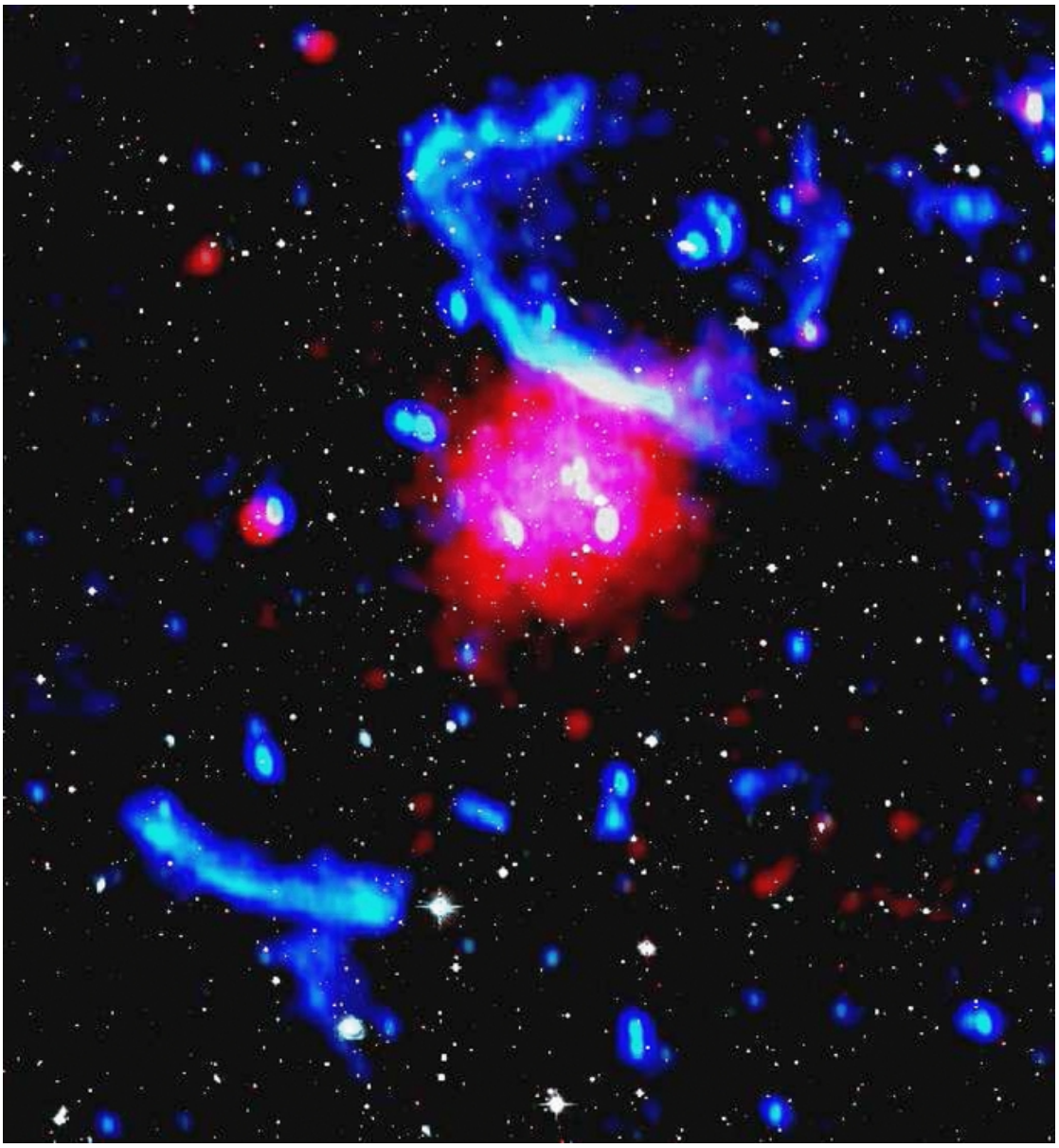

FIGURE 1.12: Double radio relic in the galaxy cluster PLCKG287.0+32.9. Red colour indicates the X-ray emission, while the blue and green indicate low ($22'' \times 18''$) and high ($13'' \times 8''$) resolution radio images, respectively (from Bonafede et al., 2014)

1.4.2.3 Mini Halos

Mini halos are a class of diffuse radio sources similar to RHs, but smaller in size, generally only a few hundred kpc large (Cassano et al., 2008), and found only in CC clusters. Conversely, only 50% of CC clusters host MHs (Kale et al., 2013, 2016). Only 21 MHs are currently known (Giacintucci et al., 2014a; Bravi et al., 2016).

They have steep spectral indices, typically in the range of $1.2 \leq \alpha \leq 1.6$ (Giacintucci et al., 2014a; Kale et al., 2015; Omar, 2019), with radial steepening found in some mini-halos, examples of which include the mini-halos in Perseus (Gitti et al., 2002) and Abell 2626 (Gitti et al., 2004).

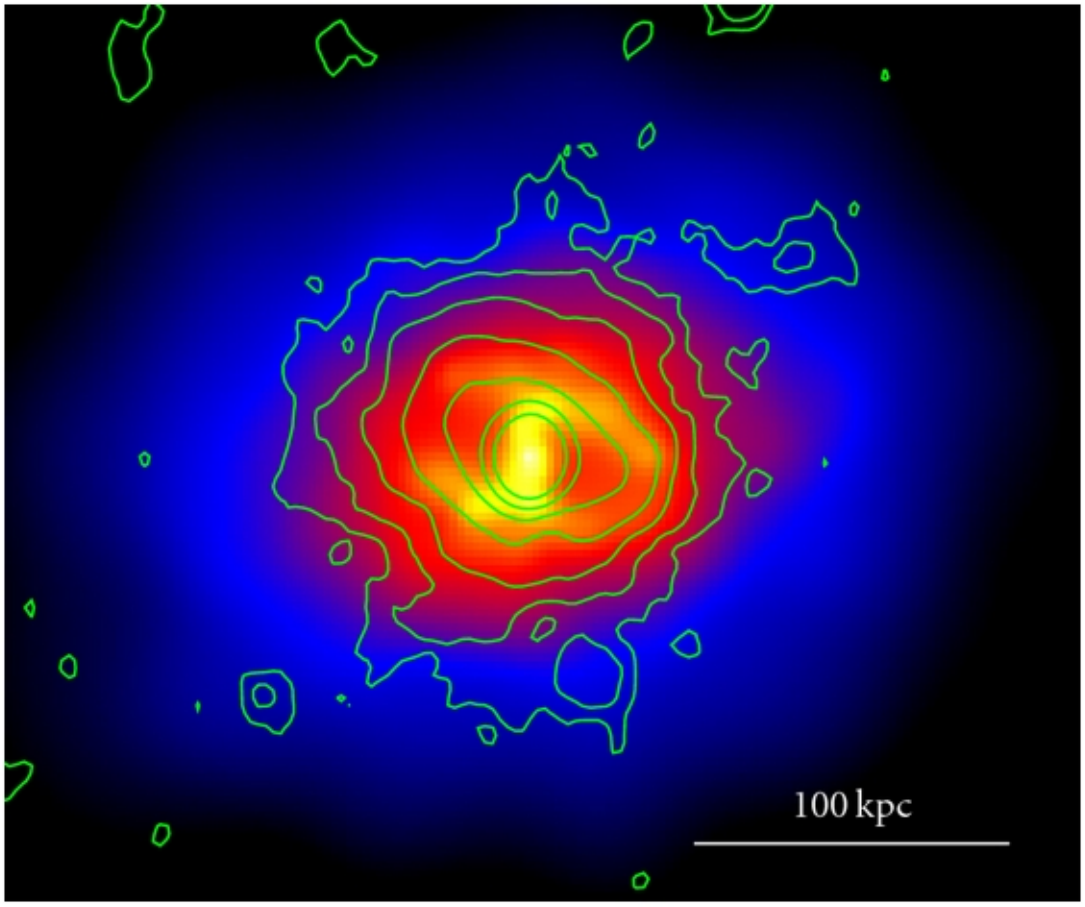

FIGURE 1.13: Mini halo in galaxy cluster RBS 797 (1.4 GHz radio contours overlaid on the X-ray image, from Gitti et al., 2012).

Unlike RHs, MHs are found in relaxed clusters and are not directly connected to the cluster merging history and there is yet no convincing explanation for their origin. Gitti et al. (2002) argued that if MHs are the consequence of relativistic particles ejected by the central AGN they should be unlikely to be observed due to the increased radiation losses following the magnetic field compression due to the cooling flow. They suggested that particles are reaccelerated in-situ via turbulence induced by the cooling flow. Support for this picture would come from the correlation found between the MH radio power and the cooling flow power (Gitti et al., 2012, 2004; Bravi et al., 2016, see Figure 1.14).

On the other hand, since the classical CF picture may be untenable, as mentioned in Section 1.3, alternative sources of energy may be required to induce turbulence for the in-situ particle reacceleration in the Gitti et al. (2002) model. Minor mergers (Gitti et al., 2007; Govoni et al., 2009) have been found to induce gas sloshing around the cores of cool-core clusters (ZuHone et al., 2013), generating significant turbulence (Mazzotta and Giacintucci, 2008) which could provide the energetics for particle reacceleration in lieu of, or possibly in addition to, cooling flows (Cassano et al., 2008).

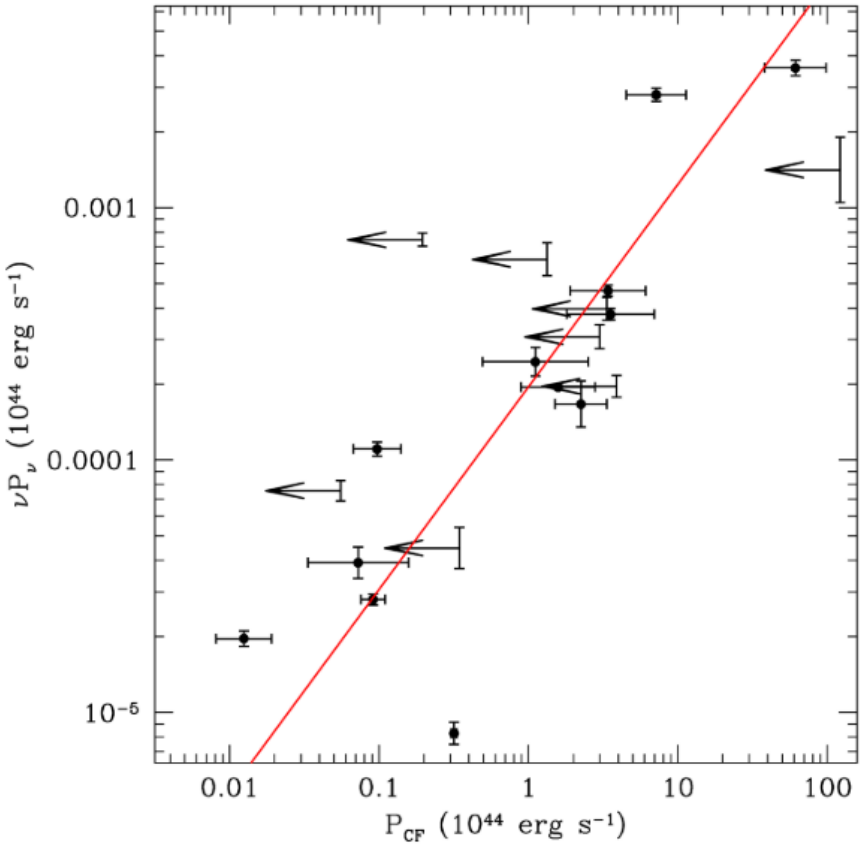

FIGURE 1.14: Correlation between the MH radio power and the cooling flow power. The red line represents the best fit and arrows indicate upper limits (Gitti et al., 2004; Bravi et al., 2016).

1.5 Radio emission in the Perseus cluster

1.5.1 3C 84

The brightest radio source in the Perseus galaxy cluster is named 3C 84 according to the third Cambridge Catalogue of Radio Sources (Edge et al., 1959) and is associated with the giant elliptical galaxy NGC 1275.

On arcsecond angular scales, 3C 84 is composed of an unresolved core and several emission "knots" that are jets emanating from the core (Figure 1.15; Miley et al., 1975; Pedlar et al., 1983). The radio knot south of the core is brighter than the northern one, which implies that 3C 84 is morphologically an asymmetric FR I source, with a $\sim 10^{25}$ W Hz^{-1} radio luminosity that falls within the intermediate classification between FR I and FR II (Pedlar et al., 1990; Baum et al., 1995; Kharb et al., 2014). 3C 84 is a characteristic example of the interaction between the lobes of a radio galaxy and the ICM, leading to the co-location of radio lobes and X-ray cavities (Section 1.3). About 20″ away from the core, the source morphology changes noticeably and the radio lobes bend significantly due to the interaction with the thermal gas (Figure 1.16). Böhringer et al. (1993) suggest that the jets sweep up gas along their path, generating regions

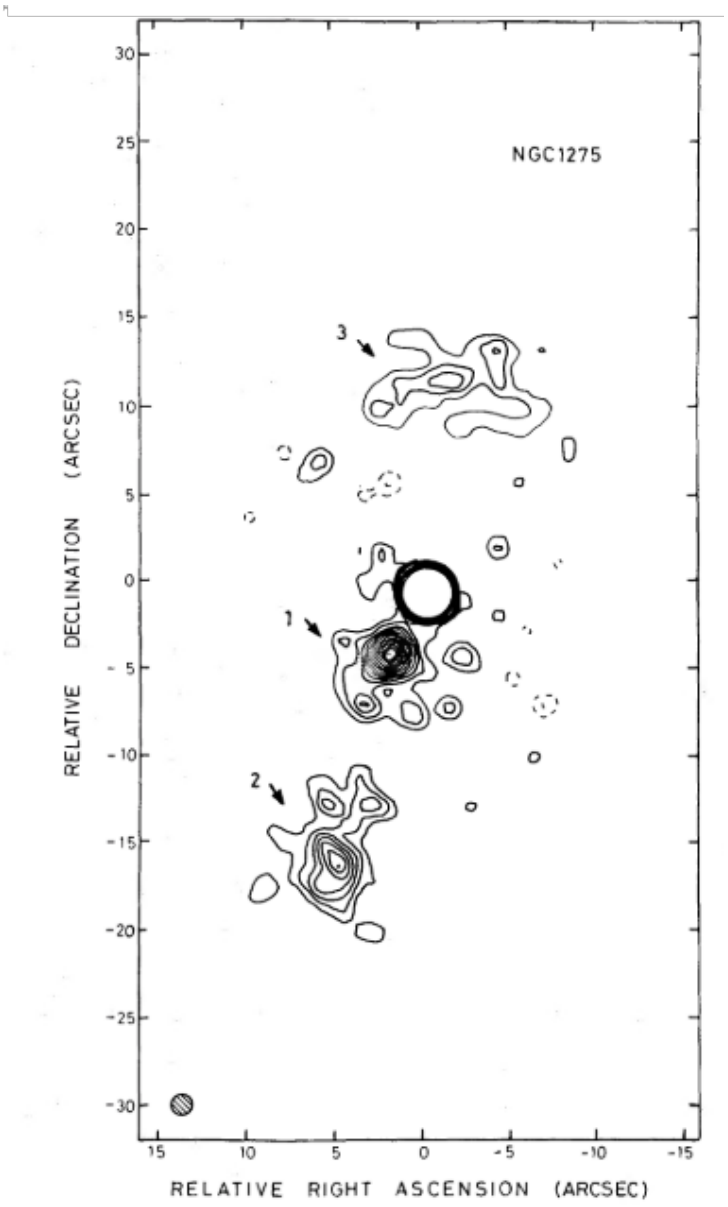

FIGURE 1.15: 410 MHz image of 3C 84. The contours run from ±11.9 up to 238 mJy beam^{-1} spaced by 11.9 mJy beam^{-1}. The angular resolution is 1.2″. Numbers indicate the core and the knots of emission (Pedlar et al., 1983).

of enhanced X-ray emission like the south-eastern blob in Figure 1.16 which, in turn, causes jets to bend.

At low radio frequencies, another pair of outer lobes become visible ∼ 25 kpc to the north-west and 45 kpc to the south-south-east of the core respectively (see Figure 1.17; Fabian et al., 2000; Blundell et al., 2002). Like the inner lobes, these outer radio lobes result from the interaction with outer thermal gas and are likely older jets that have suffered synchrotron radiative losses and, therefore, are no longer visible at higher radio frequencies (Churazov et al., 2000; Fabian et al., 2002).

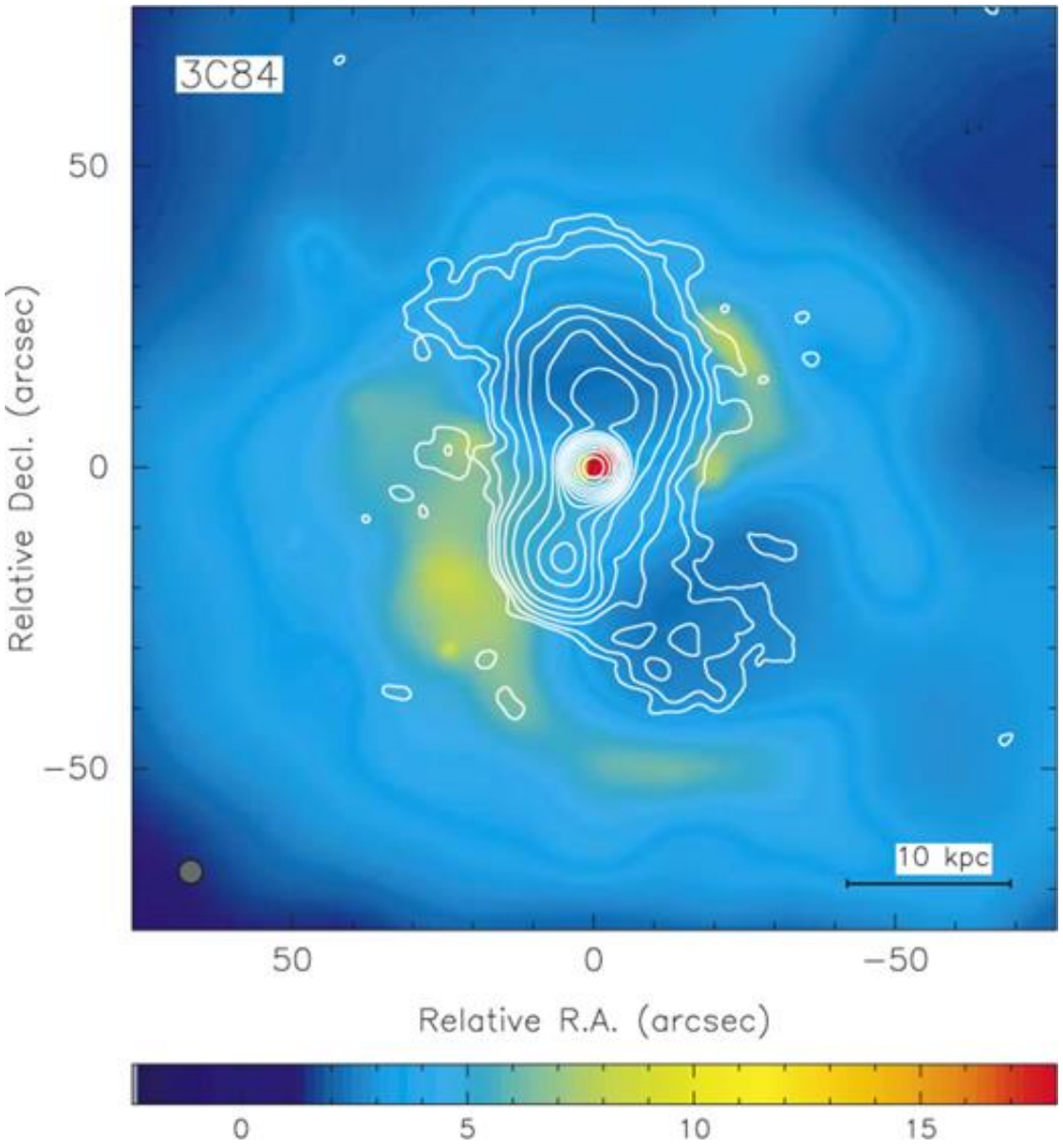

FIGURE 1.16: Radio contours around 3C 84 at 1.4 GHz overlaid on the X-ray image (0.5 – 7 KeV). Radio contours are drawn at 1 up to 21.7 Jy beam^{-1} increased by a factor of 2. The southern radio lobe can be seen to bend eastwards due to the interaction with a region of X-ray emitting plasma (from Fabian et al., 2000).

The radio spectral index α[4] in the lobes ranges from $\alpha \sim 0.7$ in the inner regions to $\alpha \sim 1.5$ in the outer regions (Pedlar et al., 1990; Gitti et al., 2003) and their age has been estimated to be 10^7 yr (Fabian et al., 2002, 2003). With the standard assumption of energy equipartition between particles and magnetic field (Ginzburg and Syrovatskii, 1965), the particles in the inner parts of the radio lobes have energy density values ranging from $\sim 10^{-10}$ to 10^{-9} erg cm^{-3}, which is comparable to the energy density of the external thermal gas ($\sim 2 \times 10^{-10}$ erg cm^{-3}), thus the radio lobes have enough pressure to displace the X-ray emitting thermal gas (Pedlar et al., 1990; Böhringer et al., 1993).

[4]We will use the notation $S_\nu \propto \nu^{-\alpha}$, S_ν is the flux density at the frequency ν.

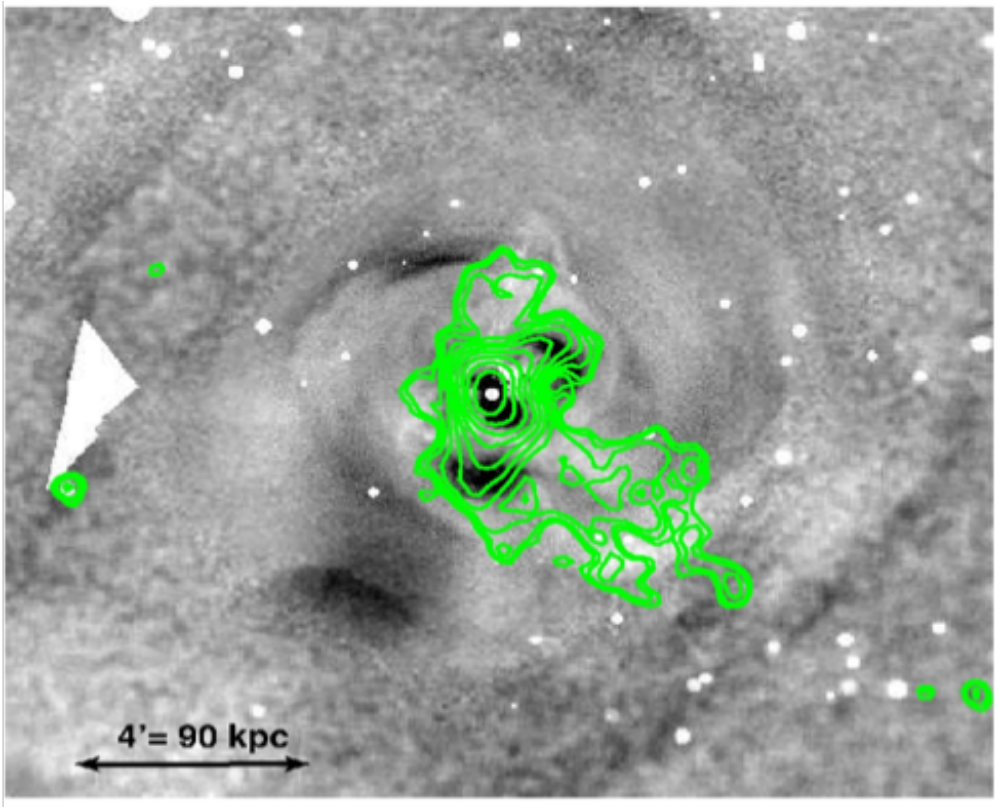

FIGURE 1.17: 74 MHz radio contours of the Perseus cluster (Blundell et al., 2002) overlaid on the X-ray Chandra image (Fabian et al., 2011). Contours range from 0.3 to 36.2 Jy beam^{-1} with logarithmic increments. The angular resolution of the 74 MHz observation is 24″. Image credit: Gendron-Marsolais et al. (2017).

Accretion onto the supermassive black hole at the core of 3C 84 releases power of order 10^{45} erg s^{-1} through the jets and the lobes (Heinz et al., 1998). This process which is known as radio-mode feedback (Birzan et al., 2004; Dunn et al., 2006; Gendron-Marsolais et al., 2017), provides a method of transporting energy from the core to balance radiative energy losses in the ICM. The details of the energy distribution remain, however, still uncertain (Fabian et al., 2006). Outstanding questions include how the energy output can be so fine-tuned as to balance cooling without dispersing the observed dense gas cores in CCs (Böhringer and Werner, 2010), how the energy can be dissipated in a roughly isotropic manner in the ICM (Fabian et al., 2017), why the coolest gas in X-ray maps is found closest to the radio lobes (McNamara and Nulsen, 2007), as well as the nature of the jets and how efficiently they transport energy from the nucleus (McNamara and Nulsen, 2007). Shocks/turbulence and/or sound waves may provide an efficient method of energy transport, and sound waves with the velocities consistent with the requirements of the feedback models have been recently observed in the Perseus cluster (see Fabian et al., 2017), but details of the feedback picture remain uncertain (McNamara and Nulsen, 2007).

1.5.2 3C 83.1 B

One of the Perseus galaxy cluster's most remarkable attributes is the many BT radio sources, 3C 83.1 B, IC 310, CR 15, CR 10 and T 74 (Miley et al., 1972; Sijbring and de Bruyn, 1998,

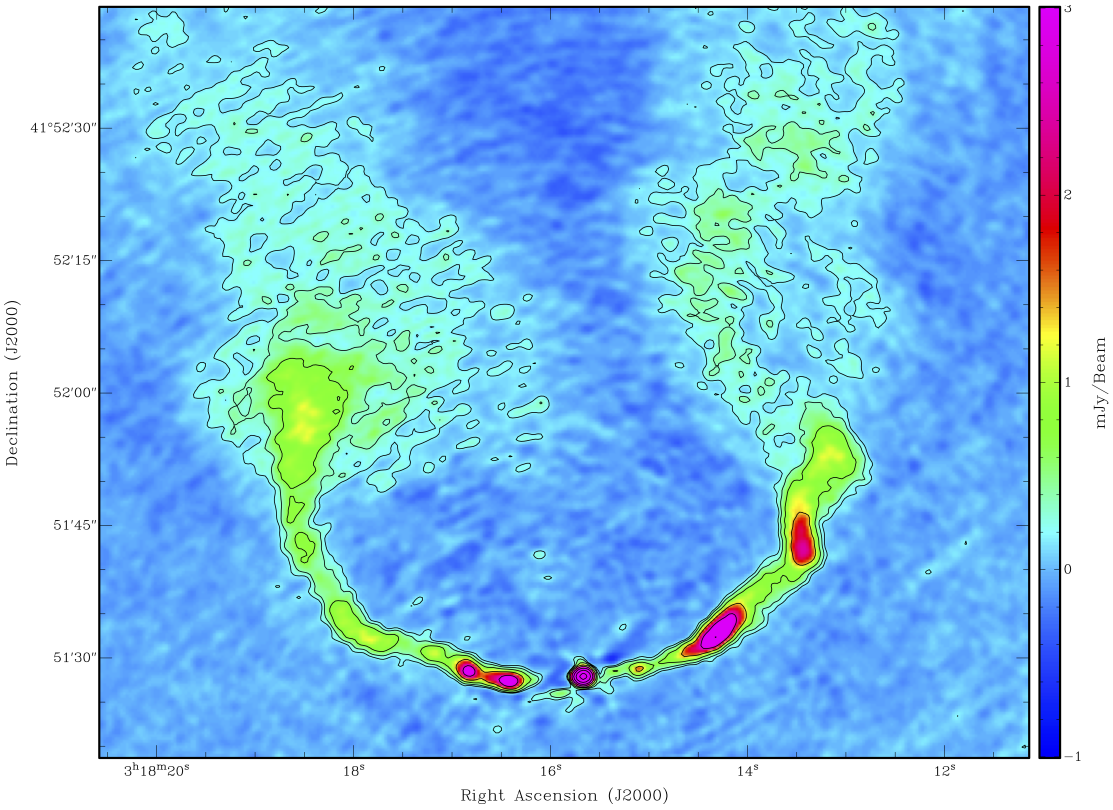

FIGURE 1.18: VLA total intensity contour map of 3C 83.1 B at 5 GHz. The image has a resolution of 1.40″. The East and West surface brightness knots are seen along the jet regions on either side of the galactic nucleus. Image adapted from: NRAO/VLA Archive Survey, 2005/2006 AUI/NRAO

and references therein). All the known BTs in the Perseus cluster are head-tail sources and the archetypical HT, 3C 83.1 B (Ryle and Windram, 1968; O'Dea and Owen, 1986) which is located $\sim 12°$ to the northwest of 3C 84, stands out due to its brightness and size.

Figure 1.18 shows the morphology of 3C 83.1 B at 5 GHz. There is an unresolved nucleus in the south of the image, with a pair of jets protruding on either side of the nucleus, initially along the east-west axis. The jets' angle of advance gently changes until they are both oriented northwards, opposite the galaxy's direction of motion.

Along the jets are a few regions of high brightness emission, known as surface brightness knots. The distribution of the knots along the jets is asymmetric, with the west jet having more widespread knots, which also appear brighter.

In general, the surface brightness along the jets of 3C 83.1 B starts off faint, with $I_{5\mathrm{GHz}} = 0.1$ mJy arcsec^{-2} within the inner 3 kpc of the east jet and the inner 2 kpc of the west jet. The first surface brightness knots along the jets are located at these distances from the core, at which point the surface brightness increases by a factor of ~ 20 in the east and by a factor of ~ 7 in the west jet. Besides this, there is no discernible correlation between the surface brightness and the projected distance from the core along the jets (O'Dea and Owen, 1986).

The spectral index measured along 3C 83.1 B is in the range of 0.5 - 0.8 (Ryle and Windram, 1968) with a gentle distance-dependent steepening (Feretti et al., 1998) at intermediate frequencies

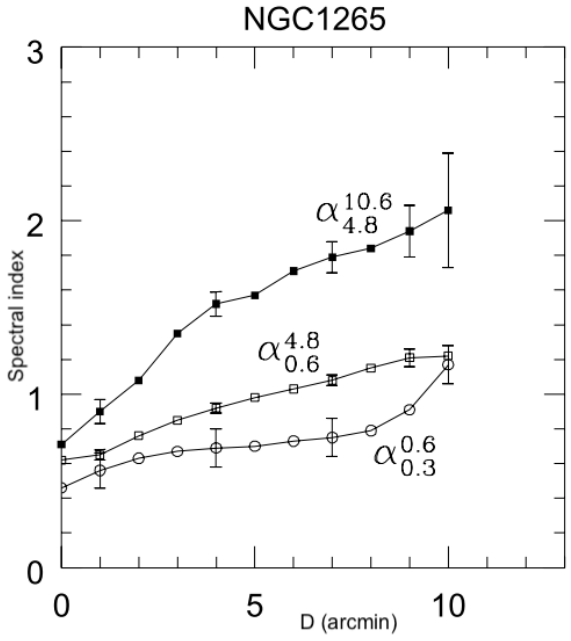

FIGURE 1.19: Spectral index vs. distance from the nucleus of 3C 83.1 B. The circles, empty boxes and filled boxes represent spectral indices calculated at $0.3 - 0.6$ GHz, $0.6 - 4.8$ GHz and $4.8 - 10.6$ GHz respectively (Feretti et al., 1998)

(300 MHz $\lesssim \nu \lesssim$ 5 GHz). As shown in Figure 1.19, a strong spectral steepening which increases with distance from the nucleus is seen at $\nu > 5$ GHz, with the spectral index reaching up to $\alpha^{10.6\ \mathrm{GHz}}_{4.8\ \mathrm{GHz}} > 2$ at the end of the tail $\sim 10'$ from the core (Feretti et al., 1998).

Since the synchrotron emitting electrons originate from the nuclear core, the electrons located further from the nucleus are expected to be the oldest. The electron population in the tails, which is furthest from the core, must be at pressure equilibrium with the surrounding gas. We also expect the spectrum to steepen with distance along the tails (Miley, 1973; Feretti et al., 1998). Moreover, the energy losses due to synchrotron and IC radiation are proportional to E^2 (Sijbring and de Bruyn, 1998), thus the steepening must be stronger at higher frequencies since the most energetic electrons get depleted first. The spectral index gives the source's synchrotron spectrum and the break frequency (ν_{br}) which, together with the magnetic field strength, can be used to determine the radiative age of the synchrotron emitting particles (Pratley et al., 2013). The particle age in a population suffering both synchrotron and inverse Compton radiative losses is given for the Jaffe-Perola model by (Jaffe and Perola, 1973; Alexander and Leahy, 1987; Feretti et al., 1998):

$$t = 1590 \frac{H_{\mathrm{eq}}^{0.5}}{H_{\mathrm{eq}}^2 + H_{\mathrm{CMB}}^2} [\nu_c (1+z)]^{-0.5} \ \mathrm{Myr}, \tag{1.7}$$

where ν_{c} is the break frequency in GHz, H_{eq} is the equipartition magnetic field in μG and $H_{\mathrm{CMB}} = 3.25(1+z)^2$ μG is the equivalent of the Cosmic Microwave Background at redshift z. The radiative age of NGC 1265 is estimated out to $\sim 10'$ ($\sim$ 215 kpc) to be 6.7×10^7 yr for electrons with an average speed of $\sim$ 3000 km s^{-1}, which increases with distance, up to $7'$ from the core (Feretti et al., 1998). This age is of the same order as those derived for similar sources (Feretti et al., 1990; Andernach et al., 1992) and predictably less than the age found for

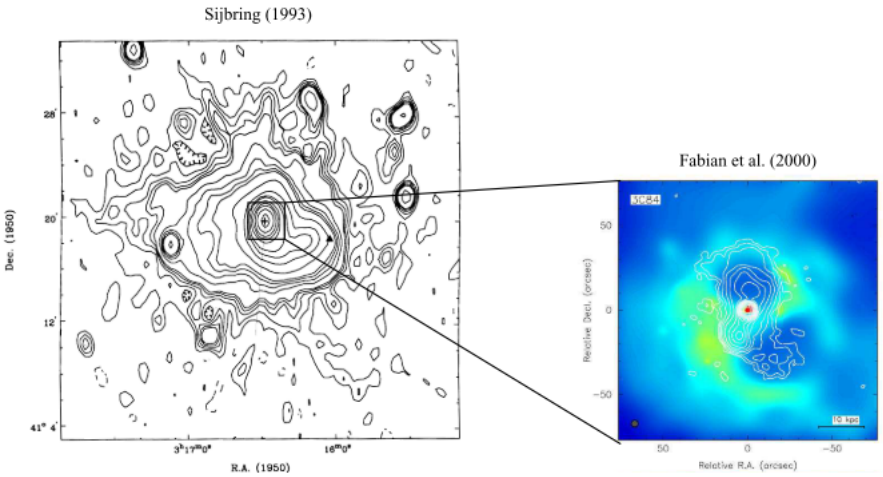

FIGURE 1.20: 327 MHz image of the Perseus cluster mini-halo at a resolution of $51'' \times 77''$, centred on NGC 1275 (Sijbring, 1993)[5]. Inset: 1.4 GHz radio contours overlaid on the X-ray image of the core (Fabian et al., 2000). Image credit: Gitti et al. (2003)

IC 711, the longest known HT (Vallee and Roger, 1987), of 2.2×10^8 yr (Srivastava and Singal, 2016) at $\sim$ 700 kpc from the nucleus. However, at large distances from the core, Feretti et al. (1998) found localised regions with speeds significantly higher than the average estimates (up to 6000 km s^{-1}), which could be due to projection effects, bulk motion of electrons along the source, or the presence of reacceleration processes.

Lower frequency maps of 3C 83.1 B have shown that the source's tails extend much further beyond the structure discernible in the high frequency maps. At 49 cm - 92 cm, after initially bending westwards, Sijbring and de Bruyn (1998) find that the merged tails bend eastwards at an angle of almost 90°. The faint part of the tail appears to have a constant brightness distribution with distance, which implies that the oldest electrons are still energised by some process. In-situ re-acceleration could provide an explanation for this phenomenon as well (Sijbring and de Bruyn, 1998). The deduced total length of the tail at low frequencies is up to 1.1 Mpc, which, at the extremities of the tail, avails a population of old relativistic electrons on which to test re-acceleration models (Sijbring and de Bruyn, 1998).

In addition, Sijbring and de Bruyn (1998) detect faint emission with a peak intensity of 15 mJy in a 92 cm image ahead of NGC 1265's direction of motion and conclude that it is emitted by a bow shock resulting from 3C 83.1 B's supersonic motion through the ICM. This low-level emission has also been previously located throughout the cluster's inner regions (Sijbring and de Bruyn, 1998), which could imply that the cluster is filled with these aged electrons. In the context of re-acceleration models, these aged electrons could eventually be re-energised by galactic wakes, shocks or other sources that distribute energy into the ICM.

1.5.3 The Mini-halo

[5] https://www.worldcat.org/title/radio-continuum-and-hi-line-study-of-the-perseus-cluster/oclc/492502184

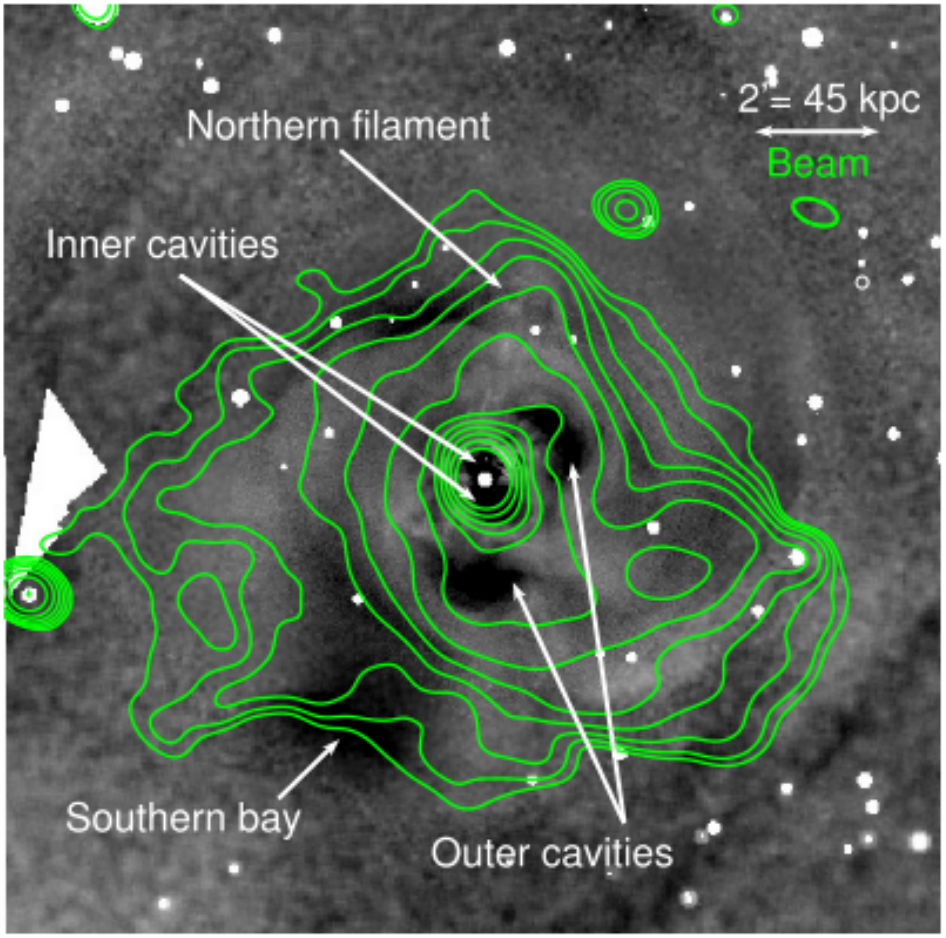

FIGURE 1.21: $270 - 430$ MHz contours running from 1.75×10^{-3} to 1 Jy beam^{-1} (Gendron-Marsolais et al., 2017) overlaid on the X-ray emission (Fabian et al., 2011).

The Perseus cluster is one of the galaxy clusters in which diffuse radio emission was first detected and it hosts the prototypical MH (Miley et al., 1975; Pedlar et al., 1990; Burns et al., 1992; Feretti et al., 2012). The MH emission surrounds 3C 84 (Figure 1.20), up to the cooling radius in the cluster inner regions and extending beyond ~ 100 kpc[6] from the core of NGC 1275 at low radio frequencies ($230 \leq \nu \leq 470$ MHz; Gendron-Marsolais et al., 2017). The MH spectral index steepens with distance from the cluster centre, with $\alpha \sim 1.1$ around 30 kpc up to $\alpha \sim 2.3$ at ~ 170 kpc, indicating radiative losses.

The Gitti et al. (2002) model suggests that the re-acceleration can be powered by energy from the cooling flow. In Section 1.4.2.3 it is shown in Figure 1.14 that the radio power of a mini halo correlates with the cooling flow power. Gitti et al. (2003) also show that the cooling flow power is significantly more than the observed integrated radio power of the mini halo in the Perseus cluster, suggesting that there is enough energy in cooling flows to re-accelerate the electrons of the MH.

[6]The radius is estimated using the minimum and maximum radii as $R_{\rm MH} = \sqrt{R_{\rm min} \times R_{\rm max}}$ (Giacintucci et al., 2014b).

In recent times, evidence for gas sloshing has been found in simulations (ZuHone et al., 2013) and X-ray observations (Fabian et al., 2011). This suggests that relic electrons which originated from the central AGN may be reaccelerated by turbulence from this gas sloshing. Some support for this hails from the correlation between the MH in the Perseus cluster and the underlying X-ray gas' morphology (Fabian et al., 2011). As evident in Figure 1.21, the counter-clockwise spiral structure of the gas temperature and brightness distribution in X-ray maps matches the morphology of the mini halo.

With better resolution telescopes, future observations will be able to better constrain the degree to which the X-ray structure in CC clusters affects the morphology of the MHs and which particular mechanisms are responsible for re-energising relic electrons in the cooling region.

1.6 Thesis motivation and goals

The original motivation of the observations used in this thesis was a pioneering radio study of the intracluster medium of the Perseus cluster, considered a testbed for the following scientific cases:

- the study of the gas density far out into the cluster outskirts where X-ray observations are no longer a sensitive probe due to their quadratic dependence on the gas density. A linear probe of the gas density (i.e., more sensitive to the low density regions) is the Thomson scattering of radio emission (Sunyaev, 1982; Wise and Sarazin, 1990; de Bruyn and Brentjens, 2005) that can be probed by radio polarization observations;
- the interplay between AGNs and the ICM. This interplay has already been unvelied in the Perseus cluster (Fabian et al., 2000), however, very sensitive polarization observations can further probe this interplay on a larger, cluster scale.

These observations were carried out with the Westerbork telescope but never, eventually, published. In this thesis we take a first step towards the aforementioned goals and analyse 24 hours of Westerbork observations on two pointings covering the Perseus cluster. The two pointings were needed to include 3C 84 and 3C 83.1 B, respectively, since the Perseus cluster field is bigger than the primary beam of a single pointing of the Westerbork telescope at 1.4 GHz.

Chapter 2

Introduction to interferometry

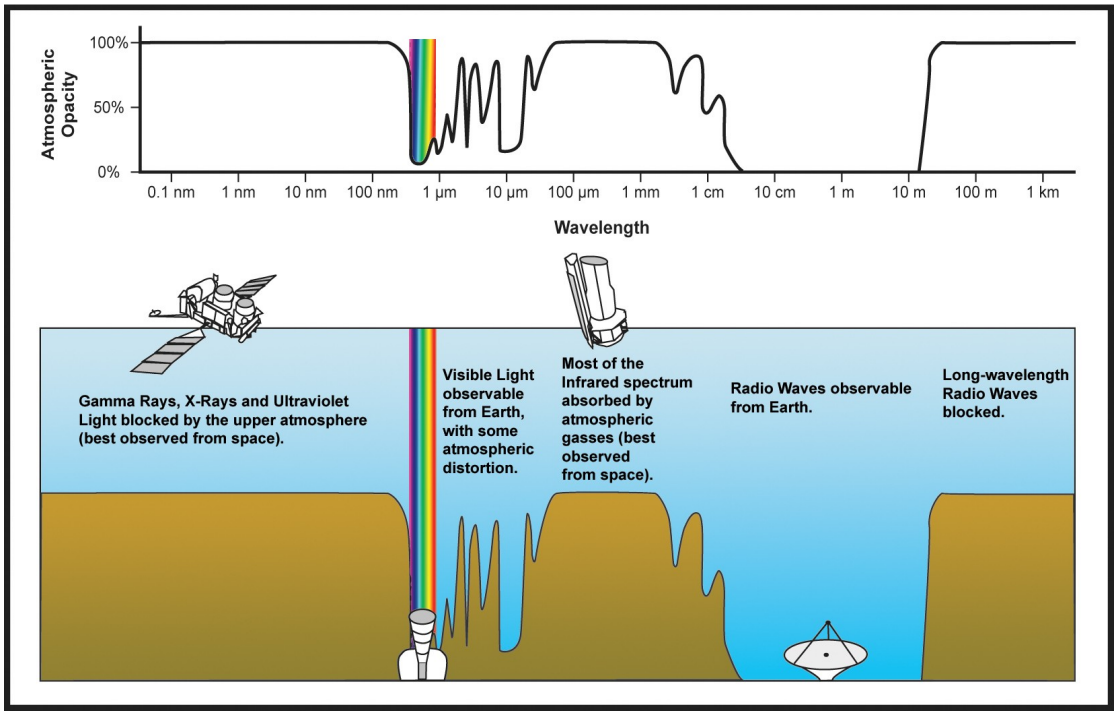

FIGURE 2.1: Atmospheric opacity as a function of observing wavelength. The opacity dips in the wavelength range between $\sim$ 5 mm and $\sim$ 20 m roughly corresponds to the radio window. credit:[1]Drugonot (2007).

The Earth atmosphere is opaque at most wavelengths, but mostly transparent in the radio window, between 15 MHz (20 m) and 60 GHz (5 mm, see Figure 2.1) (Condon and Ransom, 2016; Orfanidis, 2016). Radio telescopes are designed and built to receive radio waves and generally comprise of a large, parabolic dish, which focuses incoming radio waves to a front-end receiver, which then collects the radio waves for further analysis.

[1]https://commons.wikimedia.org/wiki/File:Atmospheric_electromagnetic_transmittance_or_opacity.jpg

The angular resolution $\theta_{\rm res}$ of a telescope describes the minimum angular distance between two objects that the instrument is able to distinguish and is given by:

$$\theta_{\rm res} \propto \frac{\lambda_{\rm obs}}{D} \text{ radians}, \tag{2.1}$$

where $\lambda_{\rm obs}$ is the observing wavelength and the D the telescope diameter.

In contrast with optical telescopes, observations at radio wavelengths require significantly larger radio telescopes to achieve comparable angular resolutions. Very large radio antennas have been constructed historically in an attempt to obtain better resolutions. However very large antennas introduce financial, engineering and functional challenges such as difficulties in tracking the objects of interest as they move across the sky, and gravitational deformation, the deterioration of the integrity of the collecting surface under the stress/strain of gravitational effects on the instrument. Such challenges can be mitigated by making use of interferometry, which employs aperture synthesis to combine the signals from multiple radio antennas into one telescope output.

Interferometry involves the combination of signals from multiple component antennas to simulate one larger antenna, achieving better angular resolution. The physical separation between any two antennas in an interferometric system is termed the baseline, B. The interferometer angular resolution is determined by the maximum baseline $B_{\rm max}$, the separation between the two most distant antennas:

$$\theta_{\rm res} \approx \frac{\lambda_{\rm obs}}{B_{\rm max}} \text{ radians}. \tag{2.2}$$

The simplest radio interferometer is the two element interferometer, the schematic of which is shown in Figure 2.2. Let us consider a quasi-monochromatic[2] interferometric array composed of two antennas, at positions p and q, respectively. The antennas simultaneously observe an arbitrarily distant point source which is located in the sky along the direction $\hat{s}$ at an angle θ from the vector separating them. Antenna q detects the signal from the source before antenna p resulting in a time difference which is dependent on the antenna separation vector $\mathbf{b}$ and the source position in the sky $\hat{s}$, known as the geometrical time delay, $\tau_{\rm g} = \mathbf{b} \cdot \hat{s}/c$ (Figure 2.2).

Accounting for the geometrical time delay, the signal induces in each antenna a voltage $V_{\rm p}$, $V_{\rm q}$ (see Figure 2.2; Condon and Ransom, 2016):

$$V_{\rm p}(t) = V\cos\left[\omega(t-\tau_{\rm g})\right], \tag{2.3}$$

$$V_{\rm q}(t) = V\cos\left(\omega t\right). \tag{2.4}$$

The voltages pass through an amplifier[3] and a correlator which multiplies and time-averages them, resulting in a correlator response $R_{\rm pq}$ (Thompson, 1999; Condon and Ransom, 2016):

$$R_{\rm pq} = \langle V_{\rm p} V_{\rm q} \rangle \simeq \frac{V^2}{2}\cos\left(\omega\tau_{\rm g}\right), \tag{2.5}$$

where $\langle\ \ \rangle$ represents time-averaging. The response function R has an amplitude proportional to the source brightness and varies sinusoidally due to $\tau_{\rm g}$ which, in turn, varies with the Earth's

[2] sensitive to a very narrow frequency band $\Delta\nu$.

[3] which filters the frequency such that they span a small frequency bandwidth ($\nu - \frac{\Delta\nu}{2} \leq \nu \leq \nu + \frac{\Delta\nu}{2}$).

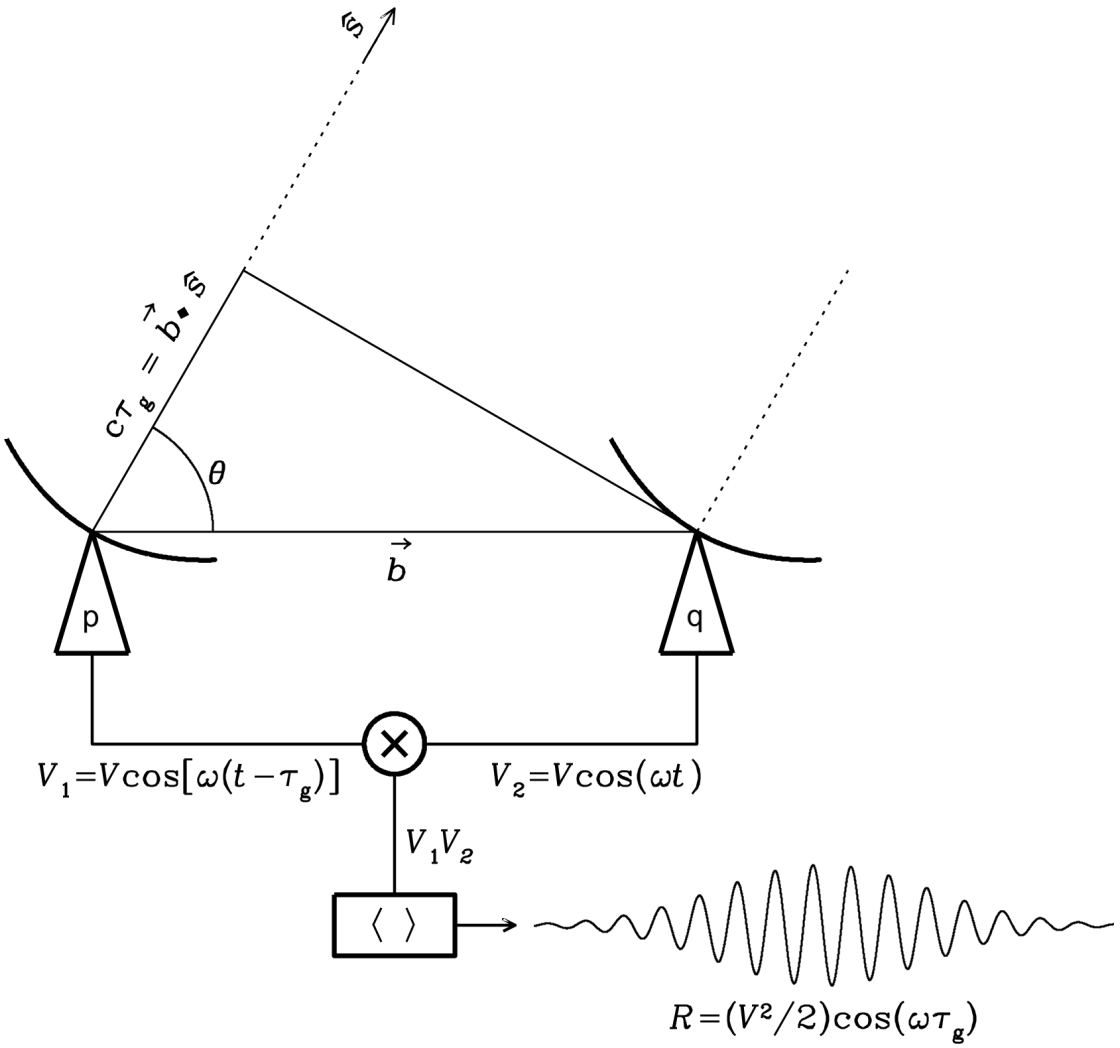

FIGURE 2.2: The two element interferometer schematic, adapted from Condon and Ransom (2016)

rotation (see Figure 2.2). The sinusoid is commonly termed the fringe and is associated with the phase $\phi = \omega\tau_{\rm g} = \frac{2\pi}{\lambda}\mathbf{b}\cdot\hat{s}$.

The correlator response function can be generalised for a number of sources with sky brightness distribution I($\hat{s}$) within a solid angle d Ω (Condon and Ransom, 2016):

$$R_{\rm pq} = \int I(\hat{s})\cos(\omega\tau_{\rm g})\ {\rm d}\Omega = \int I(\hat{s})\cos\left(2\pi\frac{\mathbf{b}\cdot\hat{s}}{\lambda}\right){\rm d}\Omega. \tag{2.6}$$

The response function in equation 2.6 is the output ($R_{\rm c}$) of a cosine correlator which only measures the even component of the sky brightness function; a sine correlator sensitive to the odd component of $I(\hat{s})$ can be designed by introducing a $\frac{\pi}{2}$ phase delay in the cosine correlator. Combining the sine and cosine correlator results in a complex correlator, which measures a complex visibility $V = R_{\rm c} - \imath R_{\rm s}$.

Using Euler's formula, the complex visibility measured by the interferometer is related to the sky brightness distribution function by (Condon and Ransom, 2016):

$$V_{\rm pq} = \int_{\Omega} I(\hat{s}) e^{-2\pi\imath \frac{\mathbf{b}\cdot\hat{s}}{\lambda}} \mathrm{d}\Omega. \tag{2.7}$$

The measured visibility function is therefore related to the sky brightness distribution through a two dimensional Fourier transform (the Van Cittert-Zernike theorem, Zernike, 1938; Born and Wolf, 1980; Thompson et al., 2004):

$$V_{\rm pq}(u,v) = \int_{-\infty}^{\infty}\int_{-\infty}^{\infty} I(l,m)\, e^{-2\pi\imath(ul+vm)} \mathrm{d}l\, \mathrm{d}m = \mathcal{F}\{I(l,m)\}, \tag{2.8}$$

where u, v and l, m represent two dimensional coordinates in the visibility and image space, respectively and $\mathcal{F}\{\ \}$ is the Fourier transform operation.

The sky brightness distribution function can be recovered by inversion of equation 2.8:

$$I(l,m) = \int_{-\infty}^{\infty}\int_{-\infty}^{\infty} V(u,v)\, e^{2\pi\imath(ul+vm)} \mathrm{d}u\, \mathrm{d}v. \tag{2.9}$$

As one baseline pair measures a single point in uv space at a given time, using different baselines, along with the Earth rotation, improves the uv coverage, resulting in a better sampling of the sky brightness distribution. Interferometers are thus typically composed of multiple elements.

2.1 Calibration

Any celestial signal induces a voltage in the receptor that can be described by a vector $\mathbf{e}$ whose basis are the two linear polarizations (Smirnov, 2011):

$$\mathbf{e} = \begin{pmatrix} e_x \\ e_y \end{pmatrix}. \tag{2.10}$$

Before the signal is correlated amongst the various baseline pairs and written to disk, it is distorted by propagation effects due to the atmosphere and the receiver electronics. These distortions are assumed to be linear in nature and described by a 2×2 complex (Jones) matrix $\mathbf{J}$. The resulting distorted signal $\mathbf{e}\,'$ is therefore (Smirnov, 2011):

$$\mathbf{e}\,' = \mathbf{J}\mathbf{e}. \tag{2.11}$$

The visibility between an antenna p and q (equation 2.5) can be written in terms of the voltage vectors induced at each antenna (e.g., Smirnov, 2011):

$$\mathbf{V}_{pq} = \langle \mathbf{v}_p \mathbf{v}_q^H \rangle = \mathbf{J}_p \langle \mathbf{e}\mathbf{e}^H \rangle \mathbf{J}_q^H, \tag{2.12}$$

where H is the Hermitian operator. The averaged voltages can be described using Stokes parameters, which are used to describe the polarization state of electromagnetic radiation (Stokes,

1851; Born and Wolf, 1980; Thompson et al., 2004):

$$\langle \mathbf{e}\mathbf{e}^H \rangle = \begin{pmatrix} \langle e_x e_x^* \rangle & \langle e_x e_y^* \rangle \\ \langle e_y e_x^* \rangle & \langle e_y e_y^* \rangle \end{pmatrix} = \frac{1}{2} \begin{pmatrix} I+Q & U+\imath V \\ U-\imath V & I-Q \end{pmatrix} = \mathbf{B}, \tag{2.13}$$

where the brightness matrix $\mathbf{B}$ describes the source polarized intensity.

Different physical corruptions along the signal chain can be described by different Jones matrices, resulting in a multiplicative chain of Jones matrices. The most common Jones matrices include a frequency dependent complex bandpass $\mathbf{B}(\nu)$ and a time dependent, frequency independent complex gain $\mathbf{G}(t)$.

The gain amplitude component largely results from slow variations of the electronic response while phase variations are mainly due to the atmosphere (Cornwell and Fomalont, 1989) which fluctuates on time scales of seconds to minutes (Thompson et al., 2004).

The process of estimating the Jones matrices and correcting the observed visibilities is known as calibration. It requires the observation of a source whose intrinsic brightness matrix $\mathbf{B}$ is known, i.e. for which model visibilities $\mathbf{V}^m$ can be generated. In this case the antenna gains can be derived as a solution to the system of equations:

$$\mathbf{V}_{pq} = \mathbf{J}_p \mathbf{V}^m \mathbf{J}_q^H. \tag{2.14}$$

Solutions can be found as the system of equations is overdetermined, i.e. it has N unknowns and $\frac{N(N-1)}{2}$ measurements (Pearson and Readhead, 1984; Marr et al., 2016).

The calibration strategy generally involves the observation of a bright, well known unresolved source in order to determine the instrument bandpass and set the absolute flux density scale. Then the target observation is often interspersed by observation of a secondary calibrator, a source which is relatively nearby the target field. The secondary calibrator is used to correct for phase variations induced by atmospheric fluctuations.

2.2 Imaging and self calibration

After calibration, visibilities are Fourier transformed into an image (equation 2.9). However, the visibility function is only sampled at specific u, v coordinates set by the baseline distribution. The observed visibilities are a product of the true visibilities and a sampling function S:

$$V^s(u,v) = V(u,v)\, S(u,v), \tag{2.15}$$

where V^s are the sampled visibilities. The Fourier transform of the sampling function is referred to as the synthesised beam or the point spread function (PSF) and it represents the response of the interferometer to a point source.

Fourier transforming the sampled visibilities results in the sky intensity distribution function $I(l, m)$ convolved with the PSF, known as the dirty image $I^{\mathrm{D}}(l, m)$:

$$I^{\mathrm{D}}(l, m) = I(l, m) \circledast \mathrm{PSF}(l, m), \tag{2.16}$$

requiring a deconvolution from the PSF in order to reconstruct the sky brightness distribution.

The `CLEAN` algorithm (Högbom, 1974) is the most common deconvolution procedure. Its main assumption is that the sky brightness can be represented by a superposition of point sources. At the beginning, an empty copy of the dirty image is created and called the model image.Then the `CLEAN` algorithm finds the peak of the dirty image and subtracts a scaled version of the PSF centred on the corresponding pixel. The fraction of the source flux density subtracted at each step is determined by the loop gain $0 \leq \gamma \leq 1$, a scaling factor usually set to $0.1 \leq \gamma \leq 0.5$ (Thompson et al., 2004). The subtracted intensity is stored in the model image as a `CLEAN` component at the location where it was subtracted in the dirty image. After the subtraction, the dirty image becomes a residual image.

The flux density peak of the residual image decreases at each iteration, the algorithm stops when either the peak of the residual image is below a user-defined threshold or the number of iterations reach a user-defined threshold. After the deconvolution stops, a restored image is formed by summing the residual image to the model image convolved with the `CLEAN` Beam [4] (Foster, 2017)[5].

Multiple variants of Hogbom's `CLEAN` algorithm have been developed over the years. The most commonly used include the Clark (1980) and Schwab (1984) `CLEAN` variants. The Clark `CLEAN` algorithm speeds up the computation by dividing the deconvolution into 'minor' and 'major' cycles. In the minor cycle, the algorithm locates pixels brighter than a user-defined subset of the PSF central regions and builds a partial sky model. In the major cycle, the partial sky model and the PSF are Fourier transformed, multiplied together and the product is Fourier transformed and subtracted from the current residual image. This procedure allows the deconvolution to cover a larger subset of the image in each major cycle iteration.

The Cotton-Schwab variant retains the minor and major cycles of the Clark algorithm, but performs the subtraction of the sky model from the ungridded visibilities, leading to a more accurate result.

Image deconvolution is often limited by calibration inaccuracies, mostly due to time variable antenna gains that are not corrected by the calibration procedure described so far. Improvement in the image quality can be achieved via self calibration, a procedure that uses a model derived from the target field itself to improve the calibration (e.g Pearson and Readhead, 1984; Cornwell and Fomalont, 1989).

Self calibration begins with a sky model derived from the `CLEAN` components (Readhead and Wilkinson, 1978; Pearson and Readhead, 1984; Cornwell and Fomalont, 1989). The gains are

[4] a two dimensional Gaussian fitted to the main lobe of the PSF

[5] National Astrophysics and Space Science Program Fundamentals of Radio Interferometry for Aperture Synthesis course

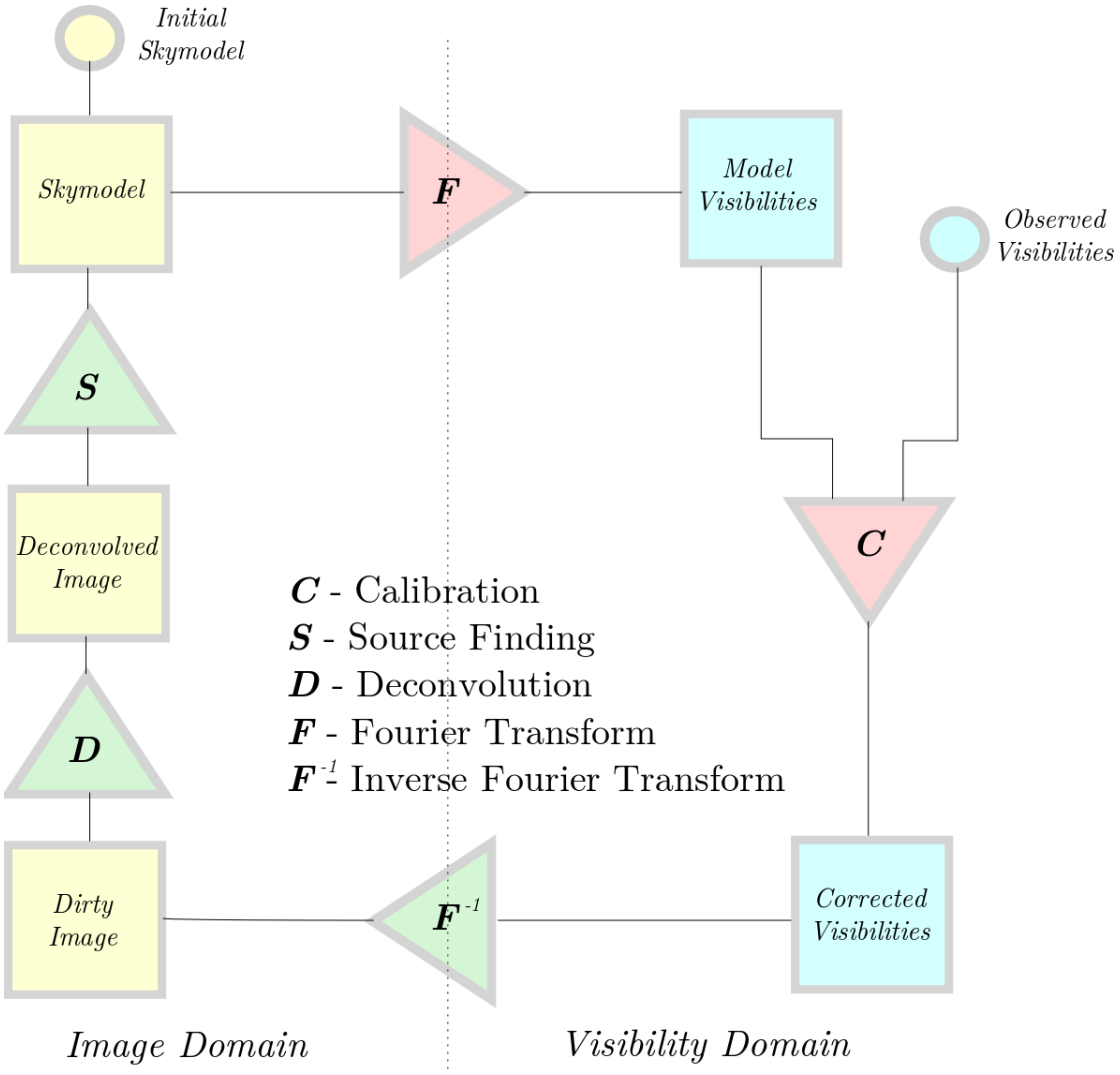

FIGURE 2.3: Flow chart of the self calibration process. Yellow and green backgrounds represent images and operations that occur in the image domain, respectively. Cyan and pink backgrounds represent visibilities and operations occurring in the visibility domain, respectively. (Kenyon, 2017).

calculated as described in Section 2.1 and applied to further correct the visibilities. These self-calibrated visibilities are then imaged and deconvolved as described above. This process is iteratively repeated until self calibration no longer improves the image.

Chapter 3

Observations and data reduction

TABLE 3.1: Directions of the two pointings covering the Perseus cluster.

Source ID	**Right Ascension**	**Declination**
3C84-EAST	03h 22m 00s	+41d 27m 00s
3C84-NORTH	03h 18m 00s	+42d 05m 00s

Observations were carried out using the Westerbork Synthesis Radio Telescope (WSRT, Figure 3.1). The WSRT has 14 steerable antennas placed along an East - West track. Ten antennas, named RT0 − 9 (Figure 3.2) are fixed on the track, placed 144 m apart, while the remaining four are movable, with antenna A and B on one rail track (track AB) and antenna C and D on another (track CD). Track AB runs from a distance of 36 m from RT9 and has a length of 300 m. Track CD runs from a distance of 9 × 144 m east of track AB and is 180 m long. Antennas A, B and C, D can be moved to observe from any position along their respective rail tracks. Therefore, the array can achieve baseline lengths in the range 36 m $\leq |\mathbf{b}| \leq$ 2.7 km (Morganti, 2004). Each antenna station is equipped with a dish of diameter 25 m on an equatorial mount, which allows the antennas to compensate for the Earth's rotation during an observation (see Curry and Knightington, 2014; Marr et al., 2016).

In this thesis we used archival data that were taken in the so-called maxi-short configuration, which is typically used for a single 12 hour observation as it offers a trade off between a good *uv*-coverage (see, for example, Figure 3.3) and sensitivity to extended sources. In this configuration RTA is moved closest to the fixed antenna RT9 (RT9 - RTA = 36 m), RTB is 54 m away from RTA and RTC - RTD = 72 m (Morganti, 2004; Pizzo, 2010).

The data we analysed in this thesis are composed of two different pointings covering most of the Perseus cluster area (see Table 3.1). Each pointing was observed for $\sim$ 12 h (Table 3.2).

The WSRT is generally a very stable instrument at 1.4 GHz, therefore observations of calibration sources were carried out only at the beginning (3C 48) and at the end (3C 147) of each 12 h run for $\sim$ 15 minutes. Observations were carried out over 8 spectral windows, each 20 MHz wide

[1]credit: old.astron.nl/sites/astron.nl/files/cms/west0l.jpg
[2]credit: old.astron.nl/sites/astron.nl/files/cms/config.jpg

FIGURE 3.1: Aerial photograph of the WSRT antennas[1](Astron, 2018a).

FIGURE 3.2: WSRT antenna configuration (Astron, 2018b)[2]

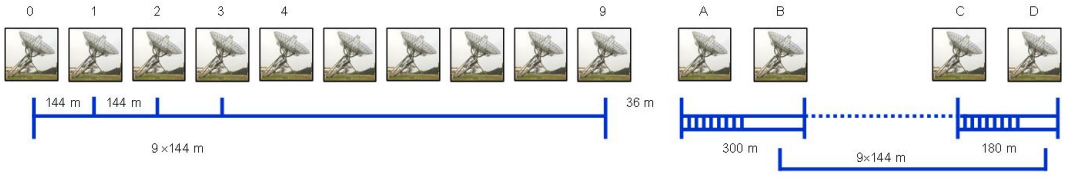

and divided into 64 channels. The spectral windows are centred at 1311, 1330, 1350, 1370, 1392, 1410, 1428 and 1450 MHz, respectively.

The data reduction was carried out using the Common Astronomy Software Applications (`CASA`) package (Mcmullin et al., 2007) The first step was to flag bad data due to Radio Frequency

TABLE 3.2: Observational summary.

Pointing	**Start Time (UTC)**	**End Time**	**Duration (hr)**
3C84-EAST	2007/10/16 19:16:20.0	2007/10/17 07:15:10.0	11.98
3C84-NORTH	2007/10/17 19:08:20.0	2007/10/18 04:37:20.0	11.43
3C84-NORTH	2007/10/21 18:52:50.0	2007/10/22 05:55:50.0	11.05
3C84-EAST	2007/10/22 18:52:40.0	2007/10/23 05:55:50.0	11.05

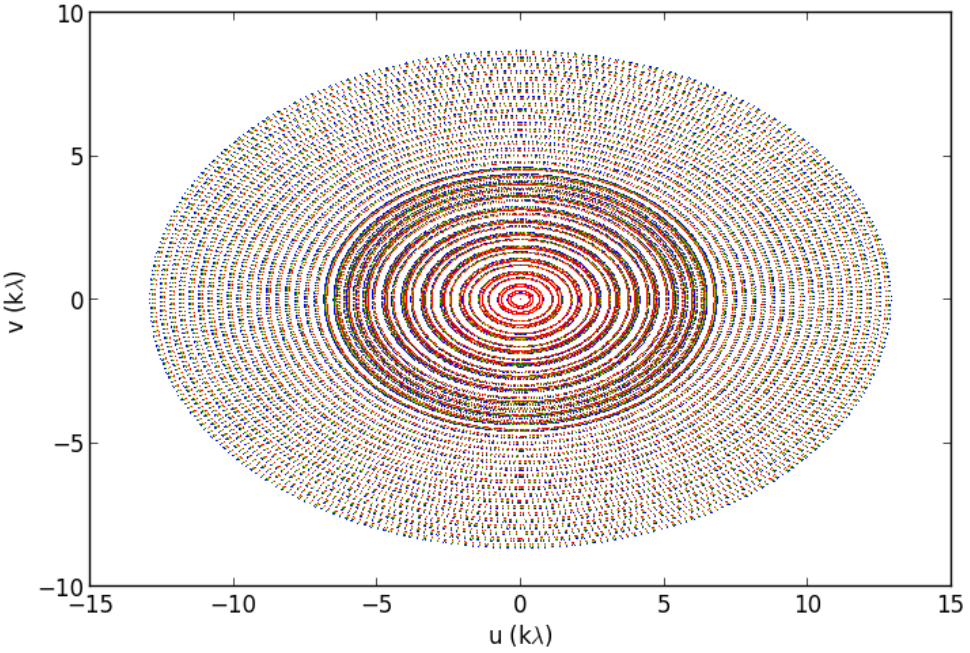

FIGURE 3.3: WSRT *uv*-coverage for the north pointing observation for the spectral window centred at 1392 MHz.

Interference (RFI). Data were initially inspected and antenna 6 was found to be bad and flagged. The first and last few channels of each spectral window were flagged for bandpass roll-off. The first and the last minute of each observation were also flagged. We carried out further flagging by using the `CASA tfcrop` auto-flag algorithm. This algorithm calculates a linear fit along the time axis in each frequency channel and the standard deviation σ from the best fit then iteratively flags data points with values beyond 3σ from the best fit. The algorithm also performs a piece-wise polynomial fit on the time-averaged bandpass in order to estimate an RFI-free bandpass. This estimated RFI-free bandpass is then used to detect and flag outliers on the two dimensional time-frequency plane (Martins and Rau, 2016). We also use `AOFLAGGER` (Offringa et al., 2010; Offringa, 2016) to flag bad data using a standard mask developed for WSRT observations. Bandpass calibration was performed on 3C 48 which has a flux density $S_\nu = 16.67$ Jy at $\nu = 1392$ MHz (Perley and Butler, 2013).

Figure 3.4 shows an example of the calibrator bandpass amplitude solutions, which are derived

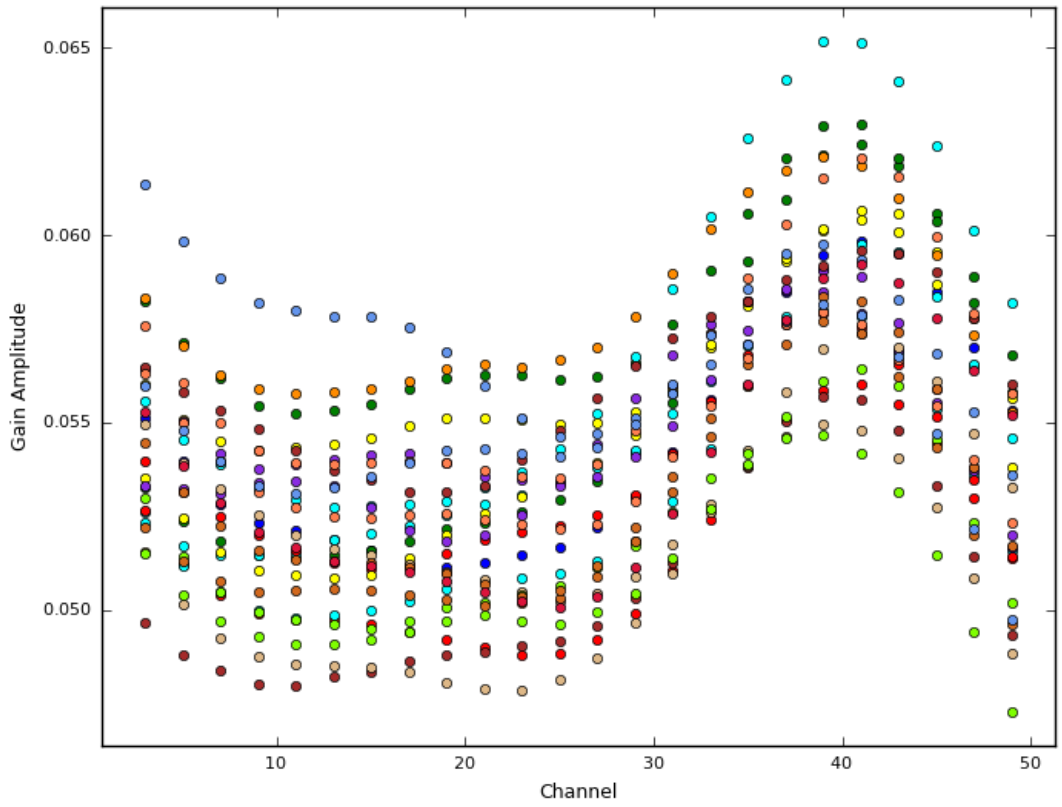

FIGURE 3.4: Amplitude gain variations for 3C 48 at the spectral window centred at a frequency of 1392 MHz

independently for each of the eight spectral windows. Figure 3.5 shows the visibility spectra of 3C 48 after calibration, in agreement with the model.

In order to assess the bandpass stability throughout the duration of the observation, we apply the bandpass solutions to 3C 147, which is observed at the end of each observation run. We found that its visibility spectrum is in agreement with the literature one (Perley and Butler, 2013) within $\sim 2\%$. This procedure was used to derive the bandpass for both pointings.

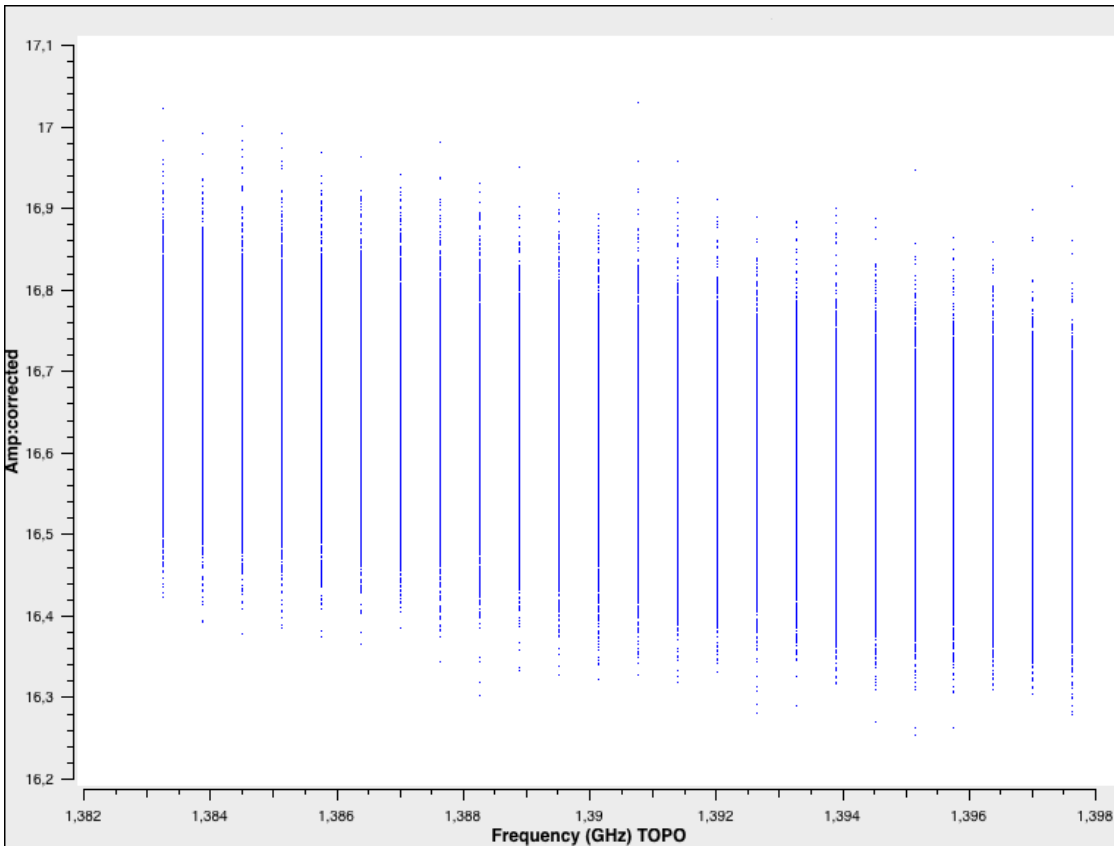

FIGURE 3.5: Calibrated visibility spectra of 3C 48 for the spectral window centred at ν = 1392 MHz.

3.1 Imaging and self-calibration of the East pointing

We begin with the description of the reduction of the East pointing. The target field was flagged following the same procedure used for 3C 48. We then applied the complex bandpass calibration and generated a dirty image using the CASA task `clean`. Visibilities were gridded using multi-frequency synthesis (Sault and Conway, 1999; Sault and Oosterloo, 2007), to combine the eight spectral windows from the two observing nights together and improve the *uv* coverage. We used uniform weights in order to suppress sidelobes across the 1°.1 image size, corresponding to approximately twice the full width at half maximum of the WSRT primary beam.

Clean boxes were interactively drawn around regions of bright sky emission and the search for clean components was restricted to these regions in all deconvolution rounds. The dirty image was deconvolved using the Cotton-Schwab algorithm (Schwab, 1984) down to a 6 mJy threshold, when the model image included the first negative component. This sky model, shown in Figure 3.6 was used for the first round of self-calibration.

Figure 3.7 shows the restored image before self-calibration, where sidelobes from 3C 84 run through the whole image. Residual sidelobes are due to calibration errors as they are not subtracted by deconvolution that, conversely, subtracts 3C 84 fairly well (Figure 3.8). We corrected these errors with self-calibration. We started off with five rounds of self-calibration by solving for the complex bandpass with a 300 second interval, which is possible as 3C 84 is very

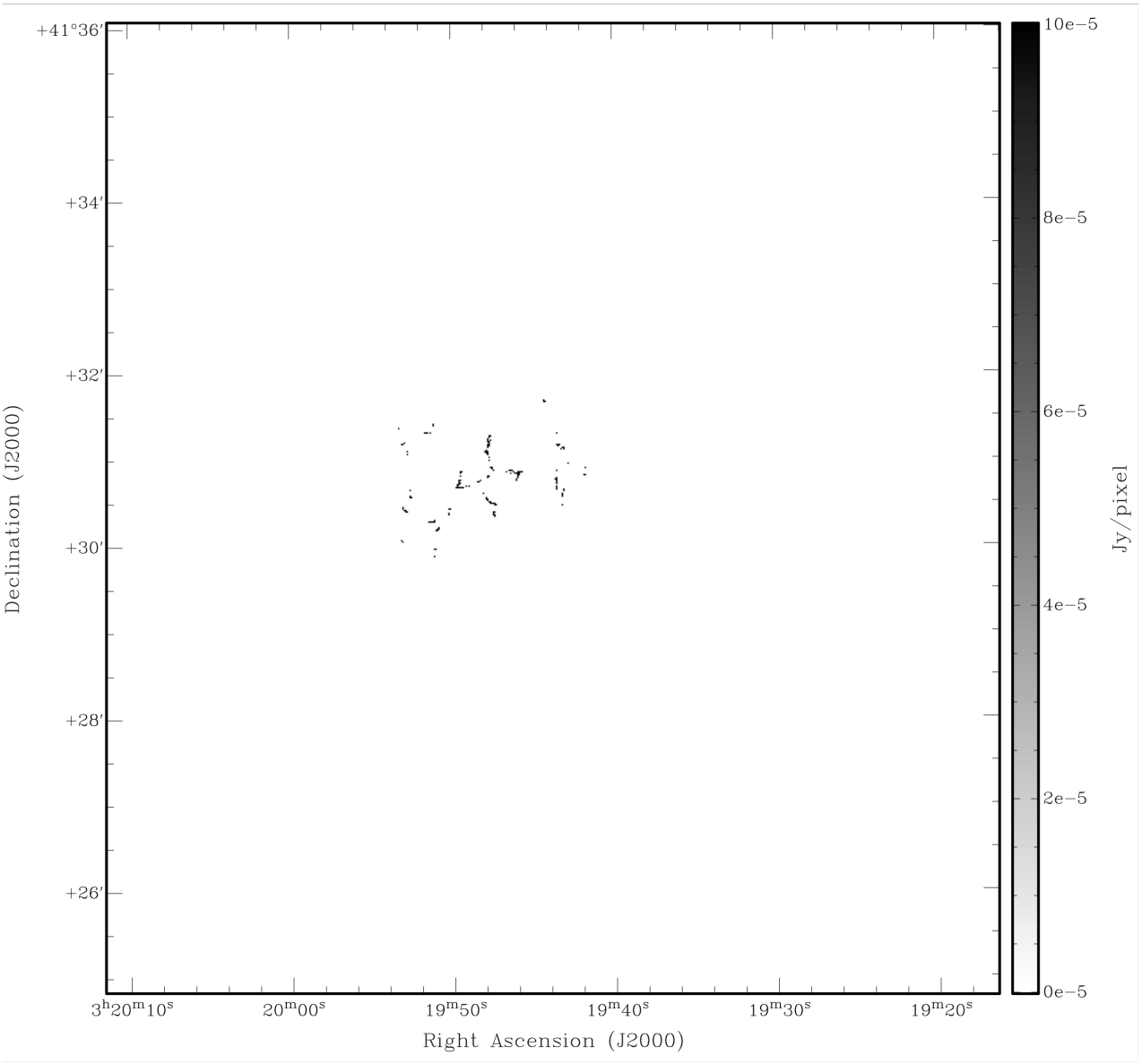

FIGURE 3.6: 3C 84 model image used for the first self-calibration loop.

bright (20.54 Jy). After the second round we improved the initial sky model by including sources across the whole field of view by using the Python Blob Detector and Source Finder (PyBDSF, Mohan and Rafferty, 2015). PyBDSF is a source-finder that fits two dimensional Gaussian models to image sources. We extracted sources down to a 2.6 mJy threshold and added to the model of Figure 3.6 to improve the calibration solutions. Examples of self-calibration solutions are shown in Figure 3.9.

After each round of self-calibration, data were further flagged based on the statistics of the residual visibilities. The sky model was Fourier transformed to generate model visibilities which

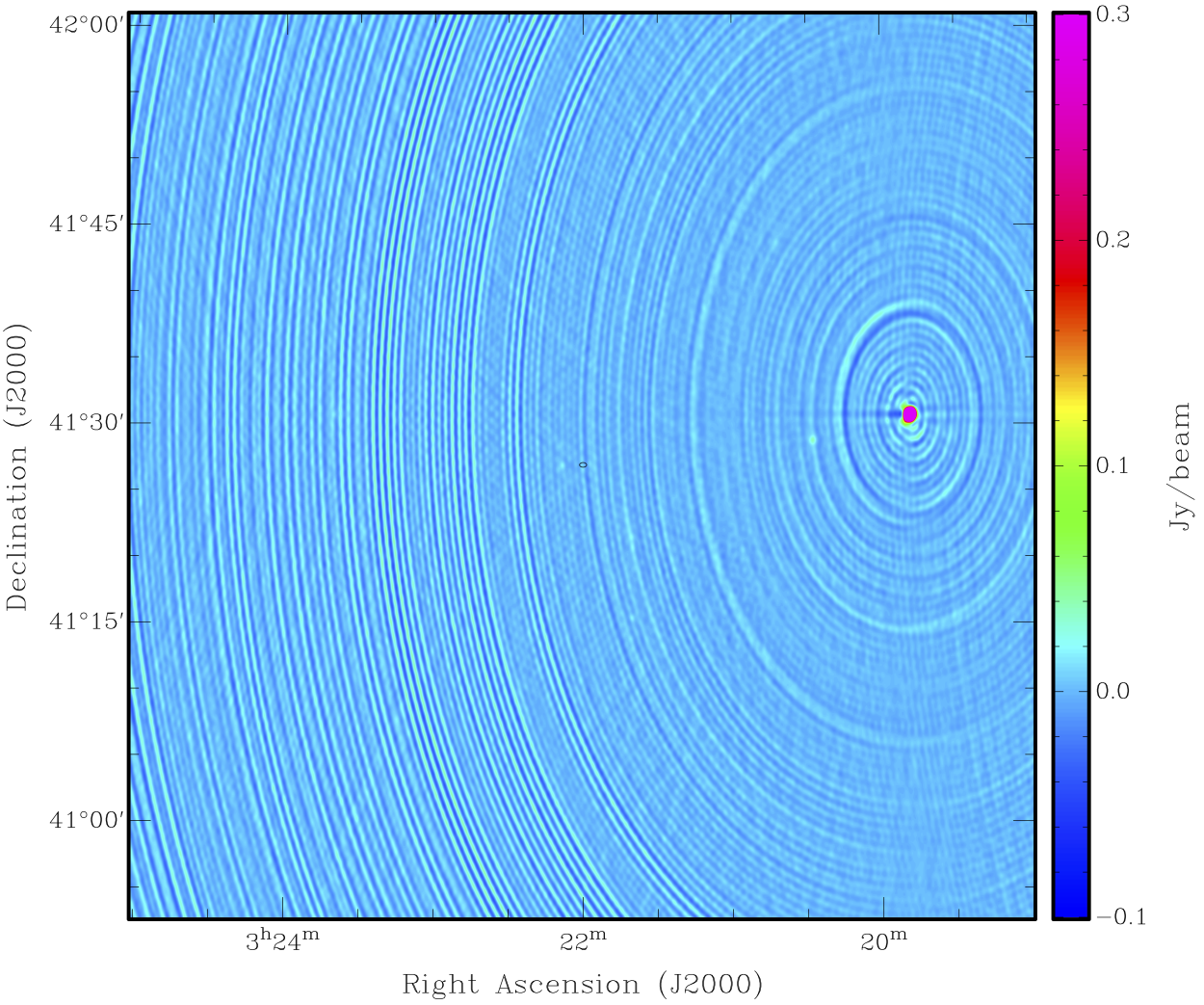

FIGURE 3.7: WSRT East pointing image at 1380 MHz, before self-calibration. The image has a resolution of $32'' \times 21''$ and a ~ 12 mJy beam^{-1} noise level, dominated by the sidelobes from 3C 84, originating from calibration errors.

were subtracted from the calibrated visibilities to form residual visibilities. The residual visibilities were then binned into histograms for each channel, and are expected to follow a Gaussian distribution (in case of ideal noise); thus outliers were flagged as bad data.

The calibration of the two outermost antennas (RT13 and RT14) remained limited and we eventually decided to discard them from the following processing. We believe that the limitations were due to the incomplete sky model of the cluster centre, where there is strong emission across a wide range of angular scales (3C 84 and the mini halo).

As we iteratively performed the deconvolution, self-calibration and residual flagging of outlier visibilities, the image quality improved and we thus adjusted our clean box to include the weaker field sources and, particularly, the diffuse emission surrounding 3C 84 down to ~ 800 μJy beam^{-1} (Figure 3.10). Ultimately, we performed 11 rounds of self-calibration, and our final image was obtained by deconvolving down to a flux threshold of 800 μJy beam^{-1} (Figure 3.11).

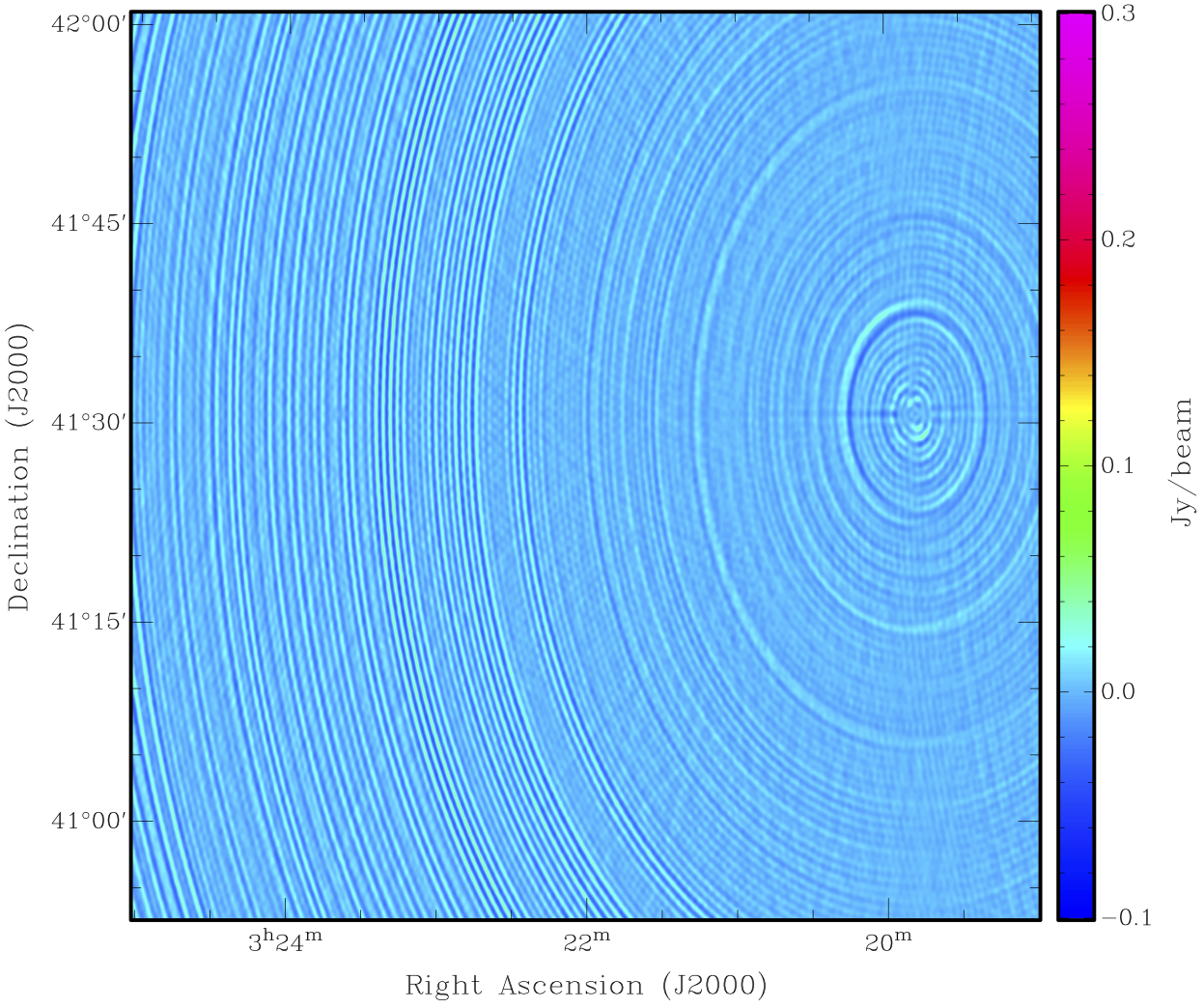

FIGURE 3.8: East pointing residual image at 1380 MHz, before self-calibration. The image has a resolution of $32'' \times 21''$ and a ~ 12 mJy beam^{-1} noise level dominated by contributions from the sidelobes.

Self-calibration significantly improves the image quality, by suppressing the sidelobe level and revealing, on top of 3C 84, the mini halo structure and several compact sources across the whole field of view. The final image is not, however, artefact free as some sidelobe contamination remains present. A commonly used metric to quantify the image quality is its dynamic range (DR), i.e. the ratio between the image peak flux $S_{\rm max}$ and the noise standard deviation σ_I (e.g Noordam and Smirnov, 2010):

$$DR = \frac{S_{\rm max}}{\sigma_I}. \tag{3.1}$$

The noise standard deviation was measured at the edge of the image, in a region with no visible source. The initial restored image has a dynamic range of $DR \sim 340$, whereas self-calibration yielded to a final, noticeable dynamic range $DR \sim 60000$.

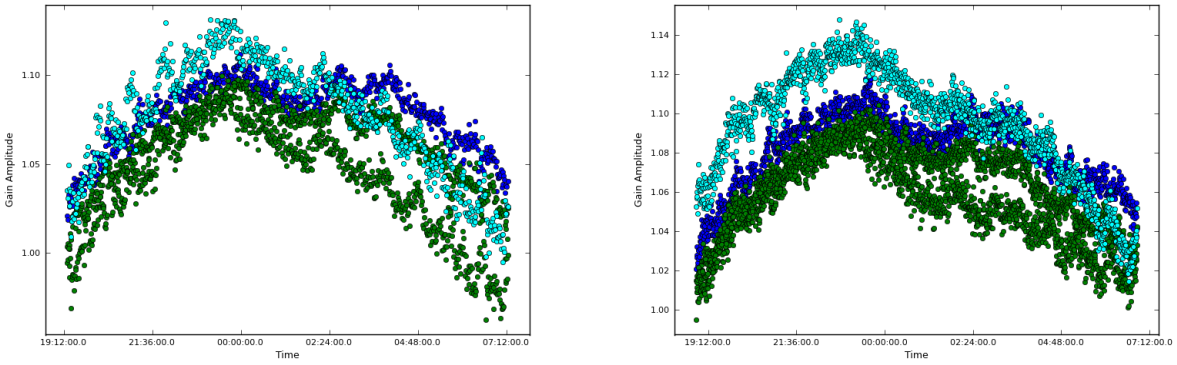

FIGURE 3.9: Examples of self-calibration solutions for the spectral window centred at 1392 MHz from the October 16^{th} (left) and 22^{nd} (right) observation respectively. Each colour is a different channel.

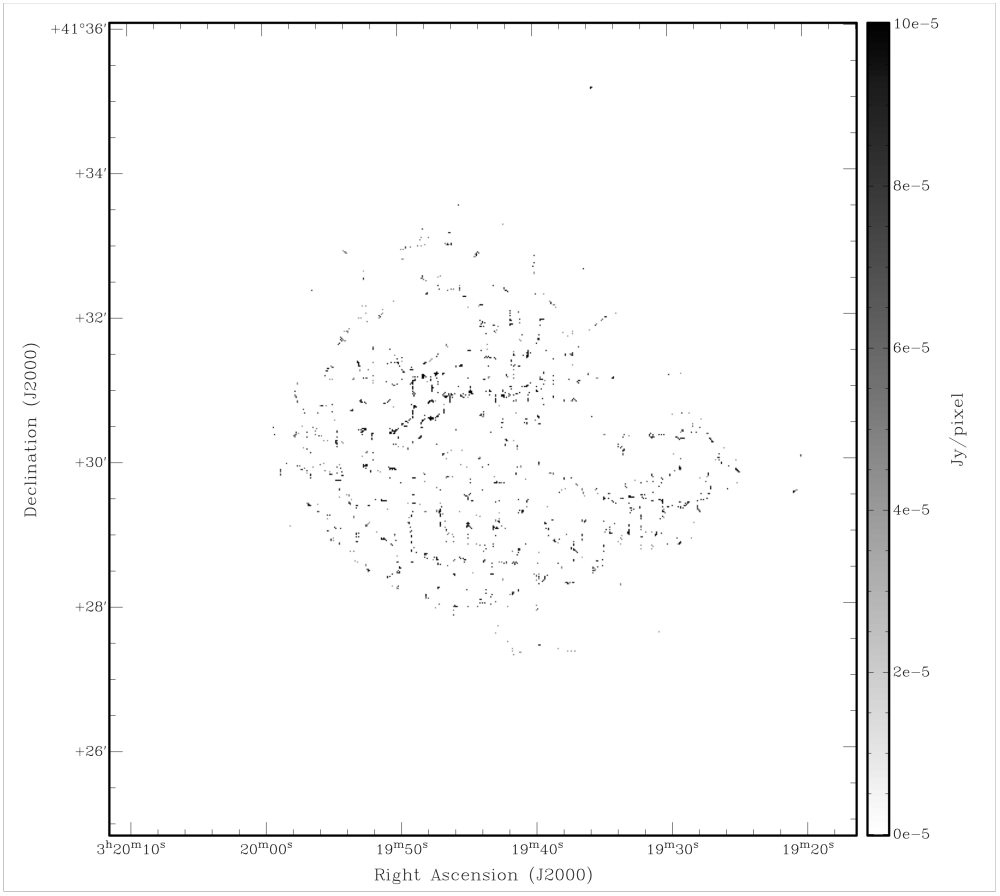

FIGURE 3.10: 3C 84 model image after the final self-calibration round

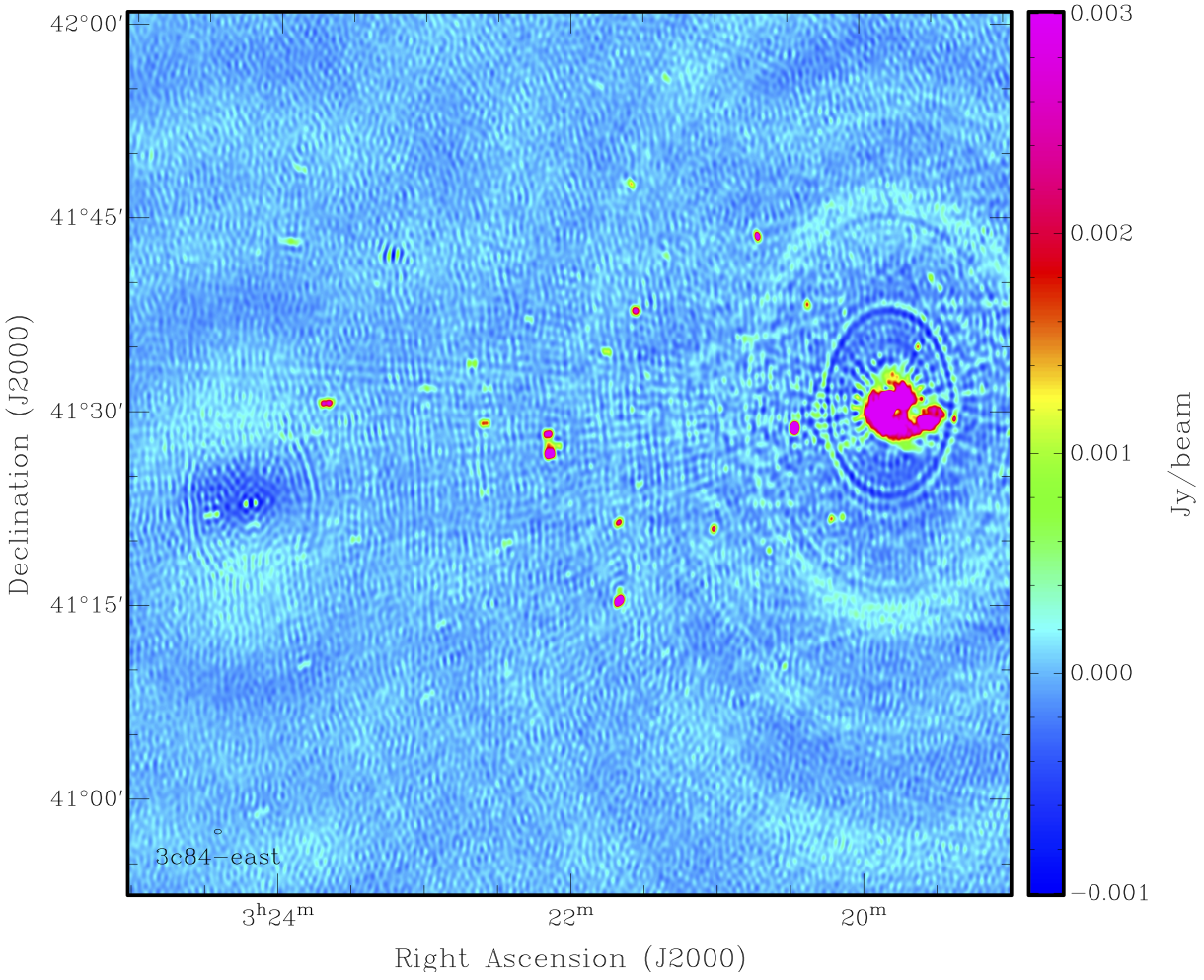

FIGURE 3.11: East pointing image at 1380 MHz after self-calibration. The image has a resolution of $32'' \times 21''$ and a ~ 83 μJy beam^{-1} noise level.

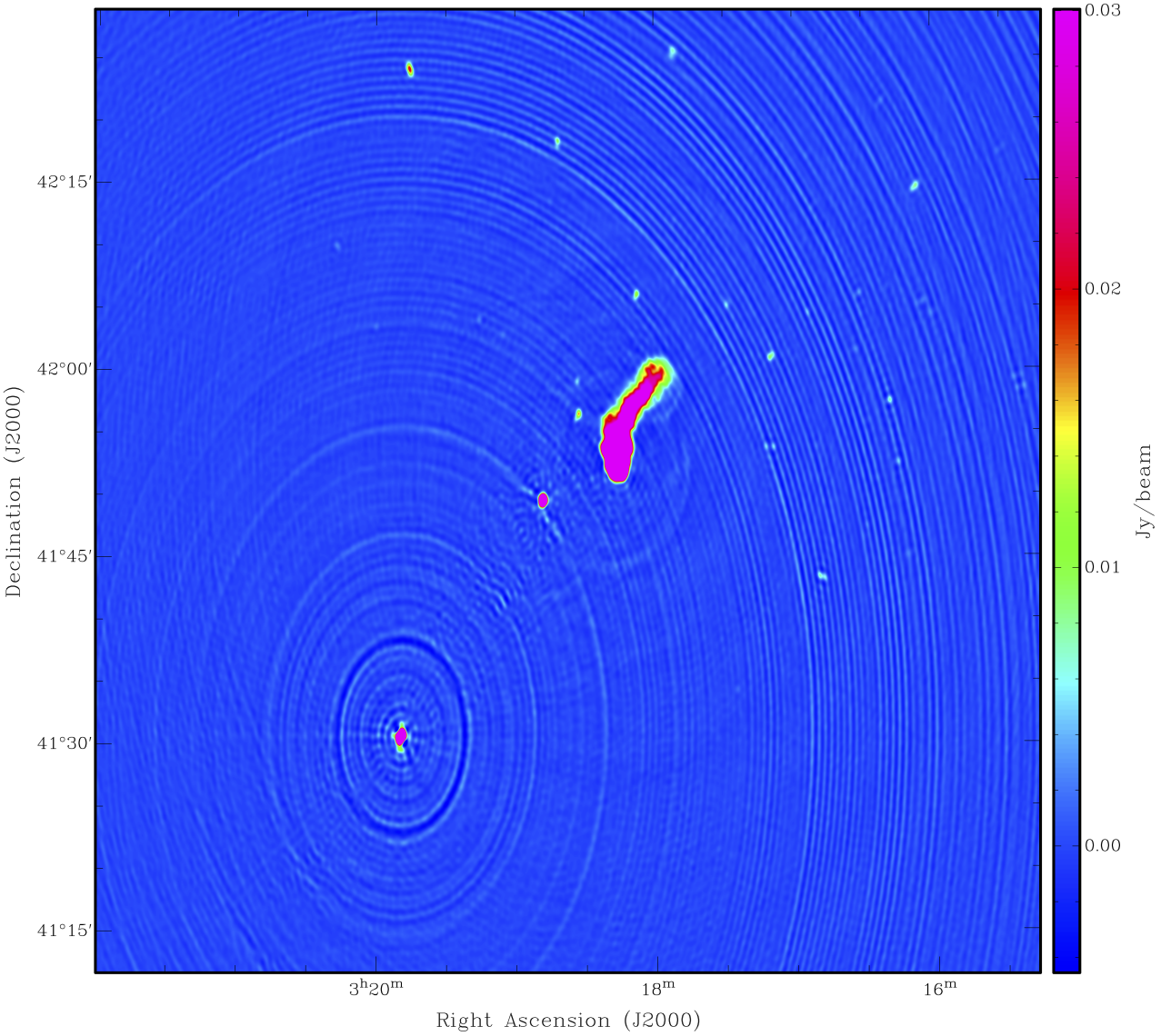

FIGURE 3.12: WSRT North pointing image before self-calibration at a central observing frequency of $\nu = 1380$ MHz, made with the Cotton-Schwab `clean` algorithm.

3.2 Imaging and self-calibration of the North pointing

The initial flagging, calibration and imaging were performed similarly to the procedure described in Section 3.1, resulting in the image shown in Figure 3.12.

This pointing is centred on the bright, extended head tail radio galaxy 3C 83.1 B (Sijbring and de Bruyn, 1998) whose tail extends for more than 1 Mpc (approximately 20′ in our observations). The Cotton-Schwab `clean` has limitations in modelling the complex, extended brightness distribution of 3C 83.1 B, leaving residual emission in the residual image (Figure 3.13). In order to obtain a more accurate model for self-calibration we therefore used the multi-scale `clean` algorithm (Cornwell, 2008), which allows the deconvolution of sky emission correlated on scales larger than the pixel size. The various scales were specified by setting the CASA `multiscale` parameter to `multiscale` $= [0, 10, 20, 26]$. The first scale corresponds to point sources, while

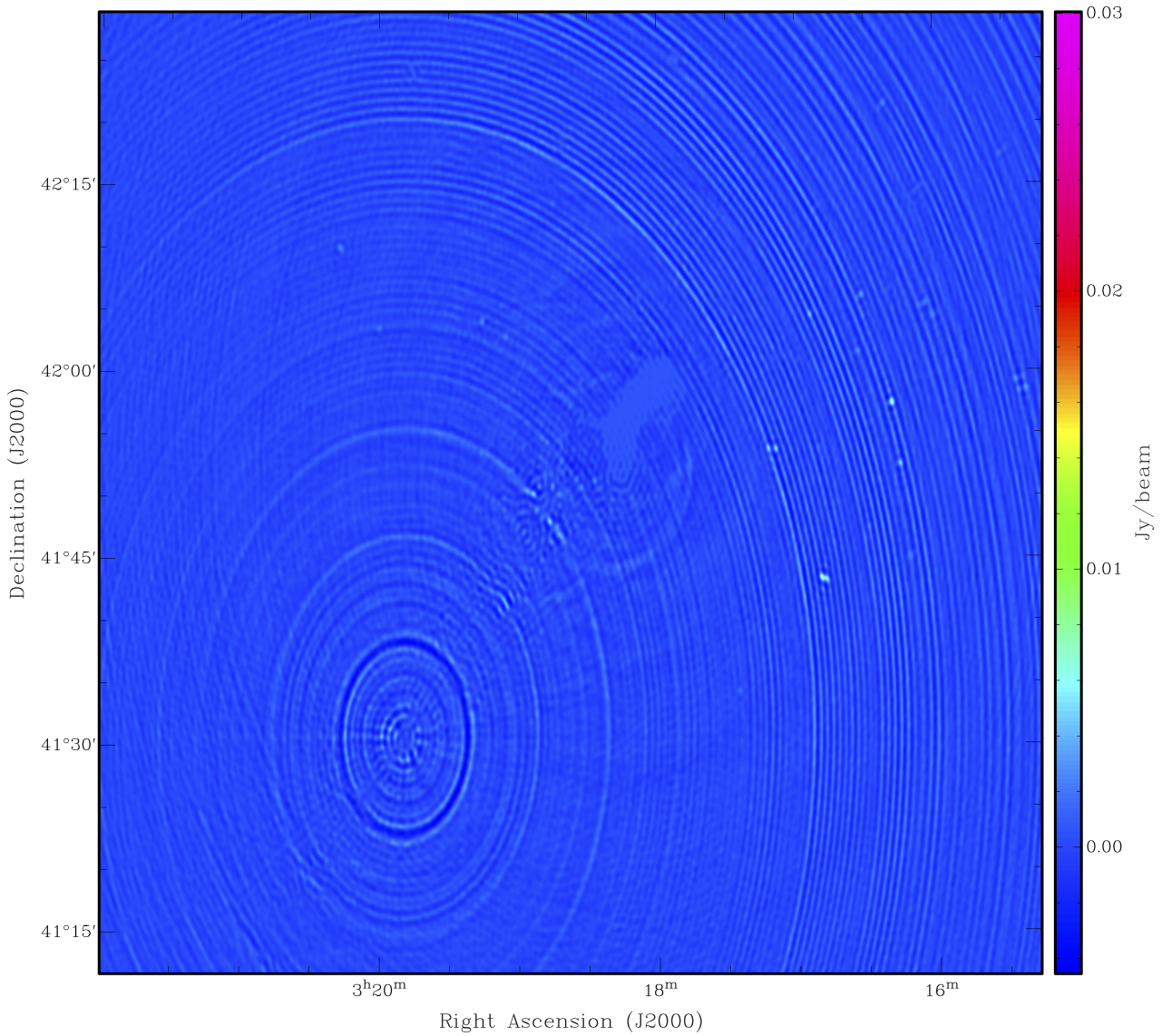

FIGURE 3.13: WSRT North pointing residual image at $\nu = 1380$ MHz, after deconvolution with the Cotton-Schwab `clean` algorithm.

the other scales correspond to source sizes spanning multiple pixels as specified by the user. The multi-scale algorithm generates therefore one model image for each scale and the restored image is the linear combination of the model image convolved with the corresponding Gaussian beams.

The model image resulting from the first multiscale deconvolution round was used to self-calibrate the time-variation of the phases and the amplitude on a 30 second interval. A sky model for the rest of the field was obtained with PyBDSF in a similar way as described in the previous section. Figure 3.14 shows the image after eleven rounds of self-calibration and Figure 3.15 shows the corresponding residual image. We notice that the multi-scale `clean` was able to produce lower residuals associated with 3C 83.1 B, i.e. improve the source model.

Sidelobes due to 3C 84 are present across the image above the noise level. As the source is $\sim 30'$, i.e. significantly attenuated by the primary beam, it likely suffers from calibration errors. We nevertheless estimated the image noise as the standard deviation of the image pixels in a region

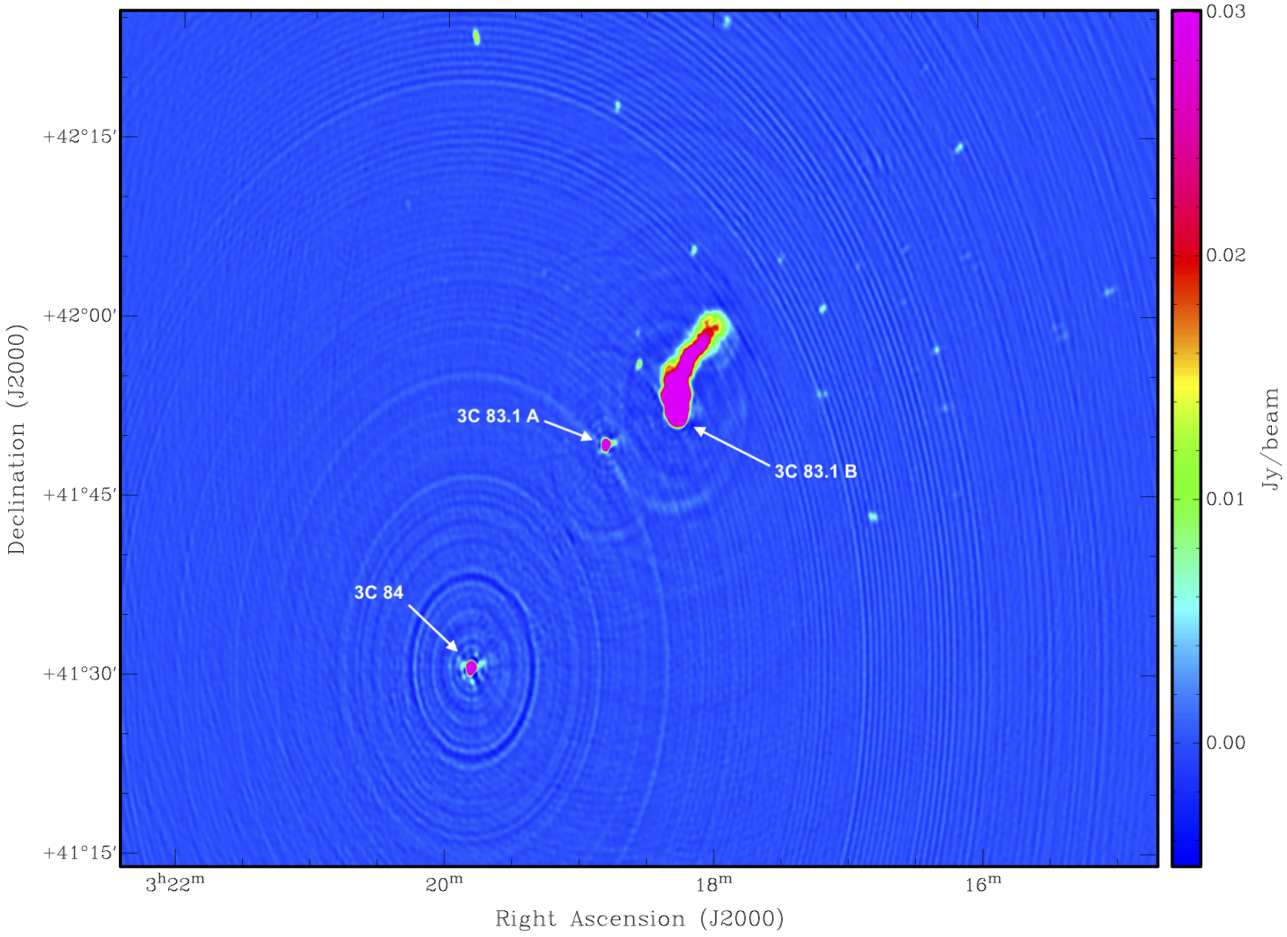

FIGURE 3.14: WSRT North pointing image at $\nu = 1380$ MHz after self-calibration made with the multiscale `clean` algorithm. The angular resolution is 31×21 arcsec^2, and the noise is ~ 240 μJy beam-1. The radio source 3C 83.1 A can be seen roughly $6.6'$ south-east-south of 3C 83.1 B, while 3C 84 is about $30'$ south-south-east of 3C 83.1 B.

away from the pointing direction and with no sky sources, obtaining $\sigma_I = 240$ μJy beam^{-1} and an image dynamic range of ~ 1500.

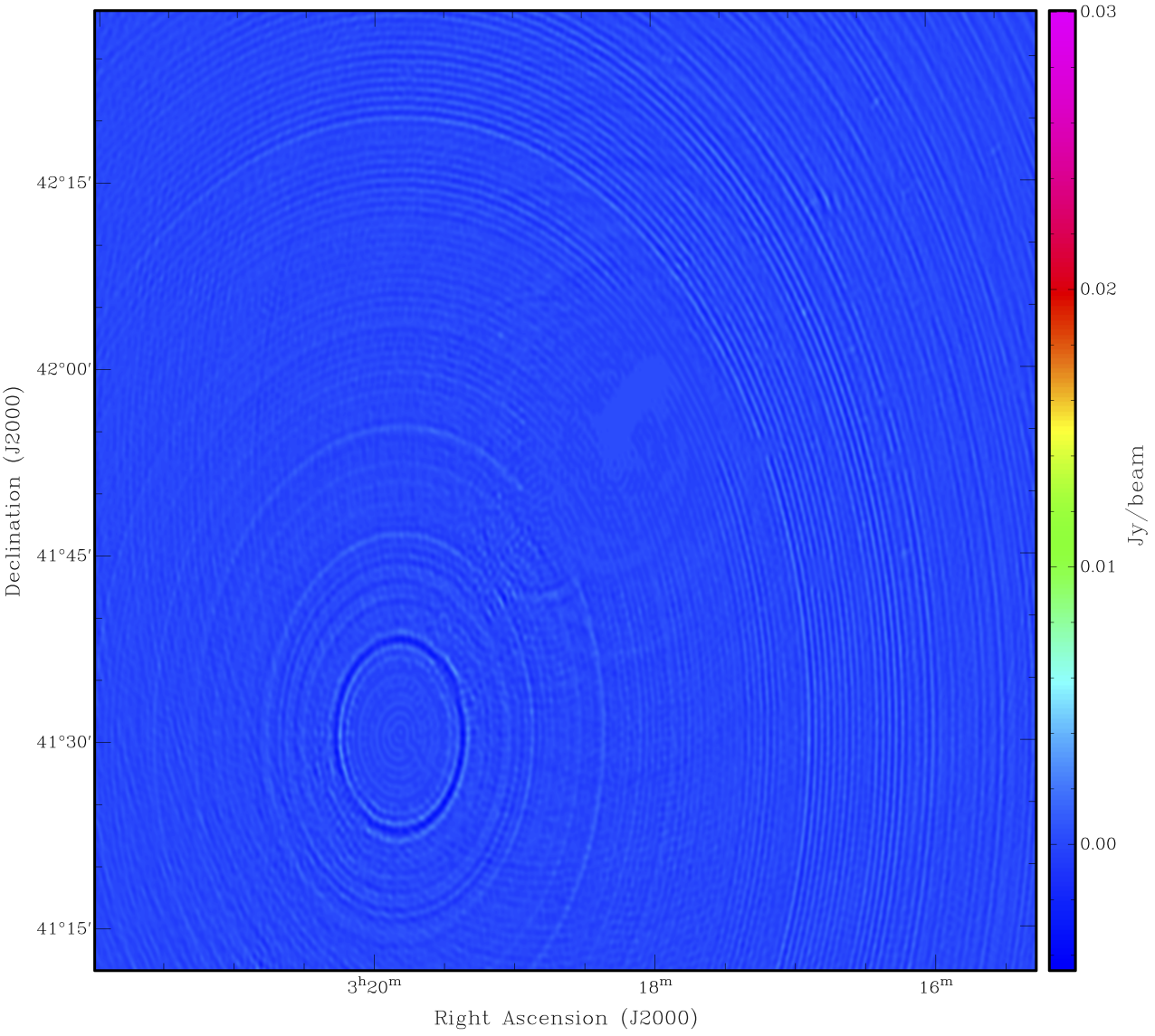

FIGURE 3.15: WSRT North pointing residual image at $\nu = 1380$ MHz, made with the multi-scale `clean` algorithm.

Chapter 4

Results

4.1 EAST Pointing

4.1.1 3C 84

As we discussed in Section 1.5.1, radio observations of 3C 84 have been carried out at an extensive range of frequencies and angular resolutions in the literature. Figure 4.1 compares our results (zoom in of Figure 3.11 centred on 3C 84) with the observations by Pedlar et al. (1990). Our resolution does not allow us to image the jets and knots (Section 1.5.1) which are well contained within 20″ from the image centre[1]. However, we corrected our images by the primary beam in order to measure the absolute flux density of 3C 84. The WSRT primary beam can be well approximated as (e.g., Bernardi et al., 2010):

$$A(\nu, \gamma) = \cos^6(0.065\,\nu\,\gamma), \tag{4.1}$$

where ν is the observing frequency in MHz and γ is the angular distance from the pointing direction in radians (Figure 4.2). 3C 84 is located at the $\sim 25\%$ beam power point. As visible in Figure 4.1, the source is embedded in a diffuse emission region - the mini halo. In order to produce a best estimate of the source flux density without contamination from the diffuse emission we performed a two dimensional Gaussian fit to all the pixels that are included in one synthesized beam ($21'' \times 32''$), centred on the source peak. The fit yielded a flux density of 20.5 ± 0.4 Jy, where the error budget is mostly due to the uncertainty in the bandpass calibration (see Section 3).

Performing the two dimensional Gaussian fit on a region with double the semi-major and semi-minor axis results in a 0.9% increase, while halving the dimensions of the elliptical region, results in a 0.5% decrease in flux density.

3C 84 is known to be a highly variable source, on time-scales of weeks to months at different frequencies (e.g., Dent, 1966; Pauliny-Toth and Kellerman, 1966; Kellermann and Pauliny-Toth,

[1]We assumed $H_0 = 69.6$ km s^{-1} Mpc^{-1} for the Hubble constant, $\Omega_M = 0.286$, $\Omega_\Lambda = 0.714$, leading to $1'' = 359$ pc at the cluster redshift.

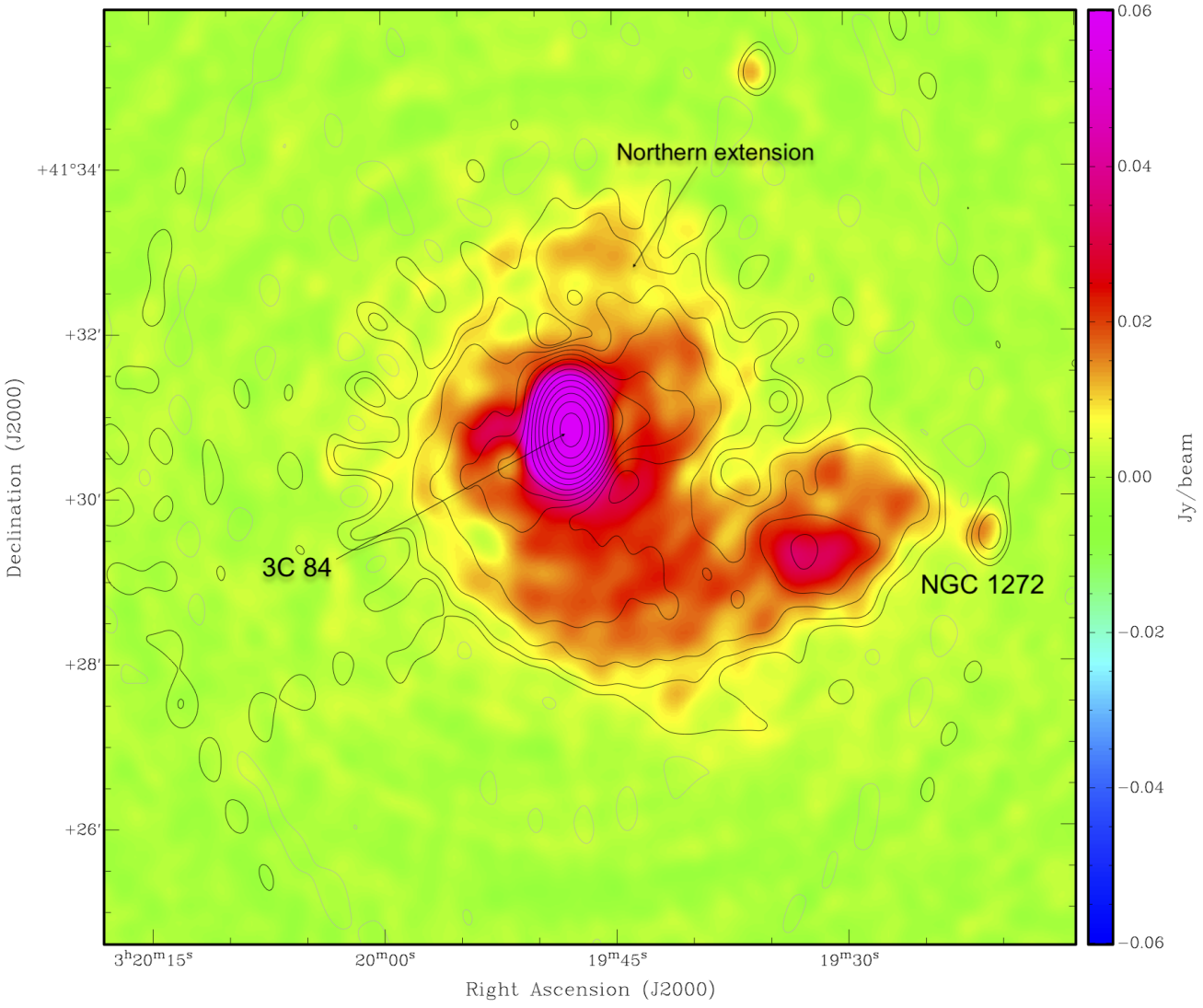

FIGURE 4.1: 3C 84 image at 1380 MHz with a resolution of 21″ (Pedlar et al., 1990) with WSRT contours overlaid. Contours are shown from $\pm 5\sigma$ and incremented by a factor of 2 up to 4.94 Jy beam^{-1}. Negative contours are shown in grey, while positive contours are shown in black. The emission from the mini halo surrounding 3C 84 is clearly visible and with a similar morphology in both observations.

1968; O'Dea et al., 1984). We plotted the source light curve spanning four decades and including our WSRT measurement in Figure 4.3. Our flux density measurement is in substantial agreement with the more recent ones, showing that the flux density has more than doubled over the last forty years, with a steeper increase from the 1990s.

The limited angular resolution of our observations does not allow us to draw any new result on the morphology of 3C 84.

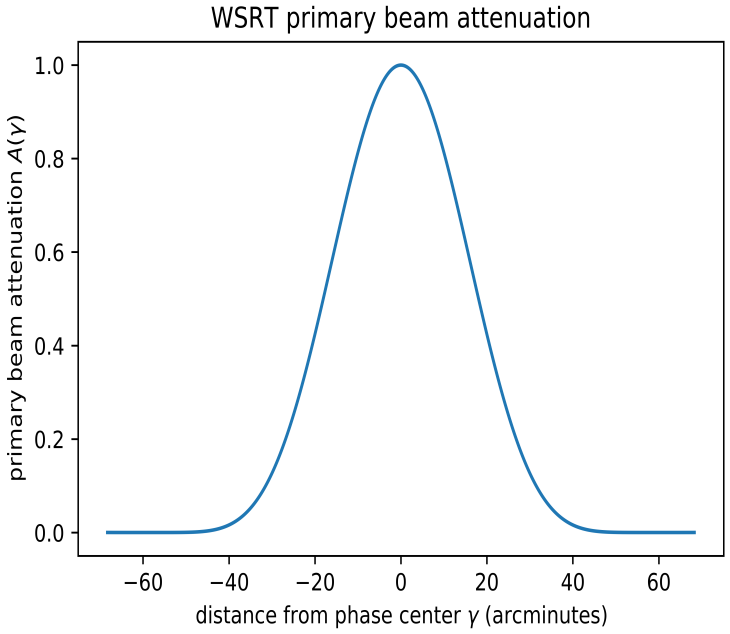

FIGURE 4.2: Profile of the WSRT primary beam at 1.4 GHz, from Equation 4.1

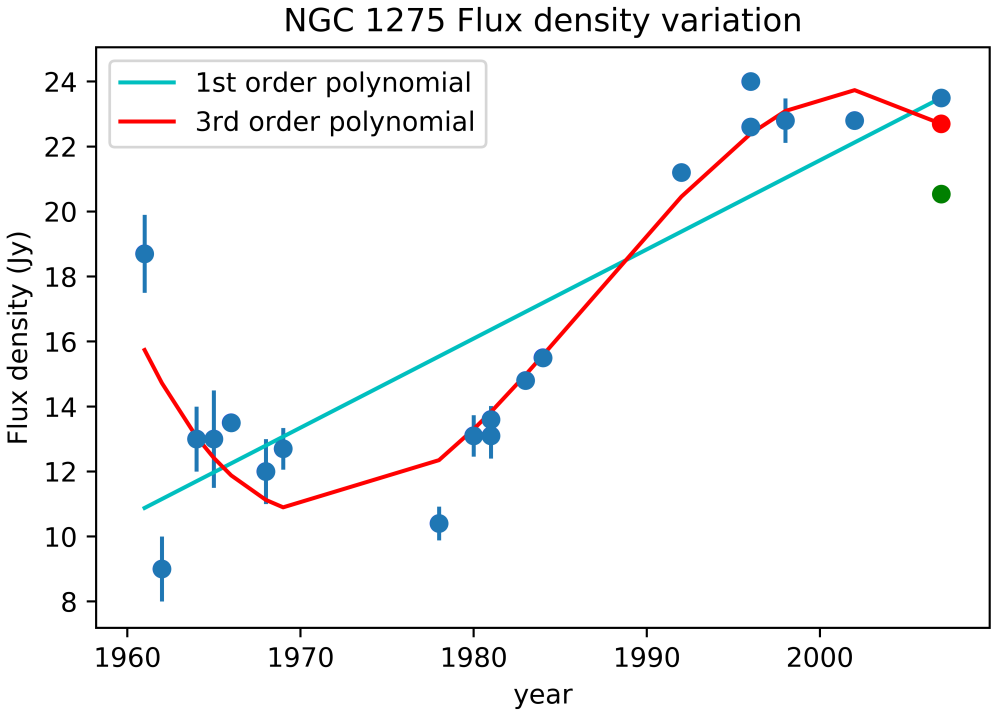

FIGURE 4.3: Variation of the flux density of 3C 84 at 1.4 GHz since 1961 (from Ryle and Windram, 1968; Pedlar et al., 1990, and NED). A third order (red) and first order (cyan) best fit lines are shown. The three rightmost dots represent the flux density of 3C 84 in 2007, with the blue and red dots showing the first and third order best fit estimates, respectively, while the green dot is the measured WSRT flux density from this work.

4.1.2 The Perseus mini-halo

The emission of the Perseus mini-halo around 3C 84 is shown in Figure 4.1 at a resolution of 21″ and a sensitivity of roughly 1.2 mJy beam^{-1} (from Pedlar et al., 1990) with the WSRT contours from Figure 3.11 overlaid. The WSRT contours trace the VLA map of the emission quite well.

There is an asymmetry in the emission of the mini-halo, with more features and emission generally located to the south and west of the core, as pointed out by Pedlar et al. (1990). This is seen from roughly 50″ away from the centre along position angles PA $\sim 120°$ in the southeast and $\sim 280°$ in the north west. In the north west, the emission proceeds along this PA for another 30″ before turning anti-clockwise towards PA $\sim 30°$. In the south east a similar effect is seen with the emission turning to PA $\sim 230°$ and proceeding for over 2′ before further turning anti-clockwise along PA $\sim 300°$ towards NGC 1272.

The mini-halo emission south of the core appears to terminate around NGC 1272, but there is also a hint of a much fainter (1.5σ) bridge possibly connecting NGC 1272 to the mini-halo; while the northern emission appears at this frequency to terminate in the *northern extension* (see Figure 1.21; Gendron-Marsolais et al., 2017). The overall emission of the mini-halo emission exhibits an anti-clockwise tendency in its distribution, which provides support for the correlation of the mini-halo's morphology with the underlying X-ray emission's morphology (see Chapter 1.5.3). This is noticeable in Figure 4.4, where the outer cavities coincide with the change in direction of the mini-halo emission, as well as the cavities' location along the same PA as the mini-halo features. The X-ray emission also shows a clear anti-clockwise distribution.

Due to its irregular shape, the extent of the mini halo is not easily defined by a single radius value. We used the minimum R_{min} and maximum R_{max} radii measured down to the 3σ contour to find the its average radius R_{MH} (Giacintucci et al., 2014a):

$$R_{\rm MH} = \sqrt{R_{\rm max} \times R_{\rm min}} = 69\,{\rm kpc}. \tag{4.2}$$

This value is a factor of two smaller than that reported in Giacintucci et al. (2014a) at the same frequency. On the other hand, Pedlar et al. (1990) measure the total radius down to the noise level ($1\sigma = 1$ mJy beam^{-1}), and find a value of $\sim 5'$. Using the same criteria, we find a maximum radius of $\sim 4.7'$ for the mini-halo, translating to a total radius of about 100 kpc at 1σ. Thus, using the Pedlar et al. (1990) method, our measurement gives us a value that is much closer to the Giacintucci et al. (2014a) result, at $\sim 77\%$ of their measured radius.

If we integrate the emission above 5σ in the primary beam corrected images we obtain a 22.50 Jy flux density, including the contribution from 3C 84. Subracting 3C 84, we measure 1.96 ± 0.04 Jy for the mini halo flux density, 30% fainter than the value reported by Giacintucci et al. (2014a).

We calculate the mini halo monochromatic radio power at 1.4 GHz using (e.g., Di Gennaro et al., 2018):

$$P_{1.4\ \rm GHz} = 4\pi d_{\rm L}^2 S_{1.4\ \rm GHz} = (1.38 \pm 0.03) \times 10^{24} {\rm WHz}^{-1}, \tag{4.3}$$

where $S_{1.4\ \rm GHz}$ is the measured flux density and $d_{\rm L}$ is the distance to the source in Mpc. We note that our value is $\sim 37\%$ less than the literature value (Giacintucci et al., 2014a). There

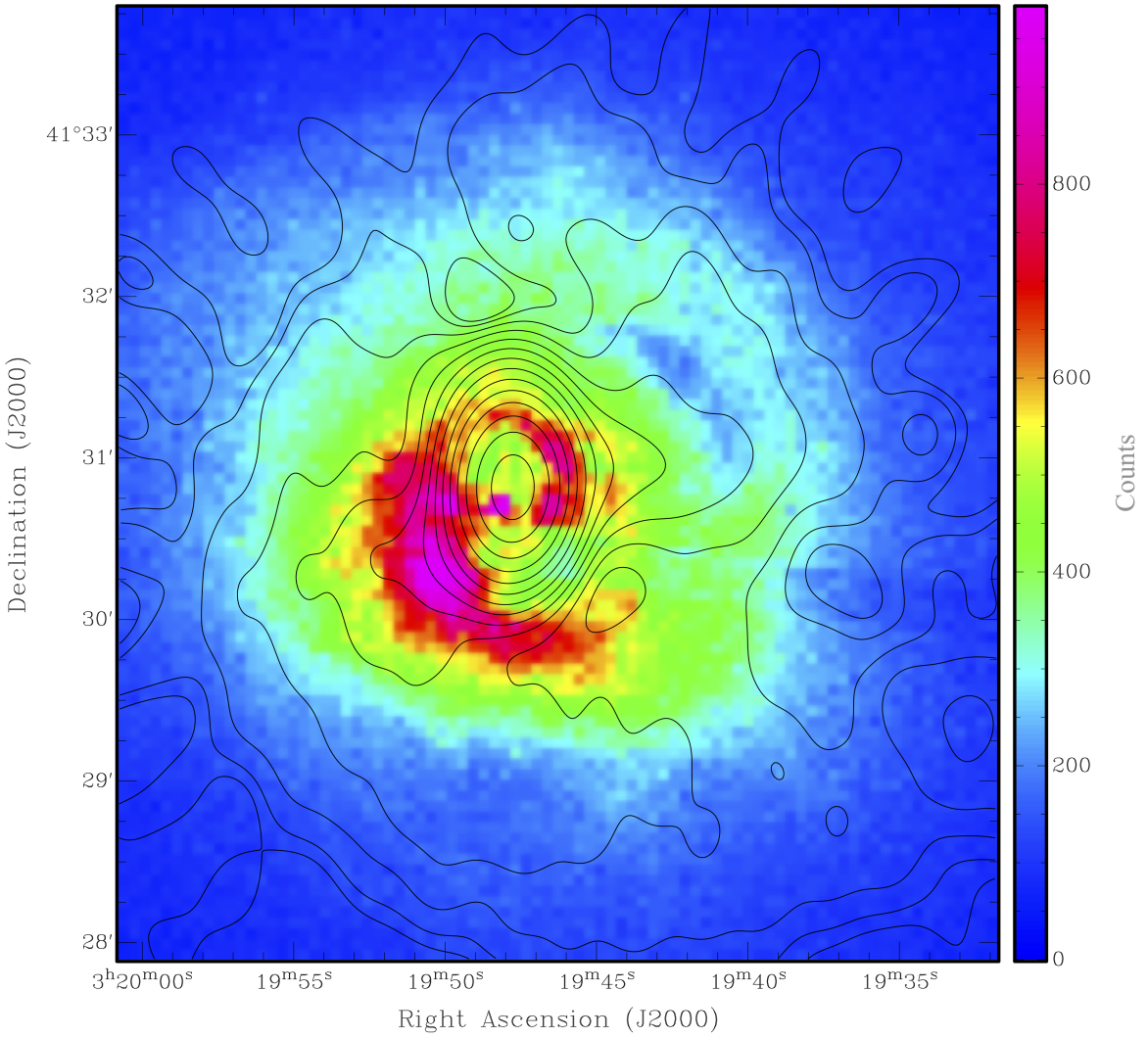

FIGURE 4.4: X-ray image of the region around 3C 84 (Fabian et al., 2000) with WSRT radio contours overlaid. The WSRT contour levels are shown at 5σ incremented by factors of 2, up to 4.93 Jy beam^{-1}, with a 83 μJy beam^{-1} noise level.

are several sources of uncertainty in our measurements, but we believe the total error budget is in the range of 10% to 20%. Since our images are calibration and deconvolution-limited, we conservatively estimate the radius of the source, which ultimately leads to a conservative estimate of the source flux density.

4.2 NORTH Pointing

The NORTH pointing is almost centred on the head tail radio source 3C 83.1 B. Our angular resolution does not allow us to resolve the details of the core and the source jets (see Section 1.5.2), but allows us to image the large scale tail with high sensitivity. Figure 4.5 shows that our

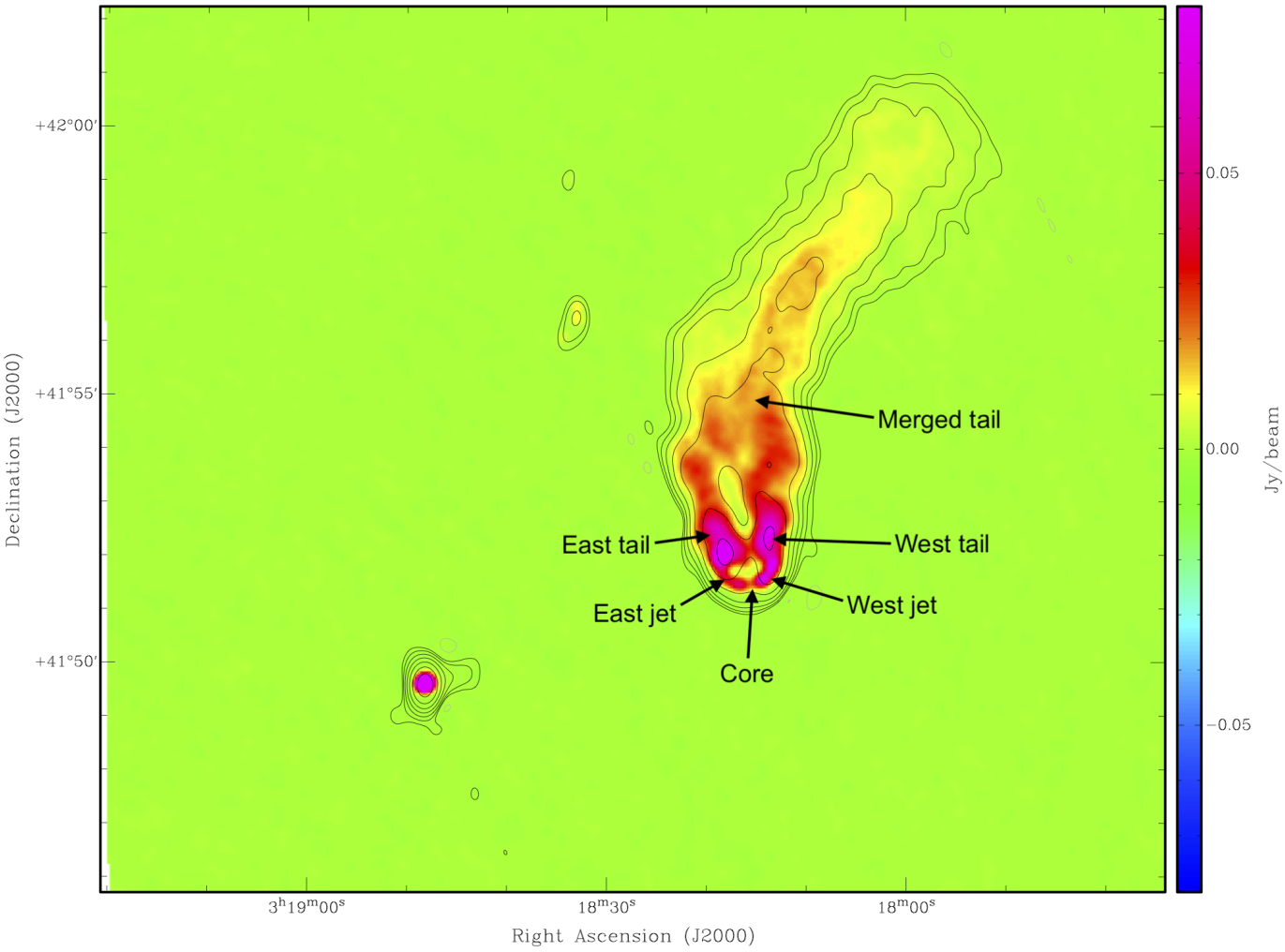

FIGURE 4.5: WSRT radio contours overlaid on the VLA 1.4 GHz image with an angular resolution of 12″ showing 3C 83.1 B (adapted from O'Dea and Owen, 1986). The contour levels run from $\pm 5\sigma$ incremented by factors of 2, up to 381 mJy beam^{-1}, $\sigma = 0.34$ mJy beam^{-1}

.

observations, which have a higher sensitivity, are in very good agreement with previous ones (O'Dea and Owen, 1986).

We measured the flux density of the source above the 5 σ contours to be 5.49 ± 0.02 Jy at 1380 MHz, which is about 30% fainter than in previous observations (H. Kuhr et al., 1981; Condon and Cotton, 2002). The cause of the discrepancy may be due to a systematic error in our amplitude calibration or to a relatively shallow deconvolution and will be the subject of further investigation. Using Equation 4.3, the measured flux density of 5.49 ± 0.02 Jy gives us a value of $(3.86 \pm 0.01) \times 10^{24}$ W Hz^{-1} for the monochromatic radio power of 3C 83.1 B.

Chapter 5

Conclusion

In this thesis we present Westerbork observations of the Perseus galaxy cluster at a frequency of 1380 MHz. The observations comprised two telescope pointings focused 25′ east and 40′ north west of the cluster centre for a total of $\sim$ 24 hours per pointing. The two pointings covered a total area of $\sim$ 0.5 square degrees.

The data reduction used some non standard techniques like the multiscale `clean` algorithm to achieve accurate modelling of bright, extended sources and to achieve high dynamic range images. In the case of the east pointing we achieve a 60000 : 1 dynamic range. The noise levels were 83 μJy beam^{-1} and 240 μJy beam^{-1} for the east and north pointing respectively with a $31'' \times 21''$ angular resolution.

We detect the Perseus mini halo at high sensitivity, extending over $\sim$ 140 kpc diameter. Its morphology is fairly similar to what is observed at 240 MHz (e.g. Gendron-Marsolais et al., 2017).

We separate the contribution of the central 3C 84 source from the mini halo and measure their flux densities to be 20.5 ± 0.4 Jy (corresponding to a 1.5×10^{25} W Hz^{-1} radio power) and 1.96 ± 0.04 Jy, respectively. We found 3C 84 to be consistent with the literature values at the same epoch, confirming the source increase in brightness by a factor of $\sim$ 2 over four decades. Our measurement of the mini halo flux density is discrepant at 37% from Giacintucci et al. (2014a), although no obvious reason was found for the difference and further investigation is needed.

We also obtained a high fidelity image of 3C 83.1 B, however, due to the limited angular resolution, our observations are not a significant improvement over existing ones (e.g., O'Dea and Owen, 1986, 1987).

Our observations, however, provide the deepest - to date, large field images at 1.4 GHz: future analysis of the whole field, including polarization, are likely to shed light on the cluster weather, i.e. the connection between AGN and ICM emission.

Bibliography

M. Gendron-Marsolais, J. Hlavacek-Larrondo, R. J. van Weeren, T. Clarke, A. C. Fabian, H. T. Intema, G. B. Taylor, K. M. Blundell, and J. S. Sanders. *Mon. Not. R. Astron. Soc.*, 469(4): 3872–3880, 2017.

R. J. Gott III and Martin J. Rees. *Astron. Astrophys.*, 45(2):365–376, 1975.

S. D. M. White and M. J. Rees. *Mon. Not. R. Astron. Soc.*, 183:341–358, 1978.

George R. Blumenthal, S. M. Faber, Joel R. Primack, and Martin J. Rees. *Nature*, 311(5986): 517–525, 1984.

Craig L. Sarazin. *Cambridge Univ. Press*, 1(1):23–42, 1988.

Mitchell F Struble and Herbert J Rood. *Astrophys. J. Suppl. Ser.*, 77:35–71, 1991.

Neta A. Bahcall. (1958), 1996.

S. Paul, R. S. John, P. Gupta, and H. Kumar. *Mon. Not. R. Astron. Soc.*, 471(1):2–11, 2017.

Gorge O. Abell. *Astrophys. J.*, 3(211A), 1958.

Neta A. Bahcall. *Annu. Rev. Astron. Astrophys.*, 15:505–540, 1977.

A. Dressler. *Annu. Rev. Astron. Astrophys.*, 22:185–222, 1984.

Richard Powell, 2006.

A. C. Fabian, J. S. Sanders, S. Ettori, G. B. Taylor, S. W. Allen, C. S. Crawford, K. Iwasawa, R. M. Johnstone, and P. M. Ogle. *Mon. Not. R. Astron. Soc.*, 318(4):L65–L68, 2000.

K.˜I. Tanaka. *Publ. Astron. Soc. Japan*, 37:481–497, 1985.

J. Brunzendorf and H Meusinger. *Astron. Astrophys.*, 161:141–161, 1999.

G. R. Gisler and G. K. Miley. *Astron. Astrophys.*, 76:109–119, 1979.

Carl K Seyfert. *Astrophys. J.*, 97:28, 1943.

A. Pedlar, H. S. Ghataure, R. D. Davies, B. A. Harrison, R. Perley, P. C. Crane, and S. W. Unger. *Mon. Not. R. Astron. Soc.*, 246(3):477–489, 1990.

A. C. Fabian, R. M. Johnstone, J. S. Sanders, C. J. Conselice, C. S. Crawford, J. S. Gallagher, and E. Zweibel. *Nature*, 454(7207):968–970, 2008.

N. A. Hatch, C. S. Crawford, R. M. Johnstone, and A. C. Fabian. *Mon. Not. R. Astron. Soc.*, 367(2):433–448, 2006.

P. Salomé, F. Combes, Y. Revaz, D. Downes, A. C. Edge, and A. C. Fabian. *Astron. Astrophys.*, 531:A85, 2011.

The Hitomi Collaboration. *Nature*, 535(7610):117–121, 2016.

E T Byram, T A Chubb, and H Friedman. *Science (80-.).*, 152(3718):66 – 71, 1966.

Gilbert Fritz, Arthur Davidsen, John F Meekins, and H. Friedman. *Astrophys. J.*, 164(3c 84): 81–85, 1971.

H. Gursky, E.M Kellogg, C. Leong, H. Tananbaum, and R. Giacconi. *Astrophys. J.*, 165(1964): 43–48, 1971.

G. Mark Voit. *Rev. Mod. Phys.*, 77(1):207–258, 2005.

J. Aleksić, L. A. Antonelli, P. Antoranz, and M. Backes. *Astrophys. J.*, 710(1):634–647, 2010.

C Jones and W Forman. *Adv. Sp. Res.*, 10(2):209–216, 1992.

J. E. Felten, R.J. Gould, W.A Stein, and N. J. Woolf. *Astrophys. J.*, 146(3):955 – 958, 1966.

Susan M Lea, Joseph Silk, E Kellogg, and S Murray. *Astrophys. J.*, 184:L105, 2002.

J A Gaunt. *Philos. Trans. R. Soc. London. Ser. A, Contain. Pap. a Math. or Phys. Character*, 229:163–204, 1930.

W. J. Karzas and R. Latter. *Astrophys. J. Suppl.*, 6:167, 1961.

C. L. Sarazin and J. N. Bahcall. *Astrophys. J. Suppl. Ser.*, 34(1):451–467, 1977.

A. Cavaliere and R. Fusco-Femiano. *Astron. Astrophys.*, 49:137–144, 1976.

Doris M. Neumann and Monique Arnaud. *Astron. Astrophys.*, 11:1–16, 1999.

Nobuyoshi Makino, Shin Sasaki, and Yasushi Suto. *Astrophys. J.*, 497(2):555–558, 2002.

Lori M. Lubin and Neta A. Bahcall. *Astrophys. J.*, 415:L17–L20, 1993.

Neta A. Bahcall and Lori M. Lubin. *Astrophys. J.*, 426:513–515, 1994.

C. Jones and W. Forman. *Astrophys. J.*, 276:38–55, 1984.

A. C. Fabian, A. Celotti, K. M. Blundell, N. E. Kassim, and R. A. Perley. *Mon. Not. R. Astron. Soc.*, 331(2):369–375, 2002.

L. L. Cowie and J. Binney. *Astrophys. J.*, 215(1974):723, 1977.

Sabrina De Grandi and Silvano Molendi. *Astrophys. J.*, pages 1–18, 2001.

A. C. Fabian. *Annu. Rev. Astron. Astrophys.*, pages 277–318, 1994.

A. C. Fabian, J. S. Sanders, G. B. Taylor, S. W. Allen, C. S. Crawford, R. M. Johnstone, and K. Iwasawa. *Mon. Not. R. Astron. Soc.*, 366(2):417–428, 2006.

Joseph Silk. *Astron. J.*, pages 646–649, 1976.

A. C. Fabian and P. E. J. Nulsen. *Mon. Not. R. Astron. Soc.*, 180(3):479–484, 1977.

P. Gorenstein, D. Fabricant, K. Topka, W. Tucker, and F. R. Harnden Jr. *Astrophys. J.*, 216: 95–99, 1977.

M. P. Ulmer and J. G. Jernigan. *Astrophys. J.*, 222:L85–L89, 1978.

Hans Böhringer and Norbert Werner. *Astron. Astrophys. Rev.*, 18(1-2):127–196, 2010.

Luigina Feretti, Gabriele Giovannini, Federica Govoni, and Matteo Murgia. *Astron. Astrophys. Rev.*, 20(1):1–60, 2012.

P. A. Thomas and A.C. Fabian. *Mon. Not. R. Astron. Soc.*, 155(1986):1986, 1987.

J. R. Peterson and A. C. Fabian. *Phys. Rep.*, 427(1):1–39, 2006.

Andrew C Fabian. page 24, 2002.

Joseph Silk, Rosemary F G Wyse, and Gustavo Bruzual A. *Astrophys. J.*, pages 415–425, 1986.

Y. Ikebe, T. H. Reiprich, H. Böhringer, Y. Tanaka, and T. Kitayama. *Astron. Astrophys.*, 383: 773–790, 2002.

A C Fabian, J S Sanders, S W Allen, R E A Canning, E Churazov, C S Crawford, W Forman, J Gabany, R M Johnstone, H R Russell, C S Reynolds, P Salom, G B Taylor, and A J Young. *Mon. Not. R. Astron. Soc.*, 2164:2154–2164, 2011.

H. Böhringer, W. Voges, A.C. Fabian, A.C. Edge, and D.M. Neumann. *Mon. Not. R. Astron. Soc.*, 264:L25–L28, 1993.

Sebastian Heinz, Christopher S Reynolds, and Mitchell C Begelman. *Astrophys. J.*, 501(1): 126–136, 1998.

Luigina Feretti. *Mem. della Soc. Astron. Ital. v.79, p.176*, 79:176, 2007.

A.C. Fabian, E. M. Hu, L. L. Cowie, and J. Grindlay. *Astrophys. J.*, 1:47–51, 1981.

B.L. Fanaroff and J. M. Riley. *Mon. Not. R. Astron. Soc.*, 167(167):31–35, 1974.

Preeti Kharb, Ethan Stanley, Matthew Lister, Herman Marshall, Chris O'Dea, and Stefi Baum. *Proc. Int. Astron. Union*, 313:211 – 218, 2014.

B. R. McNamara and P. E. J. Nulsen. *Annu. Rev. Astron. Astrophys.*, 45:117–175, 2007.

Myriam Gitti, Fabrizio Brighenti, and Brian R. McNamara. *Adv. Astron.*, 2012(Icm):1–24, 2012.

H Croston and M J Hardcastle. *Mon. Not. R. Astron. Soc.*, 438(September):3310–3321, 2014.

Esther L. Zirbel. *Astrophys. J.*, 476(2):489–509, 1997.

Gopal-Krishna and Paul J. Wiita. *Astron. Astrophys.*, 363:507–516, 2000.

M. P. Gawroński, A. Marecki, M. Kunert-Bajraszewska, and A. J. Kus. *Astron. Astrophys.*, 447 (1):63–70, 2006.

B. P. Miller and W. N. Brandt. *Astrophys. J.*, 695(1):755–764, 2009.

Frazer N. Owen and Michael J. Ledlow. *ASP Conf. Ser.*, 54:3190, 1994.

S. A. Baum, E. L. Zirbel, and C. P. O'dea. *Astrophys. J.*, 451:88–99, 1995.

G. Ghisellini and A. Celotti. *Astron. Astrophys.*, 379(1):L1–L4, 2003.

Danilo Marchesini, Annalisa Celotti, and Laura Ferrarese. *Mon. Not. R. Astron. Soc.*, 351(2): 733–744, 2004.

L. Rudnick and F. N. Owen. *Astrophys. J.*, 203:L107–L111, 1976.

S.A.E.G. Falle. *Mon. Not. R. Astron. Soc.*, 250:581–596, 1991.

Geo V Bicknell. *Astrophys. J.*, 422(2):542–561, 1994.

Christian R. Kaiser and Paul Alexander. *Mon. Not. R. Astron. Soc.*, 286(1):215–222, 1997.

Masanori Nakamura, Ian L. Tregillis, Hui Li, and Shengtai Li. *Astrophys. J.*, 686(2):843–850, 2008.

J. A. Biretta, F. Zhou, and F. N. Owen. *Astrophys. J.*, 447:582–596, 1995.

Joshua D. Wing and Elizabeth L. Blanton. *Astron. J.*, 141(3), 2011.

L. Saripalli. *Astron. J.*, 144(3), 2012.

S. Dehghan, M. Johnston-Hollitt, T. M. O. Franzen, R. P. Norris, and N.A Miller. *Astron. J.*, 1088(May):1–13, 2014.

M. Johnston-Hollitt, S. Dehghan, and L. Pratley. *Proc. Int. Astron. Union*, 10(S313):321–326, 2014.

Minnie Y. Mao, Melanie Johnston-Hollitt, Jamie B. Stevens, and Simon J. Wotherspoon. *Mon. Not. R. Astron. Soc.*, 12(November):1–12, 2009.

James E Gunn and J Richard Gott III. *Astrophys. J.*, 176(1):1–19, 1972.

G K Miley, G C Perola, and P. C. Van Der Kruit. *Nature*, pages 269–272, 1972.

Dharam Vir Lal and A. Pramesh Rao. *Astron. Astrophys.*, 420(2):491–499, 2004.

Mitchell C. Begelman, Martin J. Rees, and Roger D. Blandford. *Nature*, 279(5716):770–773, 1979.

T W Jones and F N Owen. *Astrophys. J.*, 234(234):818–824, 1979.

E. Freeland and E. Wilcots. *Astrophys. J.*, 738(2), 2011.

Zolile Mguda, Andreas Faltenbacher, Kurt Van Der Heyden, Stefan Gottl, Catherine Cress, Petri Vaisanen, and Gustavo Yepes. *Mon. Not. R. Astron. Soc.*, 3318:3310–3318, 2015.

F. N. Owen and L. Rudnick. *Astrophys. J.*, 13(2):258–283, 1976.

D. Sijbring and a. G. de Bruyn. *Astron. Astrophys.*, 331:901, 1998.

M. Ryle and M.D. Windram. *Mon. Not. R. Astron. Soc.*, 138:1–21, 1968.

M. A. G. Willson. *Mon. Not. R. Astron. Soc.*, 151:1–44, 1970.

G Giovannini and L Feretti. *Merging Process. Galaxy Clust.*, 272:197–227, 2002.

Ruta Kale, K.˜S. Dwarakanath, Dharam Vir Lal, Joydeep Bagchi, Surajit Paul, Siddharth Malu, Abhirup Datta, Viral Parekh, Prateek Sharma, and Mamta Pand ey Pommier. *J. Astrophys. Astron.*, 37(4):31, 2016.

Tiziana Venturi. *Mem. della Soc. Astron. Ital.*, 75(Societa Astronomica Italiana):282–289, 2011.

Simona Giacintucci, Maxim Markevitch, Tiziana Venturi, Tracy E Clarke, Rosella Cassano, and Pasquale Mazzotta. *Astrophys. J.*, 2014a.

R. Kale, T. Venturi, S. Giacintucci, D. Dallacasa, R. Cassano, G. Brunetti, V. Cuciti, G. Macario, and R. Athreya. *Astron. Astrophys.*, 92:1–22, 2015.

Amitesh Omar. *Mon. Not. R. Astron. Soc.*, 000(February), 2019.

Jack O Burns, Martin E Sulkanen, and Rick A Perley. *Astrophys. J.*, 388:49–52, 1992.

R. Cassano, M. Gitti, and G. Brunetti. *Astron. Astrophys.*, 486(3):L31–L34, 2008.

G. Brunetti and T. W. Jones. *Int. J. Mod. Phys.*, pages 1–74, 2014.

T Venturi, S Giacintucci, D Dallacasa, R Cassano, G Brunetti, S Bardelli, and G Setti. *Astron. Astrophys.*, 484:327, 2008.

R. Cassano, G. Brunetti, and T. Venturi. *J. Astrophys. Astron.*, 32(4):519–527, 2011.

F. Govoni, L. Feretti, G. Giovannini, H. Böhringer, T. H. Reiprich, and M. Murgia. *Astron. Astrophys.*, 376(3):803–819, 2001.

Luigina Feretti. 2003.

G Brunetti and G Setti. *Mon. Not. R. Astron. Soc.*, 21(May):1–21, 2018.

R. Cassano, S. Ettori, G. Brunetti, S. Giacintucci, G. W. Pratt, T. Venturi, R. Kale, K. Dolag, and M. Markevitch. *Astrophys. J.*, 777(2):141, 2013.

G Brunetti, G Setti, L Feretti, and G Giovannini. *Mon. Not. R. Astron. Soc.*, 320(3):365–378, 2001.

G. Brunetti, S. Giacintucci, R. Cassano, W. Lane, D. Dallacasa, T. Venturi, N. E. Kassim, G. Setti, W. D. Cotton, and M. Markevitch. *Nature*, 455(7215):944–947, 2008.

A Bonafede, H. T. Intema, M. Brüggen, M. Girardi, M. Nonino, N. Kantharia, R. J. van Weeren, H. J. A. Röttgering, and R. J. Van Weeren. *Astrophys. J. ApJ*, 785(1):1, 2014.

F. Vazza, M. Brüggen, R. van Weeren, A. Bonafede, K. Dolag, and G. Brunetti. *Mon. Not. R. Astron. Soc.*, 421(3):1868–1873, 2012.

Luigina Feretti. *Adv. Sp. Res.*, 36(4):729–737, 2005.

Joydeep Bagchi, Florence Durret, B Lima Neto, and Surajit Paul. *Science (80-.).*, 314 (November):791–794, 2006.

A. Bonafede, G. Giovannini, L. Feretti, F. Govoni, and M. Murgia. *Astron. Astrophys.*, 494(2): 429–442, 2009.

A. Botteon, F. Gastaldello, G. Brunetti, and R. Kale. *Mon. Not. R. Astron. Soc.*, 463(2): 1534–1542, 2016.

R. Kale, T. Venturi, S. Giacintucci, D. Dallacasa, R. Cassano, G. Brunetti, G. Macario, and R. Athreya. *Astron. Astrophys.*, 556(A99):1–18, 2013.

L. Bravi, M. Gitti, and G. Brunetti. *Mon. Not. R. Astron. Soc. Lett.*, 455(1):L41–L45, 2016.

M. Gitti, G. Brunetti, and G. Setti. *Astron. Astrophys.*, 35(386):456–463, 2002.

M Gitti, G Brunetti, L Feretti, and G Setti. *Astron. Astrophys.*, 11:1–11, 2004.

Myriam Gitti, Chiara Ferrari, Wilfried Domainko, Luigina Feretti, and Sabine Schindler. *Astron. Astrophys.*, 28(7658):5, 2007.

Federica Govoni, Klaus Dolag, Matteo Murgia, Luigina Feretti, and S. Schindler. *Rev. Mex. Astron. y Astrofis. Conf. Ser.*, 36:308–311, 2009.

J A ZuHone, M Markevitch, G Brunetti, and S Giacintucci. *Astrophys. J.*, 78, 2013.

Pasquale Mazzotta and Simona Giacintucci. *Astrophys. J.*, 675(1):L9–L12, 2008.

A. Pedlar, R. V. Booler, and R. D. Davies. *Mon. Not. R. Astron. Soc.*, 203:667–675, 1983.

D.˜O. Edge, J.˜R. Shakeshaft, W.˜B. McAdam, J.˜E. Baldwin, and S Archer. *Mem. R. Astron. Soc.*, 68:37–60, 1959.

K.˜M. Blundell, N.˜E. Kassim, and R.˜A. Perley. volume 199, page 189, 2002.

G. K. Miley, K. J. Wellington, and H. van der Laan. *Astron. Astrophys.*, 1975.

E Churazov, W Forman, and C Jones. *Astron. Astrophys.*, 356:788–794, 2000.

Myriam Gitti, Gianfranco Brunetti, Giancarlo Setti, Luigina Feretti, and I Bologna. volume 6, page 7, 2003.

A. C. Fabian, J. S. Sanders, S.W. Allen, C. S. Crawford, K. Iwasawa, R. M. Johnstone, R.W. Schmidt, and G. B. Taylor. *Mon. Not. R. Astron. Soc.m*, 172(11):1434–1435, 2003.

V. L. Ginzburg and S. I. Syrovatskii. *Annu. Rev. Astron. Astrophys.*, 3:297, 1965.

L. Birzan, D. A. Rafferty, B. R. McNamara, M. W. Wise, and P. E. J. Nulsen. *Astrophys. J.*, 607:800–809, 2004.

R. J.H. Dunn, A. C. Fabian, and J. S. Sanders. *Mon. Not. R. Astron. Soc.*, 366(3):758–766, 2006.

A C Fabian, S A Walker, H R Russell, C Pinto, J S Sanders, and C S Reynolds. *Mon. Not. R. Astron. Soc.*, 000(August), 2017.

Christopher P O'Dea and Frazer N Owen. *Astrophys. J.*, 1265(3):841–859, 1986.

L Feretti, G Giovannini, U Klein, K.-H Mack, L G Sijbring, and G Zech. *Astron. Astrophys*, 331 (1991):475–484, 1998.

G. K. Miley. *Astron. Astrophys.*, 26:413 – 421, 1973.

Luke Pratley, Melanie Johnston-Hollitt, Siamak Dehghan, and Ming Sun. *Mon. Not. R. Astron. Soc.*, 432(1):243–257, 2013.

W. J. Jaffe and G. C. Perola. *Astron. Astrophys.*, 26:423–435, 1973.

P. Alexander and J. P. Leahy. *Mon. Not. R. Astron. Soc.*, 225:1 – 26, 1987.

L. Feretti, D. Dallacasa, G. Giovannini, and T. Venturi. *Astron. Astrophys.*, 232:337–343, 1990.

H. Andernach, L. Feretti, G. Giovannini, U. Klein, E. Rossetti, and J. Schnaubelt. *Astron. Astrophys. Suppl. Ser.*, 93:331 – 357, 1992.

J. P. Vallee and R. S. Roger. *Astron. J.*, 155:1986, 1987.

Shweta Srivastava and Ashok K Singal. *arXiv e-prints*, 1:arXiv:1610.07783, 2016.

L. G. Sijbring. 1993.

S. Giacintucci, M. Markevitch, G. Brunetti, J. A. Zuhone, T. Venturi, P. Mazzotta, and H. Bourdin. *Astrophys. J.*, 795(1), 2014b.

R. A. Sunyaev. *Sov. Astron. Lett.*, 8:175–178, 1982.

Michael W Wise and Craig L Sarazin. *Astrophys. J.*, 363:344–348, 1990.

A. G. de Bruyn and M. A. Brentjens. 947:931–947, 2005.

Drugonot, 2007.

James J Condon and Scott M. Ransom. 2016. ISBN 9780691137797.

Sophocles J Orfanidis. 2016.

A. Richard Thompson. *ASP Conf. Ser.*, 180:11–36, 1999.

F Zernike. *Physica*, 5(8):785–795, 1938.

Max Born and Emil Wolf. 1980.

A. Richard Thompson, James M. Moran, and George W. Swenson Jr. 2004. ISBN 0471254924.

Oleg M. Smirnov. *Astron. Astrophys.*, 106, 2011.

G. G. Stokes. *Trans. Cambridge Philos. Soc.*, 9(399):1 – 780, 1851.

Tim Cornwell and Edward B. Fomalont. *Astron. Soc. Pacific*, 6(23):185, 1989.

T. J. Pearson and A. C. S. Readhead. *Annu. Rev. Astron. Astrophys.*, 22:97 – 130, 1984.

Jonathan M. Marr, Ronald L. Snell, and Stanley E. Kurtz. 2016. ISBN 9781498770194.

J.A. Högbom. *Astron. Astrophys. Suppl. Ser.*, 53(9):1689–1699, 1974.

Griffin Foster. *Fundam. Radio Interferom.*, 2017.

B. G. Clark. *Astron. Astrophys.*, 89:377–378, 1980.

Frederic R Schwab. *Astron. J.*, 89:1076–1081, 1984.

Jonathan Kenyon, 2017.

A. C. S. Readhead and P. N. Wilkinson. *Astrophys. J.*, 223:25, 1978.

Astron, 2018a.

Astron, 2018b.

R Morganti. Technical report, 2004.

Roger Curry and David Knightington, 2014.

Roberto Francesco Pizzo. PhD thesis, 2010.

J P Mcmullin, B Waters, D Schiebel, W Young, and K Golap. *Astron. Data Anal. Softw. Syst. XVI*, 376:127, 2007.

Bruno Juncklaus Martins and Urvashi Rau. pages 59–64, 2016.

A. R. Offringa, A. G. de Bruyn, M. Biehl, S. Zaroubi, G. Bernardi, and V. N. Pandey. *Mon. Not. R. Astron. Soc.*, 405(1):155–167, 2010.

A R Offringa. *Astron. Astrophys.*, 595:A99, 2016.

R. A. Perley and B. J. Butler. *Astrophys. Journal, Suppl. Ser.*, 206(2):1–14, 2013.

R. J. Sault and J.E. Conway. *Synth. Imaging Radio Astron. II*, 180:419–432, 1999.

R.˜J. Sault and T.˜A. Oosterloo. *arXiv e-prints*, astro–ph/0(astro-ph/0701171):1–30, 2007.

Niruj Mohan and David. Rafferty, 2015.

Jan E. Noordam and Oleg M. Smirnov. *Astron. Astrophys.*, 61:1–16, 2010.

Tim J. Cornwell. *IEEE J. Sel. Top. Signal Process.*, 2(5):793–801, 2008.

G Bernardi, A G De Bruyn, M A Brentjens, B Ciardi, G Harker, and V Jeli. *Astron. Astrophys.*, 500:965–979, 2010.

William A Dent. *Astrophys. J.*, 144(2):843, 1966.

I. I. K. Pauliny-Toth and K. I. Kellerman. *Astrophys. J.*, 146:634, 1966.

K. I. Kellermann and I. I. Pauliny-Toth. *Annu. Rev. Astron. Astrophys.*, 6:417–448, 1968.

Christopher P O'Dea, William A. Dent, and Thomas J. Balonek. *Astrophys. J.*, 278:89–95, 1984.

G. Di Gennaro, T. Venturi, D. Dallacasa, S. Giacintucci, P. Merluzzi, G. Busarello, A. Mercurio, S. Bardelli, F. Gastaldello, A. Grado, C. P. Haines, L. Limatola, and M. Rossetti. *Astron. Astrophys.*, pages 1–24, 2018.

H. Kuhr, A. Witzel, I. I. K. Pauliny-Toth, and U. Nauber. *Astron. Astrophys. Suppl. Ser.*, 45: 367–430, 1981.

J J Condon and W D Cotton. *Astron. J.*, pages 675–689, 2002.

Christopher P O'Dea and Frazer N Owen. *Astrophys. J.*, 316:95–112, 1987.